

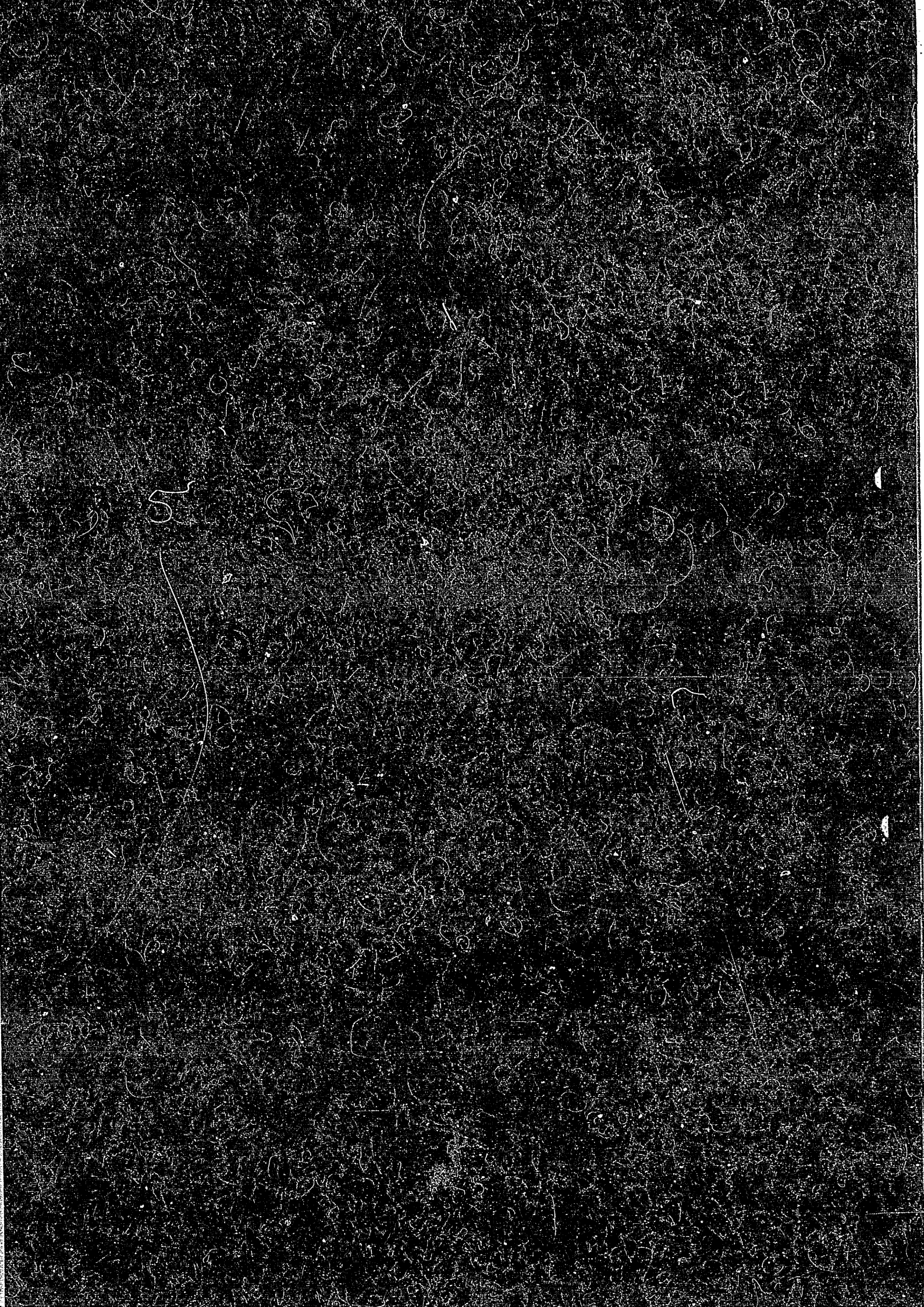
IPPJ-AM-39

**PROCEEDINGS
OF
THE JAPAN-U.S. WORKSHOP
ON
IMPURITY AND PARTICLE CONTROL,
THEORY AND MODELING**

EDITED BY T. KAWAMURA

**INSTITUTE OF PLASMA PHYSICS
NAGOYA UNIVERSITY**

NAGOYA, JAPAN



IPPJ-AM-39

**PROCEEDINGS
OF
THE JAPAN-U.S. WORKSHOP
ON
IMPURITY AND PARTICLE CONTROL, THEORY AND MODELING
MARCH 12 – 16, 1984**

Edited by
Takaichi KAWAMURA

Institute of Plasma Physics, Nagoya University
Chikusa-ku, Nagoya 464, Japan

March 1985

This document is prepared as a preprint of compilation of atomic data for fusion research sponsored fully or partly by the IPP/Nagoya University. This is intended for future publication in a journal or will be included in a data book after some evaluations or rearrangements of its contents. This document should not be referred without the agreement of the authors. Enquiries about copyright and reproduction should be addressed to Research Information Center, IPP/Nagoya University, Nagoya, Japan.

Preface

In the recent progresses of the experiments on divertor and limiter discharges and design studies of INTOR like machines, more precise models of Tokamak plasma are required, especially from the standpoint of impurity and particle controls. However, if we want to go a step further, it turns out that the present data of atomic and molecular physics are still insufficient to describe the models. This point is what we must improve near future through collaboration of plasma and atomic physicists.

As the next step of investigation, we must organize the experiment with appropriate magnetic field configurations and proper wall materials to suppress serious influences to core plasma from the edge. Through iterations of such procedure, we can reach reasonable plasma modelling to form the rigid base for the next generation machine.

I hope we can discuss these point during the coming 6th PSI conference in Nagoya.

A. Miyahara

CONTENTS

| | |
|--|-----|
| Memorandum of the Workshop | 1 |
| Plasma Engineering Considerations on Impurity Control of the Next-Step Tokamak, Focussing on INTOR Design Concept Noboru FUJISAWA | 8 |
| Numerical Simulation of Pellet Injection into Heliotron-E Yuji NAKAMURA | 30 |
| Numerical Analyses of Plasma and Neutral Particle Behavior for Poloidal Divertor in Fusion Experimental Reactor Masayoshi SUGIHARA, Seiji SAITO, Shigehisa HITOKI and Noboru FUJISAWA | 34 |
| Ergodic Magnetic Layer N. OHYABU, J. DeGRASSIE and N. BROOKS | 49 |
| Particle Simulation of Divertor Plasma T. TAKIZUKA, K. TANI and M. AZUMI | 52 |
| Modeling of Neutral Transport at the Plasma Edge D. HEIFETZ | 66 |
| Hydrogen Recycling at Wall Surface K. SONE | 92 |
| Impurity Transport Experiment by Surface Deposition Probe in JIPPT-IIU M. MOHRI and T. YAMASHINA | 106 |
| Study on Alpha-particle Diagnostics in Magnetically Confined Plasmas K. N. SATO and M. SASAO | 114 |

| | |
|---|-----|
| Ignition Simulation by the Interaction of NBI with ICRF Y. HAMADA, Y. OGAWA, T. AMANO and T. WATARI | 123 |
| Tokamak Impurity Control with Momentum Sources, Theory and Application. D. J. SIGMAR and W. M. STACEY | 125 |
| Boundary Conditions for H-Mode N. OHYABU | 140 |
| Simulation of Impurity Transport in H-mode Tokamak Discharge T. HIRAYAMA | 143 |

Memorandum
of
The Japan - U.S. Workshop
on
Impurity and Particle Control, Theory and Modeling

March 12(Monday)- 16(Friday), 1984
Institute of Plasma Physics, Nagoya University

Identification : Exchange A41.

Date : , From March 12 (Monday) to March 16 (Friday), 1984

Place : Institute of Plasma Physics, Nagoya University
Nagoya 464, Japan.

Visit : Japan Atomic Energy Research Institute,
Tokai Research Establishment (JAERI, Tokai).

Organizing : Key Persons,

Dr. Douglass E. Post, Jr. (U.S.)

Prof. Akira Miyahara (Japan).

Secretaries,

Dr. Takaichi Kawamura

Miss Miho Higuchi

Miss Mihoko Ishiguro

Mrs. Mitsuko Itonaga

Miss Yukimi Sugiura

Miss Akiko Yamada

Workshop Diary*

+ March 12 (Monday)

13:00 - Registration

13:50 Opening Address:

A. Miyahara (Inst. Plasma Phys., Nagoya Univ.)

D. Post (Princeton Univ., Plasma Phys. Lab.)

14:00 - 17:00

Session 1 (Chairman : T. Amano)

1 - 1, N. Fujisawa (JAERI) : Plasma Engineering Considerations on Impurity Control of Next step Tokamak, Focussing on INTOR Design Concept.

1 - 2, D. Post (PPPL) : Data Needs for Impurity Control Modeling (with D. Heifetz, K. Evans, W. Langer, R. Janev, J. Weisheit, C. Singer).

1 - 3, M. Wakatani (Plasma Phys. Lab., Kyoto Univ.) : Simulation of Pellet Injection Experiments in Heliotron E (Y. Nakamura and Wakatani).

+ March 13 (Tuesday)

9:00 - 12:30

Session 2 (Chairman : D. Heifetz)

2 - 1, R. Morse (univ. of Arizona) : Kinetic Modeling of Plasmas near Divertor & Limiter Plates, Resulting Sputtering Rates & Experimentally Identifiable Characteristics (P. McKenty, P. Gierszewski, J. McMullen & R. Morse).
Stationary Wall Plasma Structure in the Lower Temperature, Fluid Model Regime (G. Sowers, D. Morrison and R. Morse).

2 - 2, M. Sugihara (JAERI) : Numerical Analyses of Plasma and Neutral Particle Behavior for Poloidal Divertor in Fusion Experimental Reactor (with S. Saito, S. Hitoki and N. Fujisawa).

*Each title is the one on the occasion of presentation.

- 2 - 3, D. Post (PPPL) : An Analytic 1-D Divertor Model with
Neutral Sources (with W.D. Langer and M. Petravic).
2 - 4, N. Ohyanu (GA) : Ergodic Boundary Experiment (TEXT)
(with J. deGraggie, N. Brooks and TEXT Group).

14:00 - 17:30

Session 3 (Chairman : M. Wakatani)

- 3 - 1, T. Takizuka (JAERI) : Particle Simulation of Divertor
Plasma (with K. Tani and M. Azumi).
3 - 2¹⁾, D. Heifetz (PPPL) : Edge Plasma Neutral Transport
Modeling.
3 - 3²⁾, D. Post (PPPL) : Multi-Dimensional Plasma Edge
Modeling (with M. Petravic, D. Heifetz, G. Kuo-
Petravic, S. Lieberon- Heifetz)

18:30 - 20:30

Banquet

† March 14 (Wednesday)

9:00 - 12:00

Session 4 (Chairman : D. Sigmar)

- 4 - 1, K. Sone (JAERI) : Possibility of Recycling Rate Control
at Wall Surfaces.
4 - 2, M. Mohri (Hokkaido Univ.) : Impurity Transport
Experiment by Surface Deposition Probe in JIPPT-
IIU and Heliotron E (with T. Yamashina).
4 - 3, K.N. Sato (IPP, Nagoya) : Study on Alpha-Particle
Diagnostics in Magnetically Confined Plasmas
(with M. Sasao).

1) 3-3 in the distributed program.

2) 3-2 in the distributed program.

4 - 4, Y. Hamada (IPP, Nagoya) : Ignition Simulation by the Interaction of NBI and ICRF (with Y. Ogawa, T. Amano and T. Watari).

4 - 5¹⁾, N. Ohyabu (GA) : Boundary Conditions for H-Mode.

14:00 - 17:00

Session 5 (Chairman : T. Takizuka)

5 - 1, T. Amano (IPP) : Heating and Impurity Modeling for R-Tokamak.

5 - 2, D. Sigmar (ORNL) : Impurity control with Momentum Sources, Part I-Theory.

† March 15 (Thursday)

9:00 - 11:00

Session 6 (Chairman : N. Ohyabu)

6 - 1, T. Hirayama (JAERI) : Simulation of Impurity Transport in H-Mode Tokamak Discharge.

6 - 2, D. Sigmar (ORNL) : Impurity Control with Momentum Sources, Part II-Transport Modeling Results.

11:15 - 12:00

Session 7 (Chairman : D. Post)

Summary and Future Prospect:

A. Miyahara (Inst. Plasma Phys., Nagoya Univ.)

W. Sadowski (U.S. Dept. of Energy (DOE))

13:00 - 14:00

Laboratory Visits in IPP, Nagoya University.

† March 16 (Friday)

Workshop Visit to JAERI, Tokai.

1) 5-3 in the distributed program.

List of Participants

U.S.

| | |
|------------------------|--|
| HEIFETZ, Daniel | Princeton University, Plasma Physics Laboratory |
| MORSE, Richard | Univ. of Arizona |
| OHYABU, Nobuyoshi | GA Technologies |
| POST, Douglass E., Jr. | Princeton University, Plasma Physics Laboratory |
| SADOWSKI, Walter | U.S. Dept. of Energy |
| SIGMAR, Dieter J. | Fusion Energy Div. ORNL |

JAPAN

| | |
|----------------------|--------------------------|
| AKAISHI, Kenya | IPP, Nagoya Univ. |
| AMANO, Tuneo | IPP, Nagoya Univ. |
| AZUMI, Masafumi | JEARI, Tokai |
| FUJISAWA, Noboru | JEARI, Tokai |
| HAMADA, Yasuji | IPP, Nagoya Univ. |
| HIRAYAMA, Toshio | JEARI, Tokai |
| HITOKI, Shigehisa | Mitsubishi Electric Co. |
| ICHIKAWA, Yoshi-hiko | IPP, Nagoya Univ. |
| KADOTA, Kiyoshi, | IPP, Nagoya Univ. |
| KAMADA, Koji | IPP, Nagoya Univ. |
| KAMIMURA, Tetsuo | IPP, Nagoya Univ. |
| KANEKO, Toshiaki | Okayama Univ. of Science |
| KATO, Takako | IPP, Nagoya Univ. |
| KAWABE, Takaya | Univ. of Tsukuba |

| | |
|------------------------|------------------------|
| KAWAMURA, Takaichi | IPP, Nagoya Univ. |
| MATSUOKA, Keisuke | IPP, Nagoya Univ. |
| MIDZUNO, Yukio | IPP, Nagoya Univ. |
| MIYAHARA, Akira | IPP, Nagoya Univ. |
| MOHRI, Mamoru | Hokkaido Univ. |
| MOMOTA, Hiromu | IPP, Nagoya Univ. |
| NAKAMURA, Yuji | Kyoto Univ. |
| NISHIMURA, Hiroyuki | Niigata Univ. |
| OGAWA, Yuichi | IPP, Nagoya Univ. |
| OHNUMA, Toshiro | Tohoku Univ. |
| SAGARA, Akio | IPP, Nagoya Univ. |
| SAITO, Seiji | Hitachi LTD. |
| SASAO, Mamiko | IPP, Nagoya Univ. |
| SATO, Koh-nosuke | IPP, Nagoya Univ. |
| SONE, Kazuho | JAERI, Tokai |
| SUGAI, Hideo | Nagoya Univ. |
| SUGIHARA, Masayoshi | JAERI, Tokai |
| SUGIHARA, Ryo | IPP, Nagoya Univ. |
| TAKIZUKA, Tomonori | JAERI, Tokai |
| TANAKA, Motohiko | Hiroshima Univ. |
| TANI, Keiji | JAERI, Tokai |
| TAWARA, Hiroyuki | IPP, Nagoya Univ. |
| TERASHIMA, Yoshinosuke | IPP, Nagoya Univ. |
| TODOROKI, Jiro | IPP, Nagoya Univ. |
| TSUCHIDA, Kazuki | IPP, Nagoya Univ. |
| WAKATANI, Masahiro | Heliotron, Kyoto Univ. |

Plasma Engineering Considerations on Impurity Control of the
Next-Step Tokamak, Focussing on INTOR Design Concept

Fusion Research and Development Center
Tokai Research Establishment
Japan Atomic Energy Research Institute

Noboru Fujisawa

1. Introduction

Heats and particles flowing out from plasmas with their finite confinement times have to be removed reliably. Inevitable plasma-surface interactions in those situations would generate impurities from surfaces, which give severe influences on plasma confinement performance and have to be well controlled. The critical issue of the impurity control should be understood with well-balanced developments both in plasma physics, particularly peripheral plasmas, and in technology associated with heat and particle removal.

Looking back into past fusion reseaches, the impurity control played an outstandingly important role in production of high temperature plasmas. In a path to success in fusion reactors, of course, the impurity control will hold a essential key. In the INTOR Workshop, the impurity control issue has been actively tackled since the Phase Zero Workshop [1,2,3], with recognizing it as one of critical issues affecting the INTOR design concept.

Difficulties in the impurity control probem depend partly on powers to be removed, which are predicted to amount to about 1 GW in reactors. In the history of the impurity control studies in tokamaks up to now, emphases have been placed on trying to keep plasma as clean as possible in order to get higher temperature plasmas. Taking into account formidably large power to be handled in future tokamak reactors, however, the impurity conctrol concept should be reconsidered to change its tendency into harmonized co-existence with impurities, where most part of power could be taken out through radiations caused by impurities. Some symptoms of such a tendency is already observed in the present large tokamaks such as JT-60, JET, and TFTR. The next tokamaks, a good

representative of which is INTOR, seem to be just on a corner of the turnaround in the impurity control strategy.

Section 2 will review the plasma operation mode which is indispensable to perform INTOR objectives. Section 3 will describe critical items for the impurity control in tokamaks. Section 4 will compare two potential candidates for the INTOR impurity control, i.e., poloidal divertor and toroidal pumped limiter. Section 5 will discuss feasibility of high-density, low-temperature plasmas near divertor collector plate. Summary is presented in Section 6.

2. INTOR missions and plasma operation mode compatible with them

In a strategy of a tokamak fusion programme INTOR can be defined as the major experiment between the present generation of large tokamaks (TFTR, JET, JT-60, T-15) and the generation of demonstration reactors. The principal role of INTOR generally is the engineering demonstration of tokamak reactors [1].

The reactor-relevant mode of plasma operation is required to achieve the above major mission. Concretely, the following mode of operation is required for the INTOR plasma.

- (1) Ignited D-T plasma
- (2) Controlled burn pulse of >100 s
- (3) Reactor level neutron wall loading of $\geq 1 \text{ MW}\cdot\text{m}^{-2}$
- (4) Duty cycle ≥ 70 %
- (5) Availability of 25 - 50 %

The Zero Phase of the INTOR Workshop, which was conducted during 1979, addressed the programmatic roles and the technical objectives of INTOR and assessed plasma physics and technology bases requisite for such an INTOR experiment, and finally concluded that such an engineering test facility was feasible, provided that the supporting research and development activity is significantly expanded.

The INTOR Workshop was extended into Phase One, in early 1980, the objective of which was to develop a conceptual design of the INTOR experiment. As a result of this design work, the major INTOR design parameters, shown in Table 1, were developed in some detail and critical problems were identified.

From the viewpoint of the impurity control, the considerably crucial parameters may be the alpha heating power of 124 MW and the long burn

time of 100 - 200 s.

Alpha particles of high energy produced via D-T reaction heat D-T particles in the main plasma region. Most power of the alpha heating, then, flows out of the core plasma through conduction and convection processes. The major role of the impurity control therefore is to remove such a large power without deteriorating confinement performance of the main plasma.

Alpha particles after slowing down are ashes and should be removed as soon as possible. Otherwise, the concentration of the helium ash increases in the elapse of burning, and eventually they dilute the D-T reaction and at the same time raise a plasma beta value, which would be significantly severe constraint for tokamak plasmas at present.

3. Problem description

The design work of the impurity control system needs many important items to be evaluated. They are not only in plasma physics, but also include an impurity control engineering area. The major problematic items are as follows.

- (1) Parameters of scrape-off plasmas which directly interact with collector plates, receiving heat and particle fluxes from the main plasma.
- (2) Behaviors of impurities released from collector plates and first walls, both in the scrape-off layer and in the main plasma.
- (3) Heat and particle fluxes onto collector plates and first walls.
- (4) Helium ash exhaust.
- (5) Overall evaluation of the impurity control system from the plasma physics and technology viewpoints.

Scrape-off plasma parameters

One third of the alpha heating power, around 40 MW, is assumed to be radiated to first walls in the INTOR operating scenario. The rest of it, about 80 MW, therefore is transferred through the main plasma edge to scrape-off plasmas and heats them up. What parameters the scrape-off plasmas get is significantly crucial for impurity control studies. Because the scrape-off plasma directly interacts with collector plates and the energy of charge exchanged neutral particles plunging into the first walls also depends on the scrape-off plasma parameters.

The parameters of a scrape-off layer, such as density, temperature, and their profiles, are strongly dependent on heat and particle fluxes from main plasmas, particle and thermal diffusivities in the layer, behaviors of neutral DT particles and impurities from collector plates

and first walls. The reliable estimation of such parameters needs adequate data based on experimental and theoretical developments.

Behaviors of impurities

The most essential way for the impurity control is to avoid impurities from being released from plate and walls. It is however impossible to completely suppress the impurity ejection. Then, it becomes crucial for the impurity control to shield impurities from going into the main plasma and to keep it as clean as possible. Therefore, the behavior of impurities in the scrape-off layer should be understood in enough detail for the design. If the effect of impurities would turn to be so little, their radiation could be used positively in ways to reduce plasma temperature to decrease the heat load to collector plates.

The behaviors of impurities from walls and helium particles produced through D-T reactions in the main plasmas is also influential on the plasma confinement performance. Some part of impurities from walls and plates could unavoidably reach the main plasmas, especially high-Z impurities have great influences on the confinement performance. On the other hand, if impurities would not accumulate in the center of the main plasmas and their radiations could concentrate in the edge of the plasma column, the radiation loss machinery could be used to reduce the heat power to the scrape-off plasma.

As mentioned earlier, the long confinement time of helium ions is dangerous for long burning, because of its tendencies to dilute D-T reactions and to increase plasma beta values. The steady exhaust of the helium ashes also needs complete understanding of the helium ash behavior in the main and scrape-off plasmas.

Heat and particle fluxes to plates and walls

The heat and particle fluxes, including their energy spectra, are indispensable to the design study on the impurity control system. They should be evaluated in some detail, based on assessment of the above items mentioned. In addition to them, moreover, the design work needs other conditions to be considered, such as neutron wall loading, thermal and electromagnetic influences due to plasma disruptions, feasibility of maintenance and assembly of a reactor core, configurations of poloidal magnetic fields for plasma equilibrium and so on.

Helium ash exhaust

The helium ash should be removed continuously at the same rate as the alpha production to achieve the long burn operation of 100-200 s. The pumping requirement should of course be as small as possible to mitigate needs on research and development for a evacuating system. Moreover, if possible, a selective evacuation of the helium ash, which means to pump out mainly helium gases, should be paid some heeds to reduce the demands on a tritium processing system.

Overall evaluation for impurity control system

At present various impurity control concepts are proposed and investigated experimentally and theoretically. Which is the most favorable for INTOR should not be answered from only plasma consideration, it needs overall evaluation ranging from plasma physics to the technology. Furthermore, a future extension of the concept should be taken into considerations, because commercial reactors at present designs would produce a huge alpha heating power reaching about 1 GW, which is by one order as large as INTOR. Therefore, the most suitable method for INTOR might not necessarily extend to demonstration reactors.

4. Comparison study between single-null poloidal divertor and toroidal pumped limiter

The pre-conceptual design at the Phase One INTOR Workshop accommodated the single-null poloidal divertor as a reference impurity control method, based on data bases and some simple evaluation of scrape-off plasmas [2].

The impurity control issue was pointed as one of some critical technical issues to be resolved at the Phase-Two-A (Part 1) Workshop, which affect the INTOR design concept. During this phase, the poloidal divertor was investigated in more detail, and together with it the pumped limiter concept was also emphasized to compare it with the divertor. As a result of those efforts, the poloidal divertor was recommended to lieve as a reference method of the INTOR impurity control.

The results of the comparison between the divertor and limiter concepts are shown in Table 2. Their brief evaluations are described in the followings.

Plasma parameters in front of collector plates

Plasmas in a scrape-off layer, especially in front of collector plates, are crucial for impurity controlability. They depend on recycling D-T particles near the neutralizer plate, on the assumption of constant heat fluxes and no impurities. In general, with a large pumping speed and a particle supply with a pellet injection, the density and temperature of scrape-off plasmas respectively decreases and increases.

In a region of high-temperature (e.g. 1 kV) and low-density (e.g. of the order of 10^{18} m^{-3}), the sputtering yield of the collector plates is decreasing with increasing D-T particle energy, since it is beyond

its maximum. The incident D-T particle flux is also reduced to great extent due to reduced particle fluxes. In consequence, the flux of sputtered plate materials can be reduced significantly.

Potential realizability of such high temperature scrape-off plasma, however, seems at present to be significantly low because of no experimental indications and of concerns in arcing. It should be prudent to select such high-temperature and low-density scrape-off plasmas for INTOR.

The another operation region, which is just on the other side to the above and beneficial for the impurity control, is low-temperature ($\lesssim 30$ eV), high-density ($\gtrsim 10^{20} \text{ m}^{-3}$) plasmas. Such plasmas were lately observed near the neutralizer plates in Doublet III and ASDEX high density divertor discharges, and some elaborate divertor analyses codes indicate high possibility in the INTOR open-type divertor.

On the other hand, limiter plasmas are found to be difficult to approach the high-density, low-temperature region. Analyses on limiter plasmas disclose scrape-off layer plasmas to be medium temperature (50-200 eV) and medium-density ($< 10^{20} \text{ m}^{-3}$). This temperature range is unfavorable for the impurity control, since the sputtering yield of materials is near their maximum.

Impurity Controlability

The impurity control function can be subdivided into two. One is to suppress impurities from being released from materials, and the other is to prevent released impurities from going into the main plasmas.

The first function, reduction of impurity release, can work by decreasing plasma temperatures in front by plates and walls. The scrape-off plasma near the divertor plates has large possibility in getting to low temperatures. The low-temperature (e.g. $\lesssim 30$ eV) near

the limiter may be unrealistic at present, as mentioned above. In this context, the divertor could have more reliable impurity controllability than the limiter.

The second function, prevention of contamination of the main plasma, can also be observed considerable difference between the divertor and limiter concepts, stemming from difference in distance between the main plasmas and the plates. Impurities released from the limiter plates easily reach the main plasmas because the limiter plates are in a close vicinity of the main plasmas. Impurities released from the divertor plates could be forced to return to the plates due to electric fields in sheath and pre-sheath and frictional forces by D-T particle flows toward the plates.

Materials for collector plates

Materials for the limiter plates would be limited to low-Z, because the medium-temperature (50-200 eV) near the plates could result in the self-sputtering yield of more than unity for medium- and high-Z materials.

In the divertor case, as mentioned above, the low-temperature plasmas (≤ 30 eV) near the plates could be realized in a high density operation. Then the divertor plate materials might be free from the sputtering problem, they should be selected from other considerations on redeposition of first wall materials, thermal damage due to disruptions, and so on.

Erosion of first wall

Charge exchanged D-T neutral particles would erode significantly the first walls. For instance, sputtered quantity from the stainless-steel first wall would amount to about 1 ton/year under charge exchange

power of a few MW. Those impurities have great effects on the impurity control concept. Especially in the divertor case, the flow velocity of the scrape-off plasmas becomes considerably low and impurities released from the walls near a divertor entrance might have chances of penetrating into the main plasma. In the limiter case the situation might not be so serious, because the charge exchange loss is concentrated near the limiter and the flow velocity would not decrease so much.

Effects on plasma confinement performance

Lately, energy confinement time with limiter plasmas was observed to be fairly degraded with increasing heating power, and it was also found to recover with the diverted plasmas, i.e. H-mode. If such a trend continues, the divertor concept should be applied to INTOR. Possibility of H-mode operations with the pumped limiter, however, is still open, and more elaborate researches should be needed.

Maximum heat load on collector plates

Capability in removal of heat has some differences between the limiter and divertor plates, stemming from their configurations. The pumped limiter has to accommodate an exhausting space behind the limiter plates, and the limiter shape must have a tip. The capability of heat removal at the limiter tip is weaker than the plate because of its structural restriction. At the tip poloidal magnetic field also is normal to the surface, then the limiter tip must be far away from the main plasma edge so as to reduce the heat load at it. The fact could surely lead to a large demand of evacuation system.

Life of collector plates

The limiter plates of low-Z materials suffer severe erosion due to their high sputtering yields. For instance, the erosion rate of low Z materials might be about 100 cm/year in continuous operation, assuming no redeposition of sputtered materials. Sputtered materials however could be instantaneously ionized in front of the plates, and they would have high probability in returning back to the plates and redepositing on them. Some analyzing codes disclose that the net erosion rate of low-Z materials is significantly reduced to a few cm per year. The lifetime of the low-Z limiter is evaluated to be a few years.

In the high-density, low-temperature divertor case, the collector plates could hardly be eroded, employing refractory materials as a plate. The lifetime of the divertor plates might be certainly long. The divertor plates would rather suffer the redeposition of the first wall materials, which could govern the lifetime.

Pumping requirement

In the pumped limiter case, the tip of the limiter plates has to locate far away from the edge of the main plasmas due to its weak heat removability. Therefore, particle flux going into the chamber for pumping behind the limiter plate is limited to a small part of the total particle flux to the limiter. The fact demands a large pumping speed of more than 10^5 l/s in the pumped limiter case.

The high-density, low-temperature plasmas near the divertor plates produce concomitantly high pressures of neutral D-T and He gases. The moderate requirement of a evacuation system ($10^4 - 10^5$ l/s) could be enough to remove the helium ash at the same rate as the alpha production.

Torus size

The magnetic configuration of the divertor plasmas possesses magnetic null points at the main plasma edge. The presence of the null points surely enlarge a plasma volume compared with the limiter plasmas. Moreover, the divertor region is necessary beyond the null points, which furthermore expands a room for plasmas. Eventually, the size of toroidal coils, which is practically tantamount to the torus size, swells significantly. The INTOR cost study disclosed that the size of the toroidal coils with the limiter is reduce by 15 % from that with the divertor, which results in 12 % reduction in cost including power supply mentioned later.

Poloidal coil power supply

The divertor plasmas evidently need larger poloidal coil current than the limiter plasmas due to the presence of the null points at the main plasma edge. In the single null configuration like INTOR, in addition to the large coil current, the asymmetry increases forces on the toroidal coils, which leads to strong support structures and ultimately to large torus size. The poloidal power supply with the divertor, which occupies a major part of the total power supply, is bigger than that with the limiter.

In the above, comparisons between the divertor and pumped limiter are made from both sides of plasma physics and technology, with some emphasis placed on physics. On the basis of the above evaluations. It was recommended as a result of Phase-Two-A (Part 1) INTOR Workshop studies that the single-null poloidal divertor should be the reference impurity control option, and that the pumped limiter should be retained as a design option.

5. Low-temperature, high-density divertor plasmas

The most reliable impurity control concept for INTOR could be at present the divertor with low-temperature, high-density plasmas near the plates.

Those low-temperature in divertor plasmas were observed in Doublet III at first time [4], and after that they were also reproduced in ASDEX and PDX. Especially note that the results from Doublet III are remarkably important for INTOR, because they have no special room for a divertor and their shape is open-type similar to the INTOR divertor.

Those interesting experimental results stimulated studies on divertor analyses and some elaborate codes have been developed to predict the low-temperature, high-density divertor operation for INTOR.

5.1 Simulation of Doublet III experiments

Major results of the single-null poloidal divertor experiments in Doublet III are as follows [4]

- Metal impurities, typically titanium, are reduced by about one order, changing from limiter to divertor discharges, especially they are negligibly small in high density discharges.
- Neutral hydrogen gas pressures near the divertor reach an order of 10^{-3} Torr, which are larger by two orders than those in limiter discharges. Furthermore, in helium gas injection cases, helium gas pressure reach 10^{-4} Torr, which would result in reduction in pumping requirement.
- Radiation losses from the divertor region increase with increasing plasma densities and get to one half of the input power.
- High-densities ($\geq 1 \times 10^{20} \text{ m}^{-3}$), low-temperature ($T_e \approx 8 \text{ eV}$) plasmas near the divertor plates are observed even under conditions of

NBI heating, 4-5 MW.

The divertor analysis code consist of hydrodynamic equations of divertor plasma coupled with neutrals analyzed by a Monte Carlo method. The validity of the divertor code was checked by capability in explanation of experimental results.

Comparisons of densities and temperatures between Doublet III experiments and code analyses are displayed in Fig. 1. It can be found that the code fairly well explains the experiments.

5.2 Plasma parameter for the INTOR divertor

The code mentioned above can predict plasma parameters of the INTOR divertor, which are mainly dependent upon heat and particle fluxes flowing into the divertor from the main plasmas. Densities and temperatures near the divertor plates are shown in Fig. 2 as a function of the particle fluxes with as a parameter of the heat fluxes. Outstanding features are that plasma temperatures decrease below 10 eV beyond a certain value of the particle fluxes and that densities increase over 10^{20} m^{-3} near the plate. In high-density, low-temperature divertor plasma, the code also predicts that radiation losses by hydrogen neutrals amount to over 50 % of the input power.

The above result is preliminary, and adoption of such a low-temperature concept to the INTOR reference should need more evaluations. In any way, it is likely that the INTOR divertor plasmas would be in a low-temperature high-density regime. The code also includes no impurities, and the future development should evolve elaborate hydrogen atom and molecular effects and plausible impurity behaviors. The consistency between the divertor and the main plasma moreover should be paid heeds to, and operating conditions must be made clear, which make sure the low-temperature and high-density divertor plasma operation.

6. Conclusions

- 1) The single-null poloidal divertor concept could be the plausible impurity control in the next device, and it is recommended to be as a reference in INTOR
- 2) The divertor configuration of INTOR is open type due to poloidal coils exterior to toroidal coils, the reliable code predicts high probability of high-density, low-temperature plasmas near the plate.
- 3) The pumped limiter option is important, particularly in an aspect of its simplicity. Its potential to the extension into commercial reactors should be taken into considerations.

References

- [1] INTOR GROUP, International Tokamak Reactor: Zero Phase (Rep. Int. Tokamak Reactor Workshop Vienna, 1979), International Atomic Energy Agency, Vienna (1980); see also Summary in Nuclear Fusion 20 (1980) 349.
- [2] INTOR GROUP, International Tokamak Reactor: Phase One (Rep. Int. Tokamak Reactor Workshop Vienna, 1980-81), International Atomic Energy Agency, Vienna (1982); see also Summary in Nuclear Fusion 22 (1982) 135.
- [3] INTOR GROUP, International Tokamak Reactor: Phase Two A Part 1 (Rep. Int. Tokamak Reactor Workshop Vienna, 1981-83), International Atomic Energy Agency, Vienna (1983); see also Summary in Nuclear Fusion 23 (1983) 1513.
- [4] See, e.g. the following papers: SHIMADA, M., et al., Nuclear Fusion 22 (1982) 643; SENGOKU, S., et al., to be published in Nuclear Fusion; SHIMADA, M., et al., Phys. Rev. Lett. 47 (1981) 796; NAGAMI, M., et al., in Plasma Physics and Controlled Nuclear Fusion Research (Proc. 8th Int. Conf. Brussels, 1980) Vol. 2, IAEA, Vienna (1981) 367; YOKOMIZO, H., et al., in Plasma Physics and Controlled Nuclear Fusion Research (Proc. 9th Int. Conf. Baltimore, 1982) Vol. 3, IAEA, Vienna (1983) 173.

Table 1. INTOR Major Parameters

| | |
|--|---|
| PLASMA | |
| Plasma major radius, R_p | 5.3 m |
| Plasma radius, a | 1.2 m |
| Plasma elongation, K | 1.6 |
| Burn average beta, $\langle\beta\rangle$ | 5.6 % |
| Average ion temperature, $\langle T_i \rangle$ | 10 keV |
| Average ion density, $\langle n_i \rangle$ | $1.4 \times 10^{20} \text{ m}^{-3}$ |
| Energy confinement time, τ_E | 1.4 s |
| Plasma current, I_p | 6.4 MA |
| Field on chamber axis, B_T | 5.5 T |
| Peak thermonuclear power, P_{th} | 620 MW |
| Neutron wall load, P_n | $1.3 \text{ MW}\cdot\text{m}^{-2}$ |
| OPERATION | |
| Burn time Stage I/II and III | 100/200 s |
| Duty cycle, Stage I/II and III | 70/80 % |
| Number of pulses (lifetime) | 7×10^5 |
| Maximum availability goal | 50 % |
| IMPURITY CONTROL | |
| Method | Singl-null poloidal divertor |
| Collector | Low plasma temperature at plate: W, medium plasma temperature: Be |
| Power to divertor | 80 MW |
| FIRST WALL | |
| Power to first wall | 44 MW |
| Material | SS316 |

Table 2 Comparison between poloidal divertor and toroidal pumped limiter

| Items | Divertor | Pumped Limiter |
|---|--|---|
| A. Plasma parameters in front of collector plates | High potential of high density ($> 10^{20} \text{ m}^{-3}$) and low temperature ($\leq 30 \text{ eV}$) | Strong tendency of medium density ($< 10^{20} \text{ m}^{-3}$) and medium temperature (50-200 eV) |
| B. Impurity controllability | Small impurity release from collector plates and moreover considerable capability in preventing impurities from going into main plasma | Large impurity release from low-Z collector plates and more chances for impurities to enter main plasma |
| C. Materials for collector plates | (Low-High) Z | Low-Z |
| D. Erosion of first wall | Concentrated near divertor and some concerns in shielding performance of scrape-off plasmas | Concentrated near limiter plates and redeposition onto them |
| E. Effects on main plasma confinement performance | H-mode | L-mode (degradation in confinement time) |
| F. Heat removability of collector plates | $2 \sim 3 \text{ MW}\cdot\text{m}^{-2}$ | $2 \sim 3 \text{ MW}\cdot\text{m}^{-2}$ at plate and $\sim 1 \text{ MW}\cdot\text{m}^{-2}$ at plate tip |
| G. Life of collector plates | Significantly long if no redeposition of first wall materials | Short (e.g. 1 year even if redeposition of sputtered material) |
| H. Pumping Requirement | $(1 \sim 10) \times 10^4 \text{ l/s}$ | $\geq 10^5 \text{ l/s}$ |
| I. Torus size | Fairly large torus due to presence of null points and divertor room | Relatively small |
| J. Poloidal coil power supply | Large due to large poloidal coil current | Relatively small |

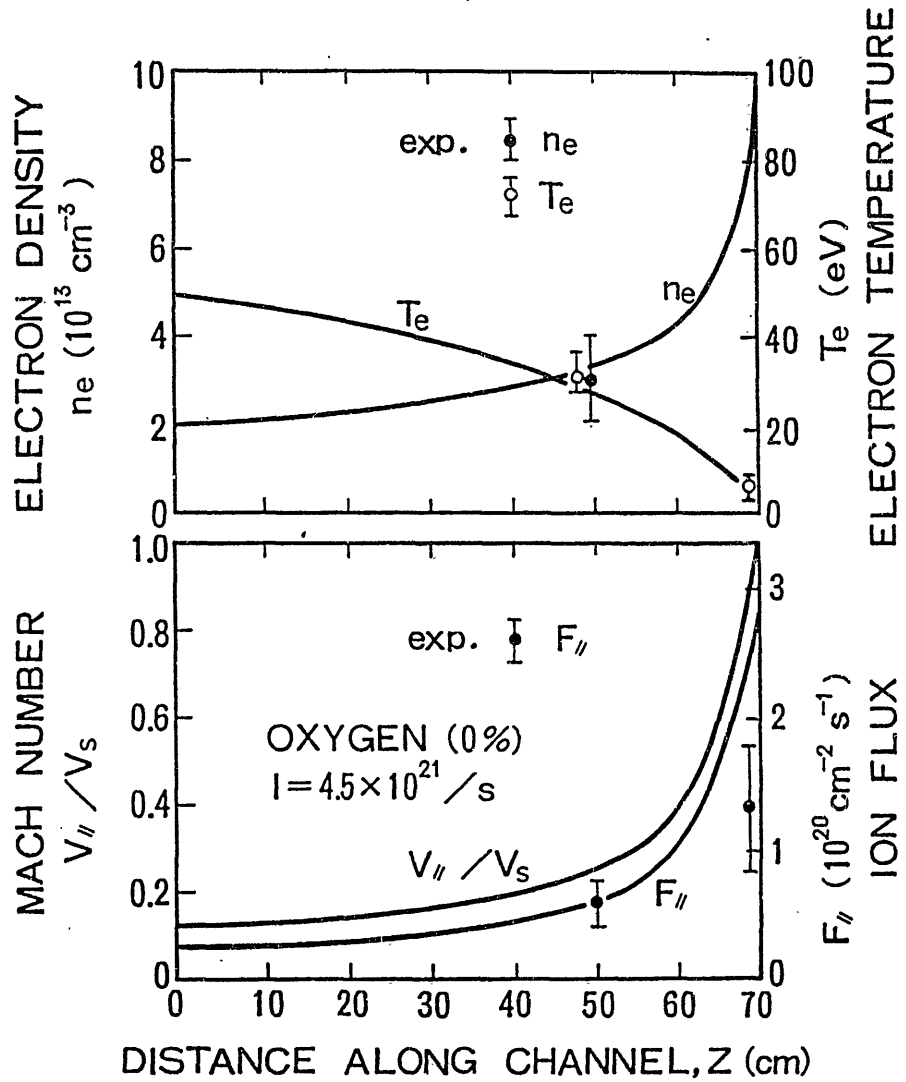


Fig. 1 Comparison between the calculated and measured values of the divertor plasma quantities.

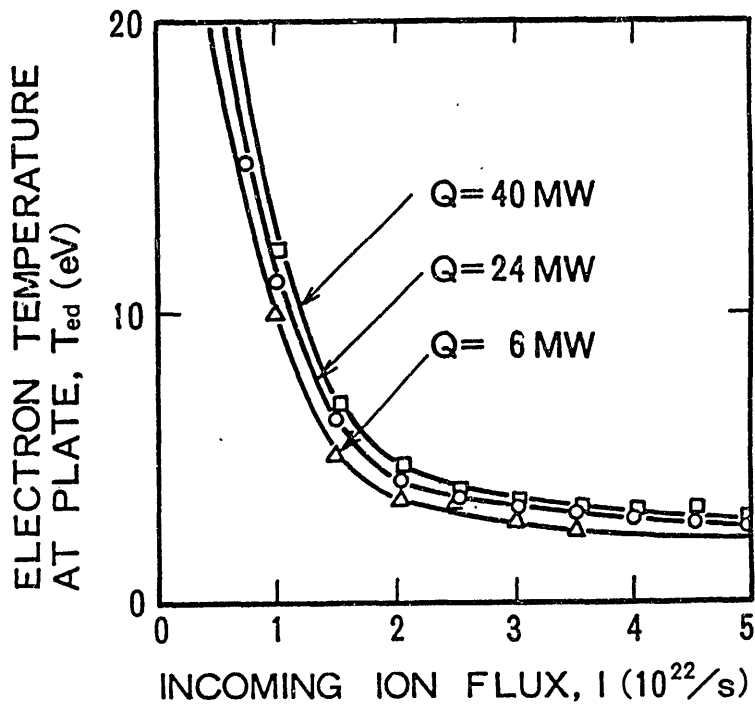
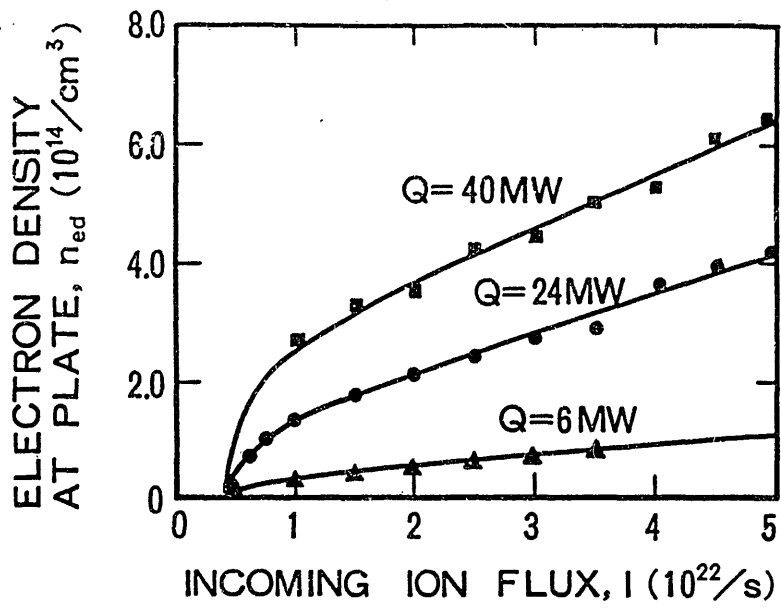


Fig. 2 Peak electron densities and temperatures near the divertor plate as a function of incoming ion fluxes for INTOR.

Numerical Simulation of Pellet Injection into Heliotron-E

Yuji Nakamura

Masahiro Wakatani

Plasma Physics Laboratory

Kyoto University

Gokasho, Uji

Density increase by the pellet injection into magnetically confined plasmas is an interesting subject from the point of view of the transport theory. Recently the pellet injection experiment becomes popular in tokamaks^{1) ~ 4)} and stellarators⁵⁾ and the remarkable result of $n_e(0) \tau_E \sim 8 \times 10^{13} \text{ cm}^{-3} \text{ sec}$ is obtained in Alcator C, where $n_e(0)$ denotes a central electron density and τ_E is energy confinement time.

There are two important processes in the analyses of pellet injection. One is ablation process and the other is transport process of the deposited particles. The ablation process is calculated by Milora-Foster model⁷⁾ and a self-limiting process which is the effect of cooling the target plasma by the pellet on the ablation rate. Typical ablation profiles along the pellet injection pass are shown in Fig. 1. Here we assume $n_e(r) = 6.0 \times 10^{19} (1 - (r/a)^2) + 5 \times 10^{17} \text{ [m}^{-3}]$ and $T_e(r) = 600(1 - (r/a)^2) + 10 \text{ [eV]}$ and total particle number of the pellet 5.86×10^{19} . These data are consistent with the pellet injection experiment into Heliotron E with a major radius $R = 2.2 \text{ m}$ and an average minor radius $a = 20 \text{ cm}$.

The particle deposition profile is coupled with the numerical code⁸⁾ to study the transport process in Heliotron E. The currentless plasma was produced by decreasing the ohmic heating current from 10 kA to 500 A in the numerical calculation. The transport coefficients, $D = D^{\text{neo}} + 5.0 \times 10^{18} / n_e \text{ [m}^2/\text{sec}]$, $\chi_e = \chi_e^{\text{neo}} + 1.5 \times 10^{19} / n_e \text{ [m}^2/\text{sec}]$ and $\chi_i = \chi_i^{\text{neo}}$ were assumed. The neutral beam injection heating of 1.44 MW was calculated by using the linearized Fokker-Planck equation. The

pellet of total particles, 4.2×10^{19} , was injected with the velocity of 1000 m/s. The radiation loss was included through an assumed Z_{eff} .

In Fig. 2, the pellet ablation profile, $T_e(r)$, $T_i(r)$ and $n_e(r)$ are shown after the pellet injection at $T = 150$ msec. Fig. 3 shows time evolution of various parameters. The average density \bar{n}_e is increased from $2.5 \times 10^{19} [\text{m}^{-3}]$ to $5 \times 10^{19} [\text{m}^{-3}]$. The abrupt increase of $n_e(0)$ means that the pellet goes across the magnetic axis. The central temperature $T_e(0)$ and $T_i(0)$ almost recover the values before the pellet injection. The confinement time τ_E and τ_p also increase according to the assumed transport coefficient (Alcator-like scaling). The pressure profile is shown in Fig. 4. The peaked profile just after the pellet injection shows non-adiabatic heating occurs near the central region. When beta value increases by the pellet injection, MHD stability against the pressure driver modes becomes an important factor to determine the pellet size and velocity.

The comparison between the numerical results and the pellet injection experiment carried out in this January is under way.

References

- (1) S. L. Milora et al., Nucl. Fusion 20 (1980) 1491.
- (2) C. A. Foster et al., Nucl. Fusion 17 (1977) 1067.
- (3) S. L. Milora et al., Phys. Rev. Lett. 42 (1979) 97.
- (4) S. L. Milora et al., Nucl. Fusion 22 (1982) 1263.
- (5) WVII-A Team, 9th IAEA Conf. (Baltimore, 1982) IAEA-CN-41/45.
- (6) S. L. Milora and C. A. Foster, IEEE Trans. Plasma Sci. PS-6 (1978) 578.
- (7) W. A. Houlberg et al., ORNL/TM-6549 (1979).
- (8) T. Amano and M. Okamoto, JAER-M8420 (1979).

Figure Captions

- Fig. 1 Ablation rate profile along the pellet path.
- Fig. 2 Profiles of abration rate, electron density and plasma temperatures of Heliotron E NBI heated currentless plasma. Pellet is injected at $T=150$ msec.
- Fig. 3 Time evolution of plasma parameters corresponding to Fig. 2.
- Fig. 4 Behavior of pressure profile after the pellet injection.

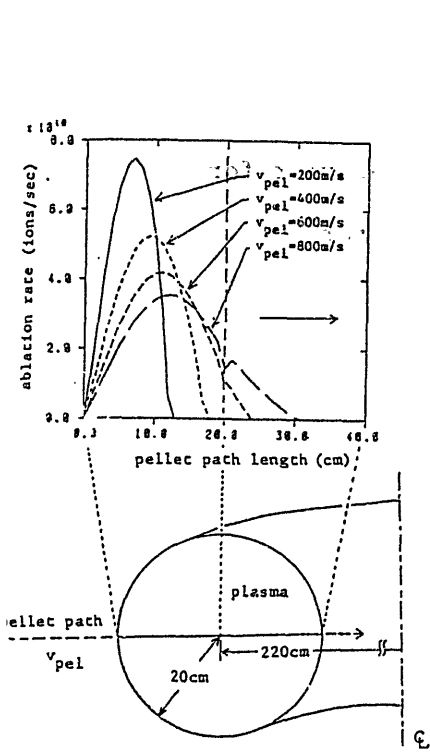


Fig. 1

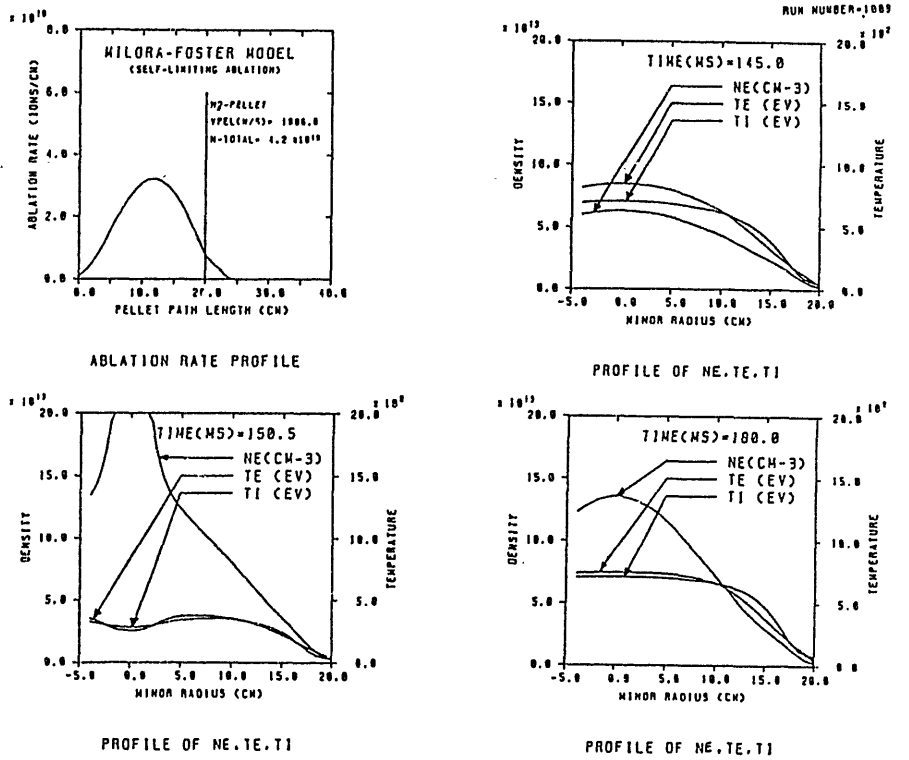


Fig. 2

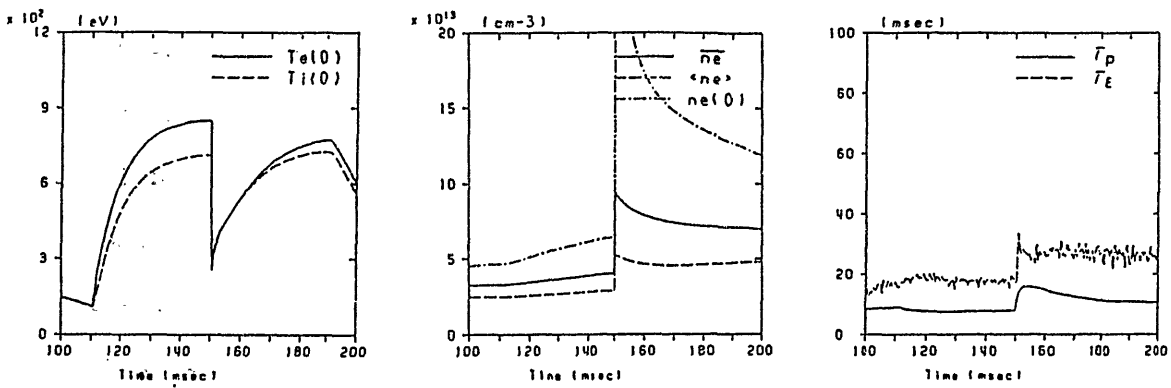


Fig. 3

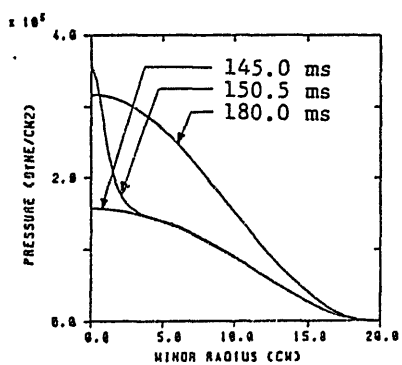


Fig. 4

Numerical Analyses of Plasma and Neutral Particle Behavior for
Poloidal Divertor in Fusion Experimental Reactor

Masayoshi SUGIHARA, Seiji SAITO*,
Shigehisa HITOKI** and Noboru FUJISAWA

Japan Atomic Energy Research Institute
Naka-machi, Naka-gun, Ibaraki, Japan

1. Introduction

Recent design works of the experimental fusion reactors have stimulated the experimental [1-4] and theoretical [5-9] studies on the heat removal and related impurity control measures. A possibility of the helium ash exhaust using a model poloidal divertor was discussed in the earlier reports [5,6] by means of a Monte Carlo simulation of the neutral particles and ions in the divertor chamber. Their model [5] was based on the simple sheath theory as to the estimation of the scrape-off variables that were assumed to be uniform along the magnetic field line. The observations of the cold and dense divertor plasma in DIII[1,2] and ASDEX [3] experiments have indicated the strong inhomogeneity of the scrape-off plasma along the field line. This feature has also been numerically investigated on the basis of the fluid model of the scrape-off plasma [7-9]. In this paper, the possible attainment of the high density operation in the FER divertor is investigated using a self-consistent treatment for the scrape-off plasma and neutrals. The scrape-off plasmas are described by the fluid equations consisting of

* Hitachi Energy Research Laboratory, Hitachi, Japan
** Mitsubishi Electric Company, Tokyo, Japan

the particle, momentum and energy conservation equations along the magnetic field line. The neutral particle transport is simulated by the Monte Carlo method. Their interactions through ionization and charge exchange processes are solved self-consistently with the scrape-off plasma by an iterative procedure.

2. Model of Neutral Particle Transport [10]

2.1 Particle Tracking Method

The neutral particle motions initiated at the neutralizer plate are followed by the Monte Carlo simulation method. The particle trajectories are traced at the space intervals between space lattices. The reaction points are searched within the space interval by generating a random number according to the reaction probability.

After ionization of neutral particles, the tracking is terminated, while after the charge exchange a new velocity is assigned to the neutral particle by generating a random number according to the Maxwellian velocity distribution of the background ions. A new velocity is also given to a reflected neutral in collision with the divertor chamber wall.

The tracking of neutral particles is terminated when they return back to the main plasma region across the entrance of divertor throat, or leave the bottom of the exhausting duct.

2.2 The Physical Model

The ionization process of neutral atoms is described on the basis of the ionization rate coefficients using the Freeman and Jones formula[11] for fuel particles and Lotz's formula[12] for helium. As for the charge exchange, the Riviere's formula[13] is used. Neutral particles colliding with the chamber wall are assumed to be reflected at the rates given Ref. [14]. There are few experiments and theories concerning the dependence on θ of the reflection coefficients, except for the normal incidence[14].

The numerical calculation shows that the reflection coefficients approach to unity as θ goes to 90° [15], where θ is the incident angle measured from the normal to the surface. Therefore we assume for simplicity the linear angular dependence. Particles which are not reflected are adsorbed and then desorbed at wall temperature. The angle of reflected or desorbed particles is determined by cosine distribution based on the assumption of rough surface in molecular level. There is still large uncertainty in these reflection model, especially in low incident energy. If, for instance, mirror reflection is dominant, the estimation of the effective conductance of the evacuating duct will be much altered. Deuterium and tritium particles desorbed from the wall are in molecular form. Dominant processes for these molecules[16] are incorporated.

2.3 The scoring Method for the Neutral Distributions

Mean flight time of particles in each space lattice is obtained by following the particle trajectories at every space lattice. The neutral density distributions are calculated from the mean flight times of test particles, the total particle flux from the neutralizer plate and the volume of the space lattice[17].

3. Fluid Model

The fluid equations in conservation form derived by Braginskii[18] can be reduced to the equations along the field line[19]. The particle, momentum and energy conservation equations projected on the poloidal cross section shown in fig. 2, are given by

$$\frac{\partial}{\partial z} f_{k,z}(x,z) = S_k(x,z) + \frac{\partial}{\partial x} (D_{\perp} \frac{\partial n_k(x,z)}{\partial x}) \quad , \quad (k = D, T, He) \quad , \quad (3-1)$$

$$\begin{aligned} & \frac{\partial}{\partial z} [n_p(x,z)(2U(x,z) + z_p T_e(x,z) + T_i(x,z))] \\ & = \frac{B_T}{B_p} [S_p(x,z) + \frac{\partial}{\partial x} \{ \frac{2U(x,z)}{V_{\perp}(x,z)} D_{\perp} \frac{\partial n_p(x,z)}{\partial x} \}] \quad , \quad (3-2) \end{aligned}$$

$$\begin{aligned}
& \frac{\partial}{\partial z} [f_z(x,z) (U(x,z) + \frac{5}{2} T_i(x,z)) + q_i(x,z)] \\
& = -V_z \frac{\partial}{\partial z} P_e(x,z) + P_{ei}(x,z) + S_{Ei}(x,z) \\
& + \frac{\partial}{\partial x} [\{U(x,z) + \frac{3}{2} T_i(x,z)\} D_{\perp} \frac{\partial n_p(x,z)}{\partial x} + K_{i\perp} \frac{\partial T_i(x,z)}{\partial x}] \quad , \quad (3-3)
\end{aligned}$$

$$\begin{aligned}
& \frac{\partial}{\partial z} [\frac{5}{2} f_z(x,z) T_e(x,z) + q_e(x,z)] \\
& = V_z \frac{\partial}{\partial z} P_e(x,z) - P_{ei}(x,z) + P_r(x,z) + S_{Ee}(x,z) \\
& + \frac{\partial}{\partial x} [\frac{3}{2} T_e(x,z) D_{\perp} \frac{\partial n_e(x,z)}{\partial x} + K_{e\perp} \frac{\partial T_e(x,z)}{\partial x}] \quad , \quad (3-4)
\end{aligned}$$

where, for simplicity, the ratio of the poloidal to toroidal magnetic field is assumed to be constant along the field line. $f_{kz}(x,z)$ denotes the ion flux parallel to the z direction for D, T and α particles and $f_z(x,z)$ the total ion flux. $U(x,z)$ is expressed in terms of the average ion mass m_p and the ion flow velocity along the field line $V_{\parallel}(x,z)$ as follows:

$$U(x,z) = \frac{1}{2} m_p V_{\parallel}^2(x,z) \quad . \quad (3-5)$$

In eqs. (3-3) and (3-4), q_i and q_e are the conduction heat fluxes in the z direction for the ions and electrons, where the heat conductivities along the field line are assumed to be the classical ones.

The first terms on the right-hand side of eqs. (3-3) and (3-4) represent energies provided by the ambipolar electric field produced by the gradient of the electron pressure $P_e(x,z)$. The second terms express the collisional energy transfer between the electrons and ions. In eq. (3-4), P_r denotes the radiation loss power from the recycling hydrogen neutral and oxygen impurities. As for the hydrogen line radiation, only the first excitation level is taken into account using the excitation rate coefficient given by Johnson [20]. The power density of the oxygen radiation is calculated using a numerical fit to the non-coronal

calculation by Shimada [21]. The particle, momentum and energy sources due to ionization and charge exchange of the neutral particles are denoted by $S_k(x,z)$ ($k=D,T,He$) $S_p(x,z)$, $S_{Ei}(x,z)$ and $S_{Ee}(x,z)$.

A part of the boundary conditions are given at the divertor throat entrance; the incoming ion fluxes $f_{kz}(x,0)$, ($k=D,T$), the incoming total heat flux $Q_{TOT}(x,0)$ and the ratio of the ion to electron temperature. More restrictive conditions characterizing the scrape-off plasma come from the existence of the electrostatic sheath formed in front of the divertor plate. The first condition is the heat flux limitation [22] imposed by the sheath electric field given by

$$Q_{TOT}(x,L) = \gamma_{TOT} T_e(x,L) f_z(x,L) \quad , \quad (3-6)$$

where γ_{TOT} is the total heat transmission coefficient. The second one is the sound speed condition [23] in the following:

$$U(x,L) = \frac{1}{2} \{ z_p T_e(x,L) + T_i(x,L) \} \quad , \quad (3-7)$$

In addition, the following continuity condition for the ion heat flux by conduction is included,

$$\left. \frac{\partial q_i}{\partial z} \right|_{z=L} = 0 \quad . \quad (3-8)$$

4. Evaluation of FER divertor characteristics [24]

The scrape-off plasmas in the outboard-side divertor chambers of FER are estimated numerically using the simplified model configuration illustrated in fig. 2(a).

The ion flux reaching the divertor plate increases due to reionizations of the recycling neutral particles. The dependence of the scrape-off plasma variables on the incoming ion flux is analyzed with use of the divertor chamber with the short length of 50 cm and relatively large width of 30 cm, and with the high pumping speed of 2.5×10^5 l/s.

The calculated results of the peak electron density and temperature at the divertor plate are shown in fig. 2 as a function of the incoming ion flux I under FER baseline condition of the heat flux of 20 MW to the outboard-side of each divertor. The heat and particle flux are assumed to have exponential distributions whose e-folding distances are 7 cm. The ratio of the poloidal to toroidal magnetic field is set to $B_p/B_T = 0.1$.

In fig. 2(b), case (A) and (B) show the case without and with the line radiations from the recycling hydrogen neutrals and the 1% oxygen impurities, respectively. The corresponding radiated power amounts to 40% of the total power for the hydrogen and 25% for the 1% oxygen impurities as shown in Fig. 2(c). The effect of the radiation cooling is to reduce the electron density with little variation of the electron temperature, as shown in fig. 2(b). The further study will, however, be needed concerning the more elaborate estimation of the radiation loss power in the very high density and low temperature region [25].

The two-dimensional plots of the electron temperature and density obtained with the radiation losses are shown in figs. 3(a) and (b) for the incoming ion flux $I = 2.5 \times 10^{22}/s$. The electron temperature on the separatrix line is about 40 eV at the divertor throat entrance and rapidly decreases to about 3 eV in front of the divertor plate. The electron density varies from about $3 \times 10^{13}/cm^3$ at the throat entrance up to about $2 \times 10^{14}/cm^3$ along the separatrix line.

In fig. 4, the electron density near the plate is shown for various heat flux as a function of incoming ion flux.

In order to evaluate the pumping requirement for the helium ash exhaust, we obtain the relation between the effective conductance of the exhaust system and the backflow fraction of the neutrals, f_{bf} . The backflow fraction is defined as the ratio of the neutral flux returning to the main plasma to the incoming ion flux. Since the required pumping

speed is expected to be higher for the lower incoming ion flux, we investigate it for the low incoming ion flux of $3 \times 10^{22}/s$. The results are shown in fig. 5. FFR standard condition gives the backflow fraction, $f_{bf} = 0.86$ for $2I = 6 \times 10^{22}/s$ and helium accumulation of 5%. Figure 5 shows that the effective pumping speed must be larger than 2.0×10^4 ℓ/s to keep the helium concentration lower than 5%. The required pumping speed is reduced by a factor of 10, due to the density enhancement in scrape-off layer, from the previous estimation $\sim 2 \times 10^5$ ℓ/s [5], where the scrape-off plasma density ($\sim 2 \times 10^{12}/cm^3$) and temperature (250 eV) are assumed based on the simple sheath theory.

5. Numerical simulation of DIII divertor

The high density ($\sim 10^{14}/cm^3$) and low temperature (3 ~ 10 eV) plasmas in front of the divertor plate have been measured on DIII experiments under 1.0 MW beam heated condition [2]. We simulate these experiments by the numerical code developed.

The configuration used for the simulation is shown in the insert of fig. 6. The experiments indicate that the heat flux into the divertor throat is about 0.5 MW and the e-folding distances of the heat flux and particle flux are 1.8 cm and 3 cm, respectively. Figure 6 shows the results obtained under these flux conditions. The results without and with the radiation loss from the neutral hydrogen and 1% oxygen impurities are denoted by case (A) and (B), respectively. The calculated values of the density and the incoming ion flux are roughly consistent with the observed ranges ($n_{ed} \sim 10^{14}/cm^3$, $I = 2 \sim 4 \times 10^{21}/s$) [2].

Another important feature of DIII experiment is the nonlinear dependence of the density at the divertor plate n_{ed} on the main plasma density \bar{n}_{main} which is roughly given by $n_{ed} \propto \bar{n}_{main}^3$ [1,2,26]. This feature can well be understood by our numerical model. By using the momentum

conservation equation (3-2) and by neglecting the momentum source term, the following scaling can be easily derived in the high density and low temperature region:

$$n_{ed} \propto Q(L)^{-2} n_{eth}^3 \quad (5-1)$$

where $Q(L)$ is the total heat flux to the divertor plate and n_{eth} is the electron density at the throat entrance. The scaling (5-1) is also satisfied by the numerical results shown in fig. 7. It fairly well explains the observed nonlinear dependence provided that the density at the throat n_{eth} can be assumed to be proportional to the main plasma density \bar{n}_{main} . It should also be remarked that the radiation cooling introduces a more rapid variation of the density at the plate n_{ed} with the density at the throat entrance n_{eth} .

6. Concluding remarks

The self-consistent numerical evaluation for the transport of the scrape-off plasmas and the neutral particles was carried out to elucidate the performance of the divertor in FER. The analyses for FER baseline condition indicated the possibility of the high-density and low-temperature plasma in front of the divertor plate even in the case of the low incoming ion flux. The numerical calculations for FER divertor also suggest the intense radiative cooling (about 40% to 65% of total incoming heat flux is radiated in the divertor chamber) and the low required pumping speed for helium ash exhaust (about 2.0×10^4 l/s).

The numerical calculation for DIII under 1.0 MW beam heated condition yielded the electron density and temperature roughly consistent with the experiments.

Reference

- [1] M. Shimada, et al., Phys. Rev. Lett. 47, 796 (1981).
- [2] S. Sengoku, et al., to be published in Nucl. Fusion.

- [3] Y. Shimomura, M. Keilhacker, K. Lackner, H. Murmann and G. Siller, IPP III/80 (1982).
- [4] R.J. Fonk, et al., J. Nucl. Mater. 111 & 112, 343 (1982).
- [5] Y. Seki, Y. Shimomura, K. Maki, M. Azumi, and T. Takizuka, Nucl. Fusion 21, 1213 (1980).
- [6] D. Heifetz, D. Post, M. Petravic, J. Weisheit, and G. Bateman, J. Comput. Phys. 46, 309 (1982).
- [7] M. Petravic, D. Post, D. Heifetz, and J. Schmidt, Phys. Rev. Lett. 48, 326 (1982).
- [8] M. Petravic, D. Heifetz, D. Post, W. Langer and C. Singer, Proc. Ninth Int. Conf. on Plasma Physics and Controlled Nuclear Fusion Research, Baltimore, 1982, IAEA-CN-41/D-3-2.
- [9] M.F.A. Harrison, P.J. Harbour, and E.S. Hotston, Nucl. Technol./Fusion 3, 432 (1982).
- [10] S. Saito, M. Sugihara, N. Fujisawa, T. Abe and K. Ueda, Nucl. Technol./Fusion 4, 498 (1983).
- [11] R.L. Freeman and E.M. Jones, CLM-R 137, Culham Laboratory (1974).
- [12] W. Lotz, Z. Phys. 216, 241 (1968).
- [13] A.C. Riviere, Nucl. Fusion 11, 363 (1971).
- [14] G.M. McCracken and P.E. Stott, Nucl. Fusion 19, 889 (1979).
- [15] O.S. One and M.T. Robinson, J. Nucl. Mater. 76 & 77, 370 (1978),
- [16] D.E. Post, D.B. Heifetz and M. Petravic, J. Nucl. Mater. 111/112, 393 (1982).
- [17] M.H. Hughes and D.E. Post, J. Comput. Phys. 28, 43 (1973).
- [18] S.I. Braginskii, Reviews of Plasma Physics, Vol. 1, Consultants Bureau, New York, 1965.
- [19] C.E. Singer and W.D. Langer, PPPL-1920 (1982).
- [20] L.C. Johnson, Astrophys. J. 174, 227 (1972)
- [21] M. Shimada, et al., JAERI-M 9862 (1981).

- [22] G.D. Hobbs and J.A. Wesson, Plasma Physics 9, 85 (1967).
- [23] D. Bohm, Characteristics of electrical Discharges in Mangetic Fields P.77 (A. Guthrie and R.K. Wakerling, Eds.), McGraw-Hill.
- [24] S. Saito, M. Sugihara and N. Fujisawa, to be published J. Nucl. Mater.
- [25] J. Weisheit, J. Phys. B8, 2556 (1975).
- [26] M.A. Mahdavi, et al., J. Nucl. Mater. 111 & 112, 355 (1982).

Figure Captions

- Fig. 1 Schematic drawing of divertor chamber.
- Fig. 2 Characteristics of the scrape-off plasmas in FER divertor chamber:
- (a) Model divertor chamber for FER.
 - (b) Peak electron densities and temperatures at the divertor plate as a function of the incoming ion flux. Case (A) and (B) show the results calculated without and with the radiation loss from the neutral hydrogen and 1% oxygen impurities.
 - (c) Corresponding radiation loss power as a function of the incoming ion flux.
- Fig. 3 Two-dimensional plots: (a) electron temperature distribution, (b) electron density distribution in the FER divertor chamber.
- Fig. 4 Peak electron densities at the divertor plate as a function of the incoming ion flux for various heat flux.
- Fig. 5 Relation between the backflow fraction and the effective pumping speed for the FER divertor. ($I = 2.5 \times 10^{22}/s$)
- Fig. 6 Peak electron densities and temperatures at the divertor plate as a function of the incoming ion flux. (DIII) Case (A) and (B) show the results calculated without and with the line radiation loss from the neutral hydrogen and 1% oxygen impurities.
- Fig. 7 Relation between the peak electron density at the divertor plate and the peak electron density at the throat entrance. (DIII)

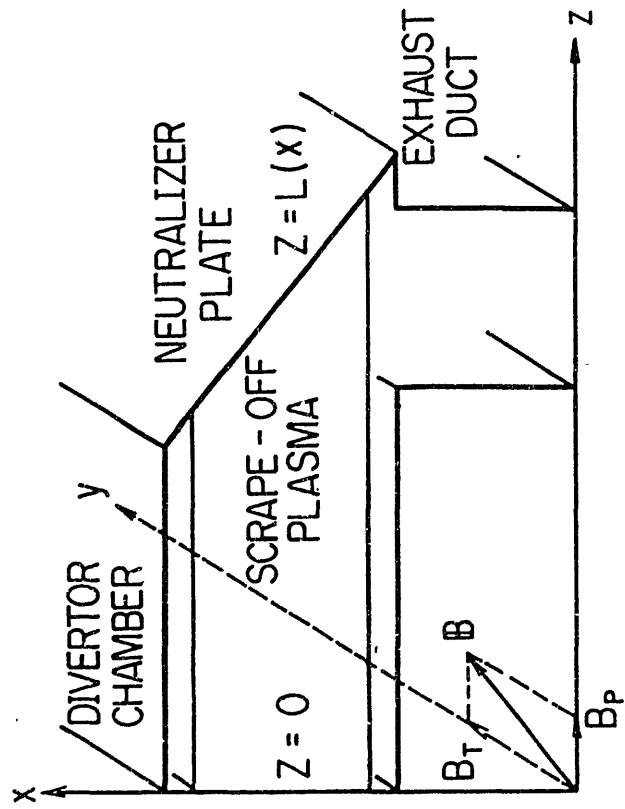


Fig. 1

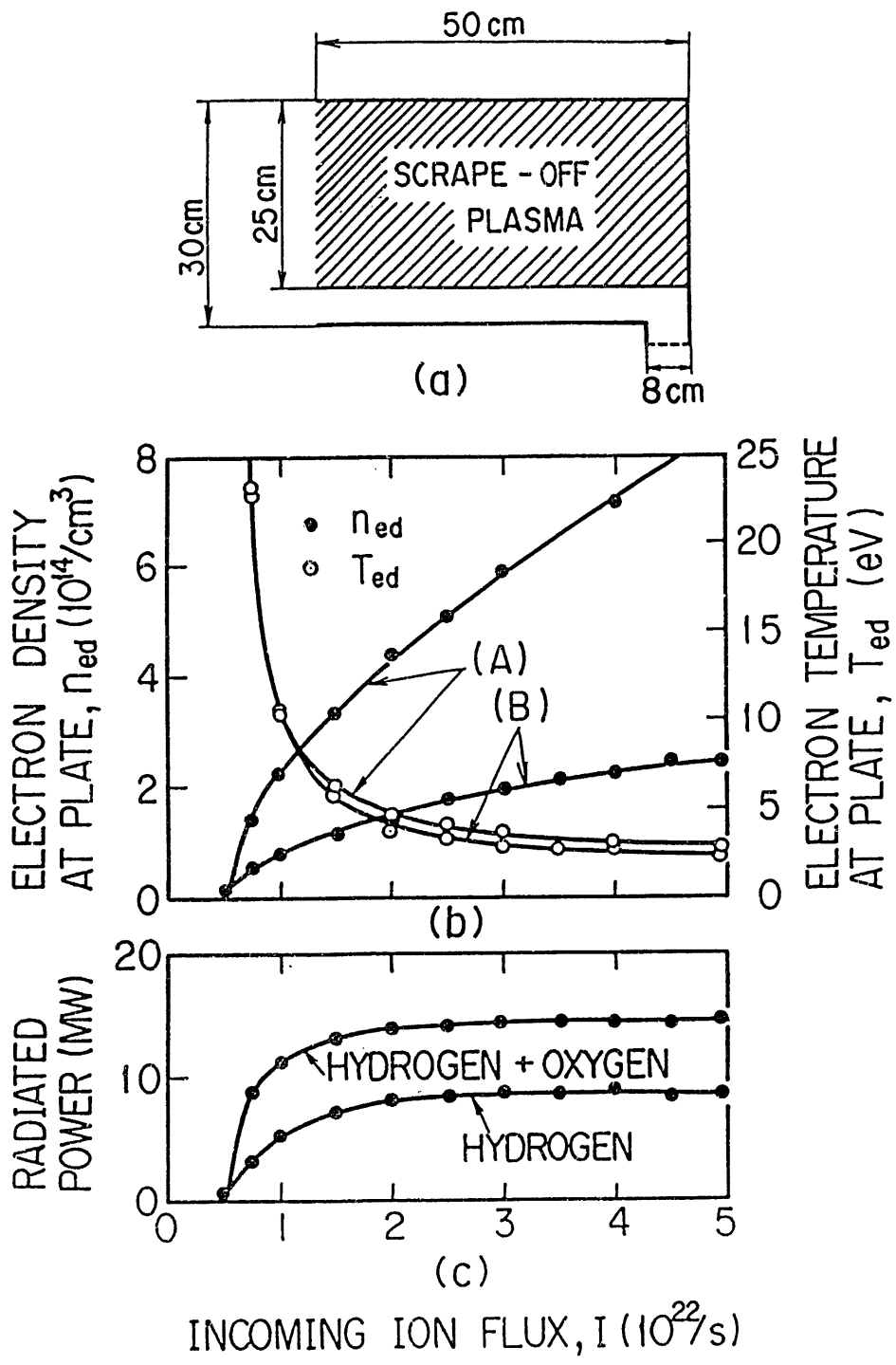
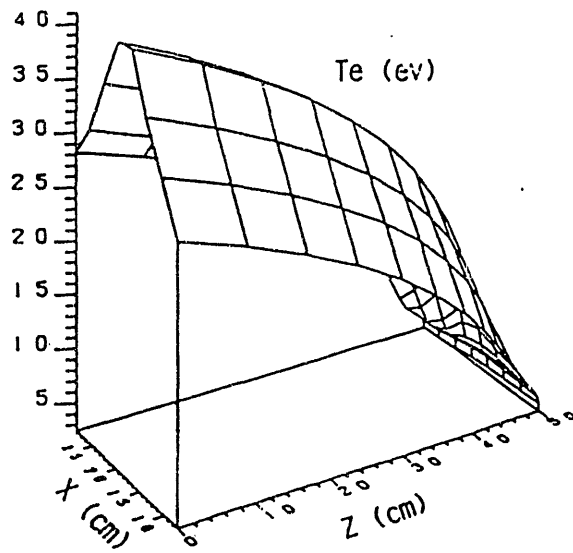
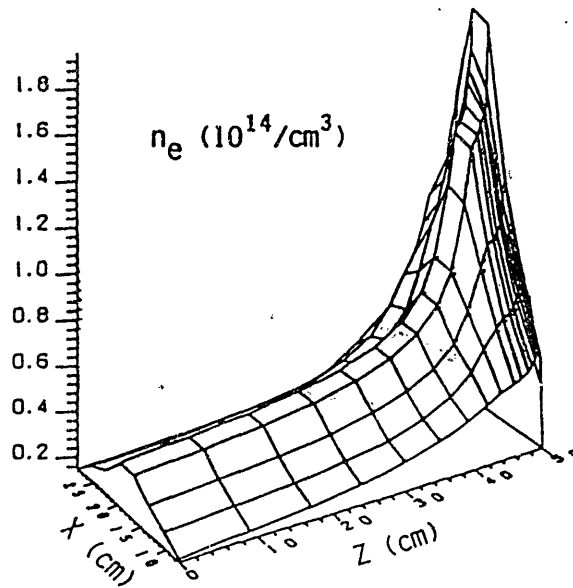


Fig. 2



(a)



(b)

Fig. 3

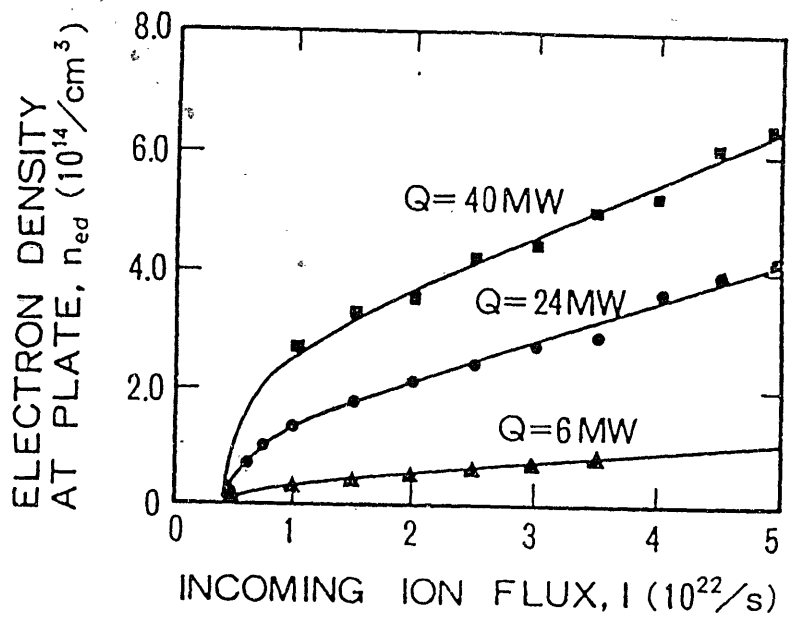


Fig. 4

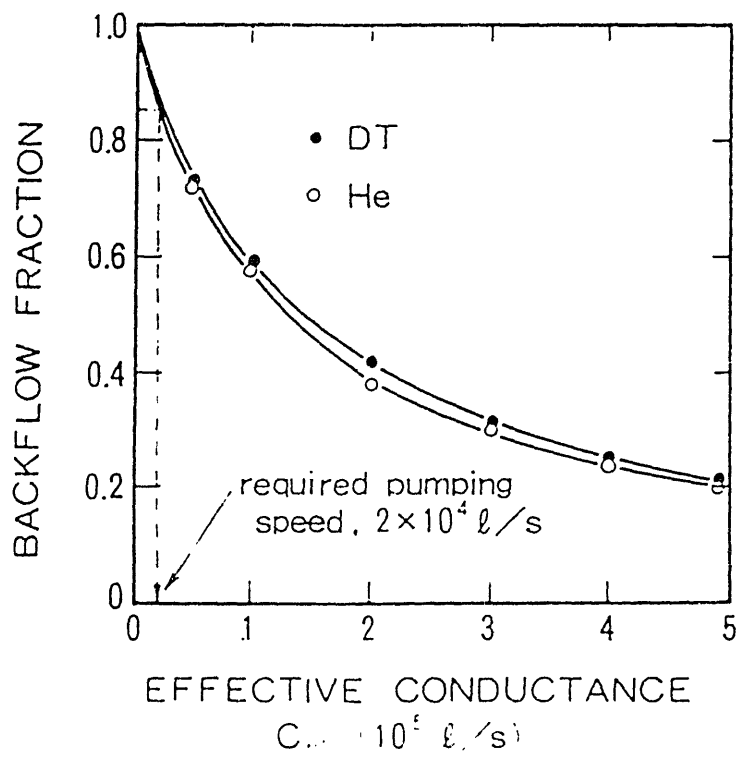


Fig. 5

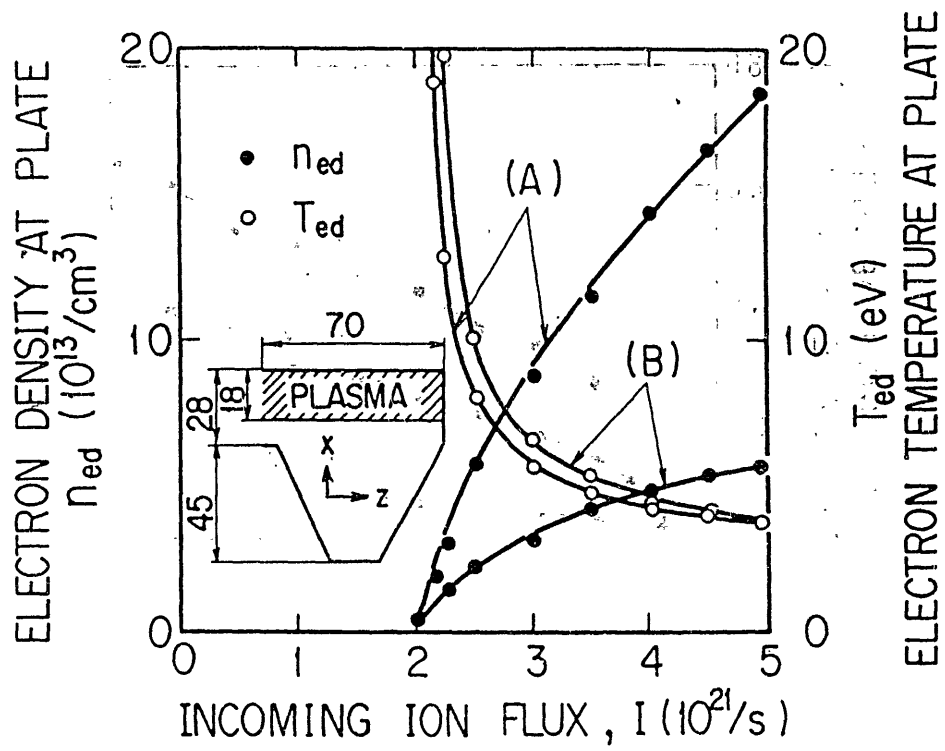


Fig. 6

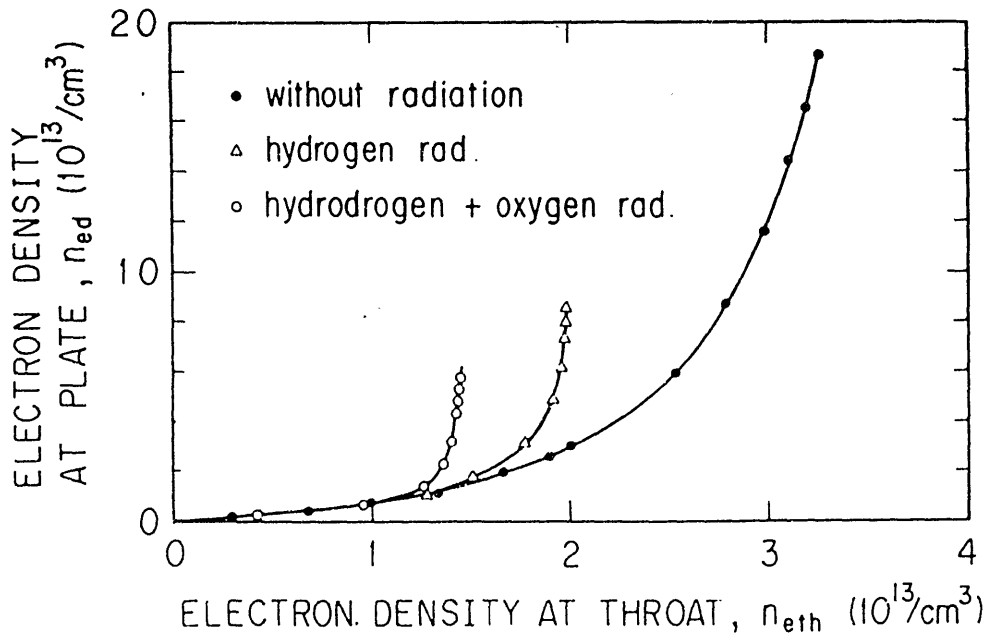


Fig. 7

ERGODIC MAGNETIC LAYER*

N. Ohyanu, J. deGrassie and N. Brooks

GA Technologies Inc., P.O. Box 85608, San Diego, CA 92138

The primary function of an ergodic magnetic layer (EML) is to create a cold, dense plasma boundary in which the radial heat flux from the plasma core is converted into radiated power by impurities. Such a radiating mantle is the safest design for removing the high heat load generated in a tokamak reactor. An ergodic magnetic structure is obtained by overlapping the primary and secondary island modes created by an external helical perturbation field. The required field strength is small – typically $\tilde{B}_{r_{max}} / B_t \sim 10^{-3}$ – and thus the required coil current is minimal. The addition in the ergodic layer of higher parallel heat transport to the ever-present cross field transport will suppress the temperature in the ergodic layer below 100 eV. Since radiative power loss from low-Z impurities is highest for temperatures below 100 eV, a large volume of radiating plasma can be generated in the ergodic magnetic layer. For INTOR parameters, 70 MW of power can be radiated away by an ergodic layer with a thickness of ~ 10 cm, an electron density of $7 \times 10^{13} \text{ cm}^{-3}$ and a neon impurity concentration of 1%. If most of the heat flux is radiated away, the temperature at the limiter may be reduced below the sputtering threshold. With heat flux and particle recycling spatially decoupled, a small limiter can be used to localize recycling near a pumping port for effective pumping of helium ash.

The objective of the EML experiment on the TEXT tokamak is to examine whether an ergodic magnetic structure can exist without inducing deleterious MHD

*Work Supported by U. S. DOE Contract DE-AT03-84ER51044.

effects such as plasma disruptions, and whether such a structure alters the heat transport in the edge. In the TEXT experiment ($R = 100$ cm, $a = 27$ cm, $B_T = 1.5 - 2.8$ T, $I_p = 150 - 400$ kA, $2 < \bar{n} < 8 \times 10^{13}$ cm⁻³), the helical perturbation field with mode number $m/n = 7/2$ or $7/3$ is generated by eight modular coils. For moderate helical perturbation fields, a stationary ergodic magnetic structure is produced at the plasma boundary. No deleterious effects on the core plasma have been observed. For sufficiently high helical perturbation field, however, the plasma disrupts.

Various diagnostic measurements have demonstrated that heat flux transport through the boundary layer is modified significantly by the ergodic magnetic structure. The pattern of heat flux deposition on the single poloidal hoop limiter is measured with an infrared camera. When the EML coils are powered, the surface temperature distribution on the limiter changes from a uniform pattern to a localized one. If the q value at the limiter is varied during an EML pulse, the localized pattern changes in time revealing a complex three dimensional path through the ergodic boundary of the heat flux.

Another striking feature is the appearance of luminous "stripes" in high density operation with the $m/n = 7/2$ mode. Tangential TV observations through an H_α filter reveal the presence of many stationary stripes in the boundary region. Data from Langmuir probes show a spatial modulation in the electron density outside the limiter radius, suggesting that density ripples cause this nonuniform excitation of the neutral hydrogen recycling flux from the limiter surface.

A drop of $\sim 20\%$ in the boundary temperature due to EML has also been observed. Such a drop is most evident at low density ($\bar{n}_e < 4 \times 10^{13}$ cm⁻³) and high helical field.

The conditions for the temperature drop and the magnitude of the drop are consistent with the theoretically estimated electron thermal conductivity in the ergodic magnetic structure. Further evidence of a drop in the edge temperature are obtained by spectroscopic measurements. Line emission profiles of low charged states such as CIII at CIV (radiating around 40 and 50 eV, respectively) broaden during EML, indicating a broadening of the low temperature region. Reduction of Titanium signals (TiXI and TiXXI) during EML also suggests a reduction of the temperature at the (TiC-coated) limiter. These observations clearly demonstrate the existence of a stable ergodic magnetic layer, in which the heat transport is enhanced and modified.

Particle Simulation of Divertor Plasma

T. Takizuka, K. Tani, and M. Azumi

Japan Atomic Energy Research Institute
Tokai, Naka, Ibaraki, Japan

Abstract: Characteristics of divertor plasma are studied by using a one-dimensional electrostatic particle simulation code with a binary collision model. Dependence of plasma parameters, such as temperature, flow speed, pre-sheath potential, etc., on the collisionality is investigated in detail. The pre-sheath potential is formed by the collisional relaxation of the velocity distribution as well as by the particle source.

1. Introduction

A poloidal divertor is considered to be the most reliable concept for a tokamak fusion reactor from the points of impurity and neutral particle control and heat flux density reduction. Characteristics of the scrape-off layer plasma in a divertor tokamak have been studied experimentally and theoretically. The fluid model has been usually applied for analyses of divertor plasmas. It is doubtful, however, whether the usual fluid equations carry the validity to describe the scrape-off layer plasma; the plasma is bounded by divertor plates, the flow speed is almost the sound speed, and the velocity distribution functions of electrons and ions are much distorted from the Maxwellian.

In order to study the divertor plasma consistently, we have developed a one-dimensional electrostatic particle simulation code with a binary collision model. In the next section, we explain about this code. Simulation runs are performed in the wide range of the ratio of collision frequency to bounce frequency of electron. Results of simulations are shown in section 3. Discussion on the fluid model is made in the last section.

2. Simulation model

In a scrape-off layer plasma bounded by divertor plates, the self-consistent electrostatic field, i.e., sheath and pre-sheath field, plays the most important role. Distribution functions of electrons and ions are much distorted from the Maxwellian. Therefore, the electrostatic particle model is suitable to study divertor plasmas. Two-dimensional simulation was

performed by Takizuka et al. [1], where the cross field diffusion of particles is simulated by using a Monte Carlo technique. Stationary state is realized by the balance between the particle flux from the main plasma to the scrape-off layer due to the diffusion and the flow into the divertor plate. The pre-sheath in the scrape-off layer is formed by the particle source near the central region and by the particle diffusion in the divertor region. Effects of collisions are neglected in this simulation, and only the cross field diffusion supplies electrons with large velocity parallel to the magnetic field, which can pass through the sheath potential barrier at the divertor plate. Coulomb collisions, however, play a very important role to supply electrons with large velocity, as well as the cross field diffusion.

We aim, in this paper, to study the importance of collisions in a divertor plasma, and we have developed a one-dimensional electrostatic particle simulation code with a binary collision model. Motions of particles with finite size of the order of Debye radius are followed in the x direction parallel to the magnetic field. The collisionless motion of each particle is described as

$$\frac{dv_{||}}{dt} = - \frac{e_j}{m_j} \frac{\partial \phi}{\partial x} , \quad \frac{dx}{dt} = v_{||} ,$$

where e_j and m_j are the charge and the mass of a particle of j species, respectively. The electrostatic potential ϕ is considered to be changed only with respect to the x direction and is determined by Poisson's equation,

$$- \frac{\partial^2 \phi}{\partial x^2} = \frac{1}{\epsilon_0} (e_i n_i - e n_e) ,$$

where ϵ_0 is the permittivity of vacuum, n_i the ion density, and n_e the electron density. The divertor plasma is bounded by divertor plates located at $x=L$ and $x=-L$. The electrostatic potential is symmetric, $\phi(-x)=\phi(x)$, and we calculate above equations in the region, $0 \leq x \leq L$. Boundary conditions for the potential are given by

$$\phi = 0 \quad \text{at} \quad x = L , \quad \partial \phi / \partial x = 0 \quad \text{at} \quad x = 0 .$$

We can treat the position, $x=0$, as a reflecting wall for particles because there exist a pair of particles; one at $x=x_0$ has a velocity $v_{||0}$ and the other at $x=-x_0$ has a velocity $-v_{||0}$. A particle is considered to be neutralized and absorbed at the plate, $x=L$. The reflection or desorption of neutral particles and secondary electrons at the plate are neglected in the present simulation, but these can be easily introduced in the particle simulation. Particles are supplied in the central region, $0 \leq x \leq L_s$, they are distributed

according to a Maxwellian distribution with temperature T_{j0} . Electrons with large $|v_{||}|$, which can pass through the sheath potential barrier, are supplied a little by the source but mainly by the collisional diffusion in the velocity space. In order to simulate the effects of Coulomb collisions, we apply a binary collision model proposed by Takizuka and Abe[2]. The major procedures of the model are that (1) a particle suffers binary collisions in the time interval Δt with an ion and an electron which are chosen randomly in a spacial cell, and that (2) the change in the relative velocity results from a Coulomb interaction. The absolute value and pitch-angle of the velocity $\vec{v} = (v_{||}, v_{\perp}^2)$ of a particle is changed by a binary collision, while both total momentum and total energy are conserved. The model describes a collision integral of the Landau form when the time interval is sufficiently small compared with the relaxation time. All the simulation procedures are as follows:

(i) Supply particles in the region $0 \leq x \leq L_S$; as $\langle v_{||}^2 \rangle = \langle v_{\perp}^2 \rangle / 2 = T_{j0} / m_j$ where $\langle \rangle$ denotes the average in the velocity space.

(ii) Calculate the density n_j and potential ϕ .

(iii) Push particles without collisions in a time interval Δt by using the leap-frog method; $v_{||}$ and x are changed.

(iv) Change velocities $\vec{v} = (v_{||}, v_{\perp}^2)$ by adding effects of collisions.

(v) Absorb particles at the plate, $x = L$.

Time is advanced by repeating these procedures until the system becomes stationary. The required time steps, K , to obtain the steady state solution is estimated as

$$K > 2L/C_S \Delta t \approx 2\sqrt{m_i/m_e} (\omega_p \Delta t)^{-1} (L/\lambda_D) ,$$

where C_S is the sound speed, ω_p the electron plasma frequency, and λ_D the Debye radius. The required particle number, N , for the reliable simulation results is about

$$N = (10 \sim 100) (\lambda_D/\Delta x) (L/\lambda_D) ,$$

where Δx is the mesh size (and/or particle size). Both values of K and N are proportional to L/λ_D . In the real situation, L/λ_D is about 10^5 and it is impossible to perform a simulation. Fortunately, characteristics of divertor plasma is almost unchanged by changing the value of L/λ_D except the sheath region near the divertor plate; the size of the sheath region is smaller than $10\lambda_D$. We can choose the value of L/λ_D as $10^2 \sim 10^3$ ($K = 10^4 \sim 10^5$ and $N = 10^3 \sim 10^4$), and we can obtain realistic solutions for divertor plasmas by the particle simulation.

3. Results

We perform simulation runs in the wide range of the ratio of collision frequency to bounce frequency of electrons,

$$\nu_{de0} / \nu_{be0} = 10^{-2} \sim 10 ,$$

where ν_{de0} is the frequency of 90° pitch-angle scattering by ions of an electron with energy of $m_e v_{te0}^2 / 2 = T_{e0} / 2$, and $\nu_{be0} = v_{te0} / L$ is the bounce frequency. The ratio, ν_{de0} / ω_p , is artificially increased. The value of ν_{de0} / ν_{be0} in a divertor plasma is approximately described by using plasma parameters (the density n in m^{-3} , electron temperature T_e in eV, and the length along a field line L in m) as

$$\nu_{de} / \nu_{be} \approx 10^{-16} \times n L / T_e^2 .$$

This value, in the JT-60 tokamak with $L \approx 100m$, is less than unity for the low density of the scrape-off layer plasma; $n \approx 10^{18} m^{-3}$ and $T_e \geq 100 eV$, and becomes larger than unity for the high density; $n \approx 10^{19} m^{-3}$ and $T_e \leq 100 eV$. The simulation parameters are $\omega_{p0} \Delta t = 0.25$ and $\Delta x / \lambda_{D0} = 0.5$, where the electron plasma frequency ω_{p0} is defined by the spacially averaged density and the Debye radius $\lambda_{D0} = v_{te0} / \omega_{p0}$. The system length, L , is $100 \lambda_{D0}$ and the length of the source region, L_s , is $0.3L$. Numbers of ions and electrons in the system are about 2500, respectively. The ion temperature of the source, T_{i0} , is usually equal to the source electron temperature, T_{e0} . The mass ratio, m_i / m_e , is chosen as 400 standardly. The dependence of simulation results on the temperature ratio and the mass ratio is also studied.

The steady state solution for the case of $\nu_{de0} / \nu_{be0} = 1$ is shown in Fig.1. Spacial profiles of (a) the electrostatic potential $e\phi / T_{e0}$, (b) particle number in a cell N_{cell} , (c) flow speed $V_{||} / v_{te0}$, and (d)(e)(f) mean random energies of ions and electrons are obtained by averaging these quantities in time ($2 < C_{st} / L < 4$). From Fig.1(a), we observe the sheath potential ϕ_s near the plate; $\phi_s \approx \phi(0.95L)$, and the pre-sheath potential $\Delta\phi$ due to collisions; $\Delta\phi = \phi(L_s) - \phi_s$. The dependence of these values on the collisionality are shown in Fig.2. It is clearly seen that the pre-sheath is formed by collisions as well as by the particle source in the region $0 \leq x \leq L_s$. The flow speed, $V_{||}$, is increased by this pre-sheath potential. Figure 3 shows the collision dependence of the flow energy, $m_i V_{||}^2$, at the divertor entrance $x = L_s$ (open circle) and before the sheath region $x = 0.95L$ (black circle). The broken line represents the flow energy normalized by the parallel random energy. We define the sound speed C_s as $m_i C_s^2 = m_e \langle \tilde{v}_{||}^2 \rangle_e + m_i \langle \tilde{v}_{||}^2 \rangle_i$. The flow speed is much greater than the sound speed before the sheath region, and the

Bohm condition for the sheath formation; $V_{||}/C_s \geq 1$, is satisfied.

The parallel random energy, $\langle \tilde{v}_{||}^2 \rangle$, and the perpendicular random energy, $\langle \tilde{v}_{\perp}^2 \rangle$, have different values each other. This is mainly caused by the different forms of the energy convection; the convection of parallel energy is $3m_j V_{||} \langle \tilde{v}_{||}^2 \rangle_j$, and that of perpendicular energy is $m_j V_{||} \langle \tilde{v}_{\perp}^2 \rangle_j$. The difference of electron energies becomes small as collisions is increased since almost electrons are trapped in the system by the sheath potential and the collisional relaxation is effective, while the relaxation of ion-energy difference is small even for $v_{di} \sim v_{bi}$. These relaxations are shown in Fig.4. Figure 5 shows the velocity distribution of electrons and ions in the region $0.5 \leq x/L \leq 0.6$ for the cases of (a) $v_{de0}/v_{be0} = 1$ and (b) $v_{de0}/v_{be0} = 10^{-2}$. The distribution function of electrons is almost a truncated Maxwellian rather than a shifted Maxwellian. The truncation velocity is about $v_{||} = -(2e\phi_s/m_e)^{1/2}$ for the electron distribution near the divertor plate. The parallel temperature and perpendicular temperature of electrons are much different for the rare-collisional case as is mentioned above. The ion distribution is much distorted from a Maxwellian even in the collisional plasma.

Next we study the dependencies of the solutions on the temperature ratio, T_{i0}/T_{e0} , and on the mass ratio, m_i/m_e . Figure 6 shows the flow energy before the sheath region (open circle) for the case that $v_{de0}/v_{be0} = 1/3$. The energy depends on T_{i0}/T_{e0} because the sound speed is changed by the value of T_{i0}/T_{e0} . The parallel random energies of electrons and ions are also shown in Fig.6 by black circles. The ion random energy, $m_i \langle \tilde{v}_{||}^2 \rangle_i$, has a finite value even for $T_{i0} = 0$, because ions supplied at various positions in the source region gain various energies from the potential. By replotting the flow energy with regard to the energy of the sound speed, $m_i C_s^2 = m_e \langle \tilde{v}_{||}^2 \rangle_e + m_i \langle \tilde{v}_{||}^2 \rangle_i$, we have the linear relation as shown by the broken line. The mass ratio dependences of the sheath potential and the pre-sheath potential are shown in Fig.7 for the case that $v_{de0}/v_{be0} = 3$. If we assume the electron distribution function as a truncated Maxwellian near the divertor plate, we obtain an equation for the sheath potential,

$$\frac{e\phi_s}{T_e} = \frac{1}{2} \ln \frac{m_i}{2\pi m_e} \frac{T_e}{m_i V_{||}^2} ,$$

where T_e is equal to $m_e \langle \tilde{v}_{||}^2 \rangle_e$. The large-velocity part of the distribution function, $v_{||} > (2e\phi_s/m_e)^{1/2}$, however, has a small value compared with a Maxwellian with the temperature T_e . Therefore, the value of the sheath potential is smaller than the predicted value and the mass ratio dependence is a little changed. We find from Fig.7 that the pre-sheath potential, $\Delta\phi$,

depends weakly on the mass ratio.

4. Summary and discussion

We have studied the divertor plasmas by a one-dimensional electrostatic particle code with a binary collision model. The collision dependence of characteristics of scrape-off layer plasmas is clarified. Coulomb collisions play a very important role to supply electrons with large velocities. The pre-sheath is formed by the collisional relaxation of velocity distribution as well as by the particle source.

Now we comment on the fluid equations for the analyses of divertor plasmas, on the basis of the results of the particle simulation. It is necessary for fluid equations that the parallel temperature, T_{\parallel} , and the perpendicular temperature, T_{\perp} , must be treated separately. The sound speed defined by the parallel temperature, $C_S = [(T_{\parallel e} + T_{\parallel i}) / m_i]^{1/2}$, is found not to be a monotonically decreasing function, and the Mach number, $M = V_{\parallel} / C_S$, can exceed unity as is shown in Fig.8(a) for $v_{de0} / v_{be0} = 1$. The point of $M = 1$ is the local maximum point of C_S in the source-less region;

$$C_S (1 - M^2) (dM/dx) = M (1 + M^2) (dC_S/dx) .$$

The energy flow consists of $V_{\parallel} (3T_{\parallel} + 2T_{\perp})_j$, $m_j \langle \tilde{v}_{\parallel} \tilde{v}^2 \rangle_j$, and $m_i V_{\parallel}^3$, which are shown in Fig.8(b) for $v_{de0} / v_{be0} = 1$. The energy flow of $\langle \tilde{v}_{\parallel} \tilde{v}^2 \rangle$ is usually replaced by the parallel conduction as

$$m \langle \tilde{v}_{\parallel} \tilde{v}^2 \rangle \sim - (v_t^2 / \nu_{coll}) (dT/dx)$$

This relation is derived from the equation of the third moment, by considering the above two terms are dominant in the equation. Another terms in the third moment equation is important, however, for the analyses of the scrape-off layer plasmas. Fluid equations from zeroth to third may be necessary, while the boundary conditions are not found at present.

Acknowledgment: The authors would like to thank Mr. M. Watanabe for his computational support.

References

- [1] T. Takizuka et al., in Plasma Physics and Controlled Nuclear Fusion Research 1980 (Proc. 8th Int. Conf. Brussels, 1980) Vol.1, IAEA, Vienna (1981) 679.
- [2] T. Takizuka and H. Abe, J. Computational Phys. 25 (1977) 205.

Figure captions

- Fig.1 Spacial profiles of (a) electrostatic potential ϕ , (b) particle number in a cell N_{cell} , (c) flow speed V_{\parallel} , (d) mean random energies $m_j \langle v_j^2 \rangle$ of ions (thick line) and electrons (thin line), (e) mean perpendicular random energies $m_j \langle v_{\perp j}^2 \rangle$, and (f) mean parallel random energies $m_j \langle \tilde{v}_{\parallel j}^2 \rangle$ in a scrape-off layer plasma. The electron collision frequency $\nu_{\text{de}0}$ is equal to the electron bounce frequency $\nu_{\text{be}0} = L/v_{\text{te}0}$. The source region is $0 \leq x/L \leq 0.3$, and the source temperature of ions T_{i0} is equal to that of electrons $T_{e0} = m_e v_{\text{te}0}^2$. The mass ratio m_i/m_e is 400.
- Fig.2 Collision dependence of potential for $T_{i0}/T_{e0} = 1$ and $m_i/m_e = 400$. The sheath potential ϕ_s and the pre-sheath potential due to collisions $\Delta\phi$ are normalized by the parallel random energy of electrons $m_e \langle \tilde{v}_{\parallel}^2 \rangle$ (broken line).
- Fig.3 Collision dependence of flow energy for $T_{i0}/T_{e0} = 1$ and $m_i/m_e = 400$. The flow is accelerated by the pre-sheath potential from the divertor entrance $x/L = 0.3$ (open circle) to the front of the plate $x/L = 0.95$ (black circle). The energy is normalized by the energy of sound speed $m_e \langle \tilde{v}_{\parallel}^2 \rangle_e + m_i \langle \tilde{v}_{\parallel}^2 \rangle_i$ (broken line).
- Fig.4 Collision dependence of mean random energies of (a) electrons and (b) ions for $T_{i0}/T_{e0} = 1$ and $m_i/m_e = 400$. Open circles (parallel random energy) and open triangles (perpendicular random energy) represent values at the divertor entrance $x/L = 0.3$, and black circles and black triangles represent values before the plate $x/L = 0.95$.
- Fig.5 Velocity distribution of electrons and ions for the cases of (a) $\nu_{\text{de}0}/\nu_{\text{be}0} = 1$ and (b) $\nu_{\text{de}0}/\nu_{\text{be}0} = 10^{-2}$.
- Fig.6 Dependence of flow energy on temperature ratio for $\nu_{\text{de}0}/\nu_{\text{be}0} = 1/3$. The flow energy is proportional to the energy of sound speed $m_e \langle \tilde{v}_{\parallel}^2 \rangle_e + m_i \langle \tilde{v}_{\parallel}^2 \rangle_i$ as seen from the broken line.
- Fig.7 Dependence of potential on mass ratio for $\nu_{\text{de}0}/\nu_{\text{be}0} = 3$. The sheath potential ϕ_s is proportional to $\ln(m_i/m_e)$.
- Fig.8 Spacial profiles of (a) flow speed and (b) energy flow for $\nu_{\text{de}0}/\nu_{\text{be}0} = 1$, $T_{i0}/T_{e0} = 1$, and $m_i/m_e = 400$.

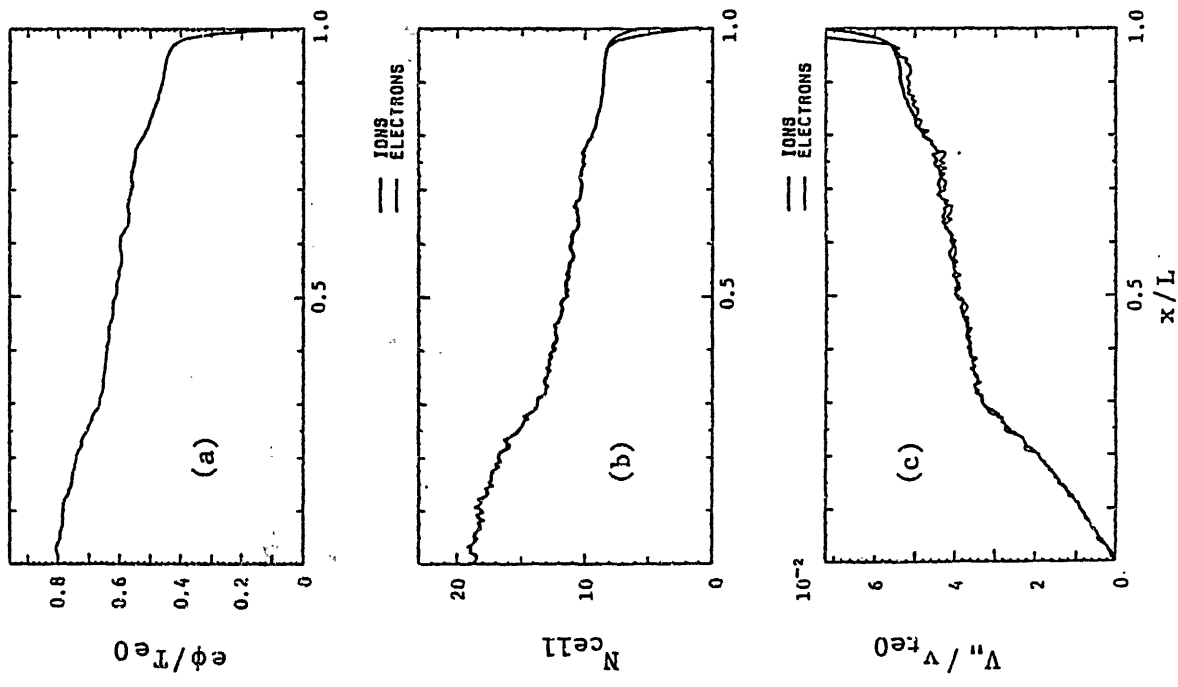
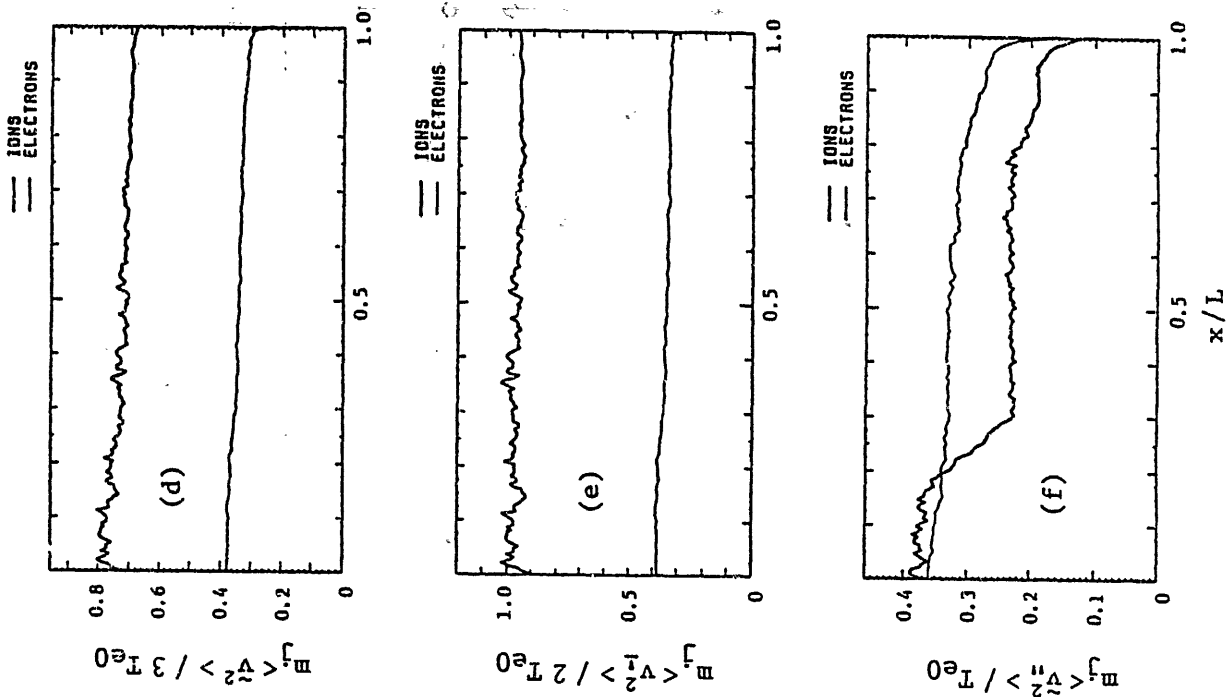


Fig. 1

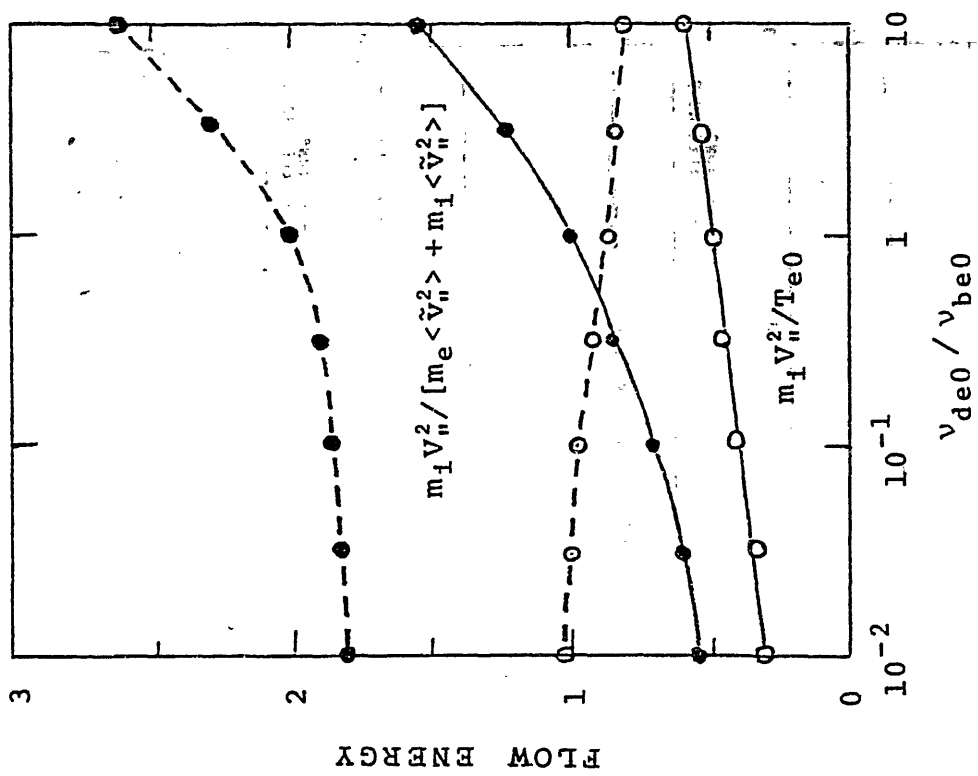


Fig.3

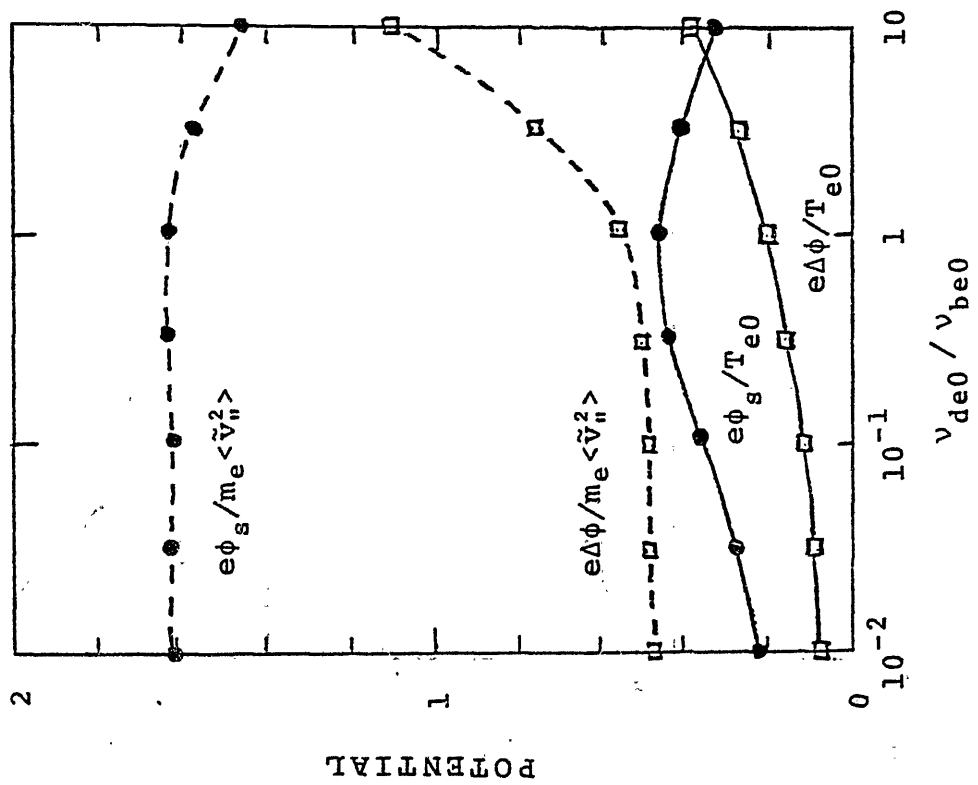


Fig.2

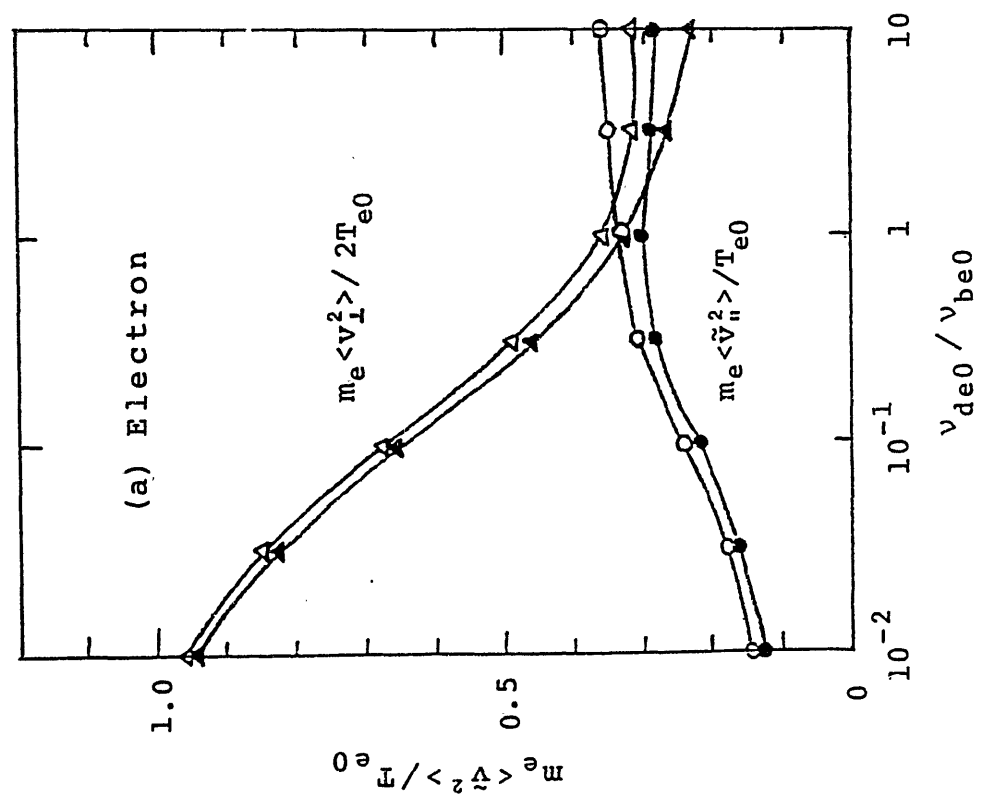
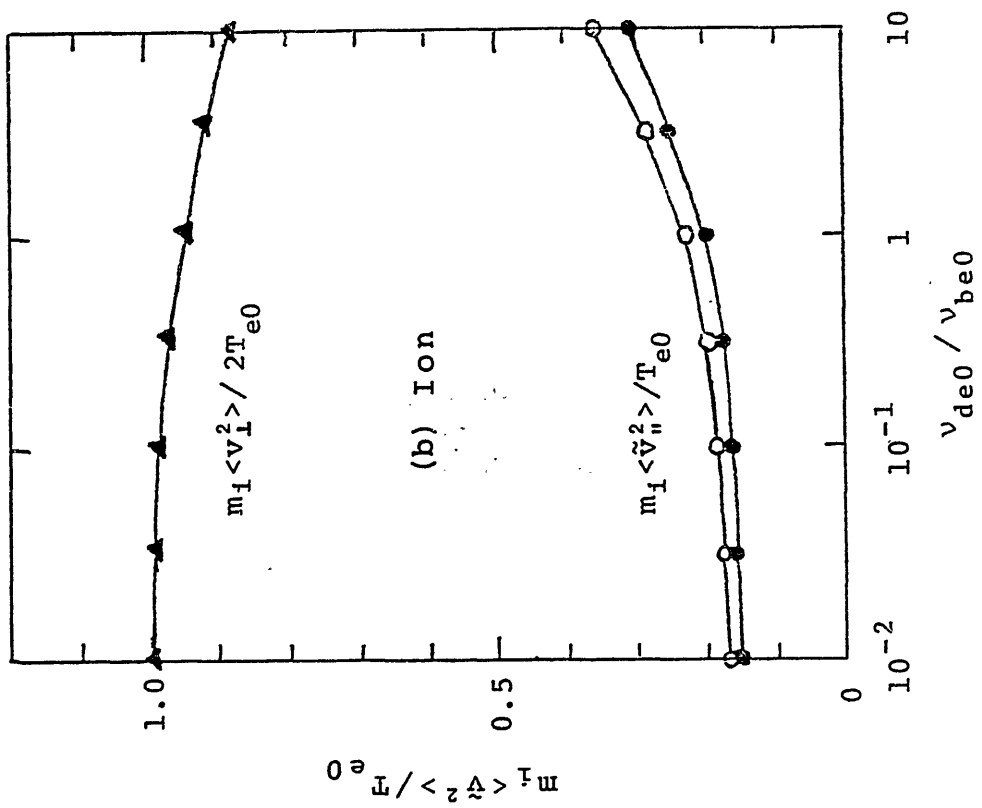


FIG.4

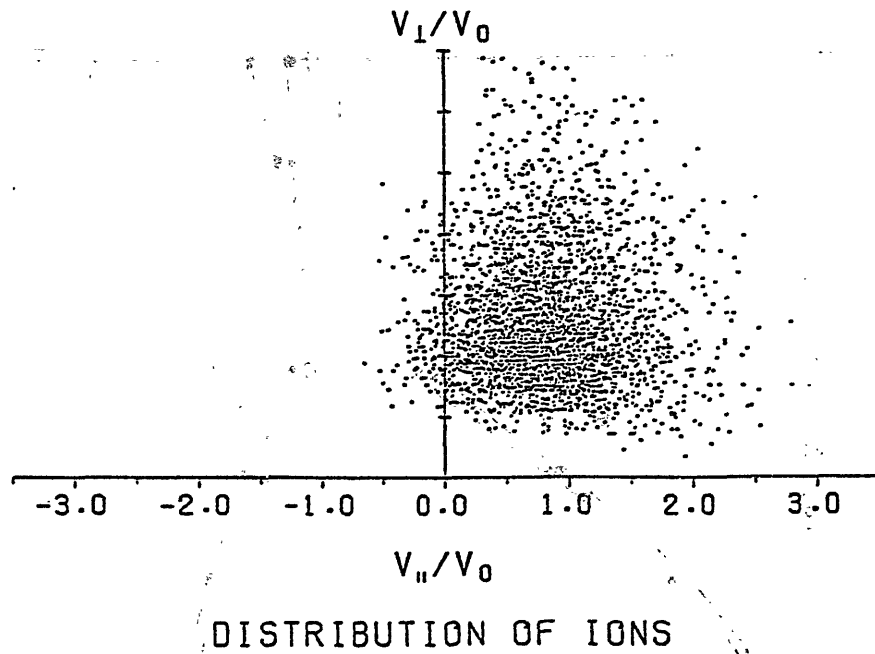
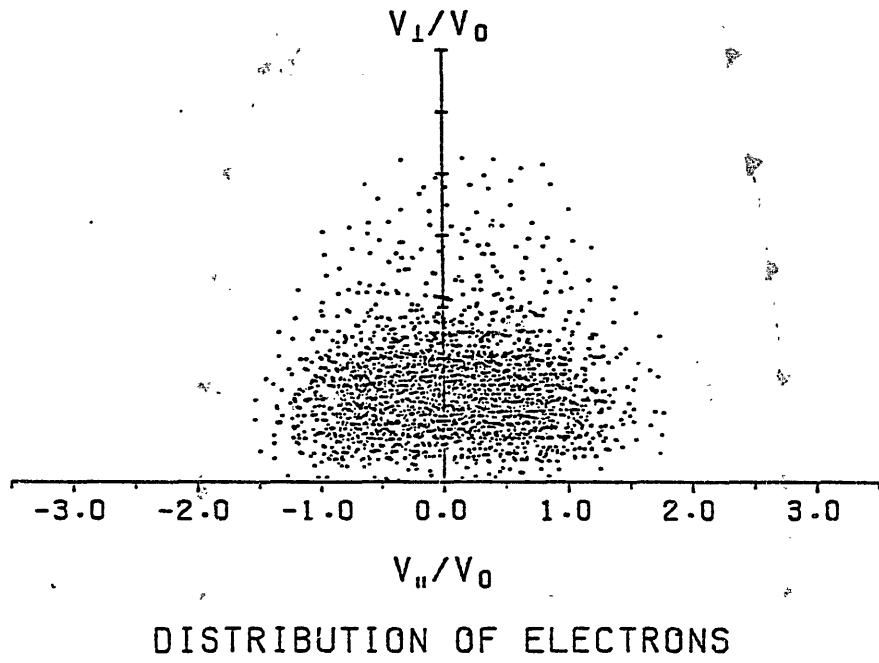


Fig.5(a)

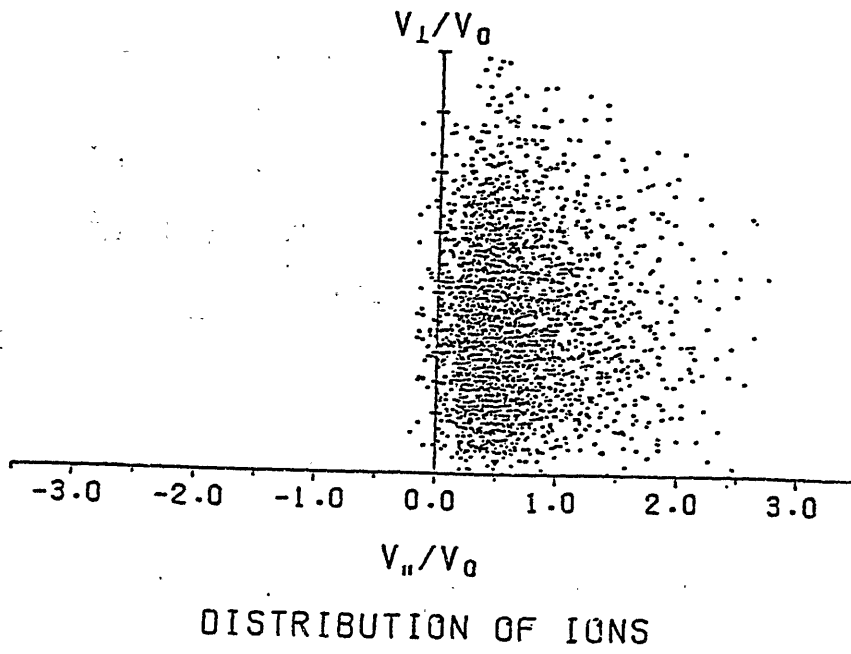
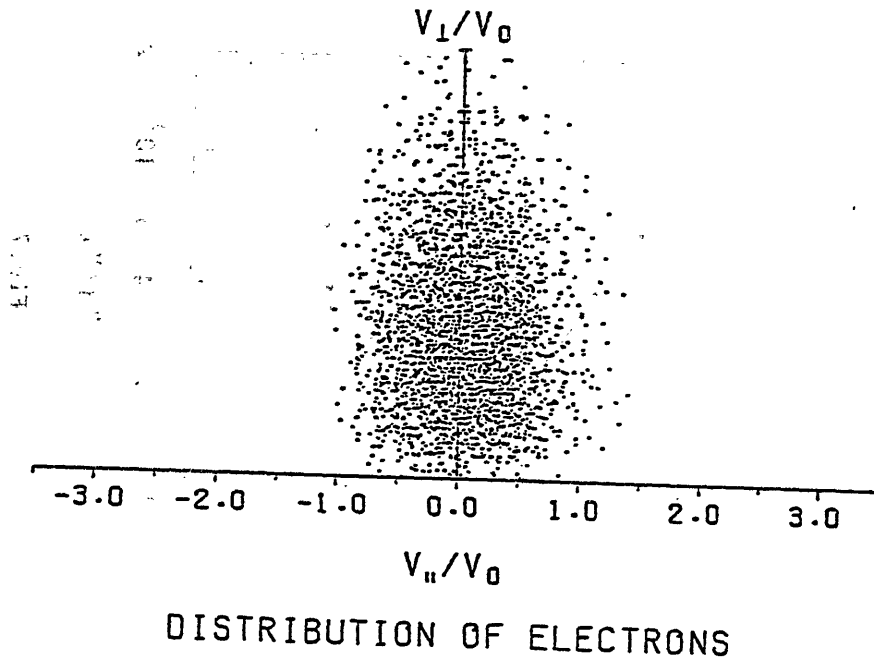


Fig. 5(b)

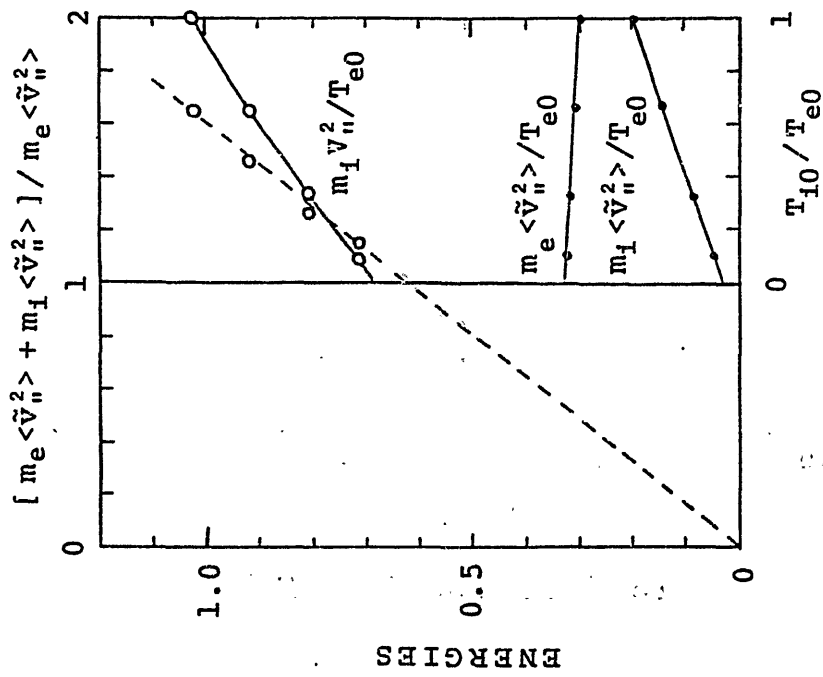


Fig.6

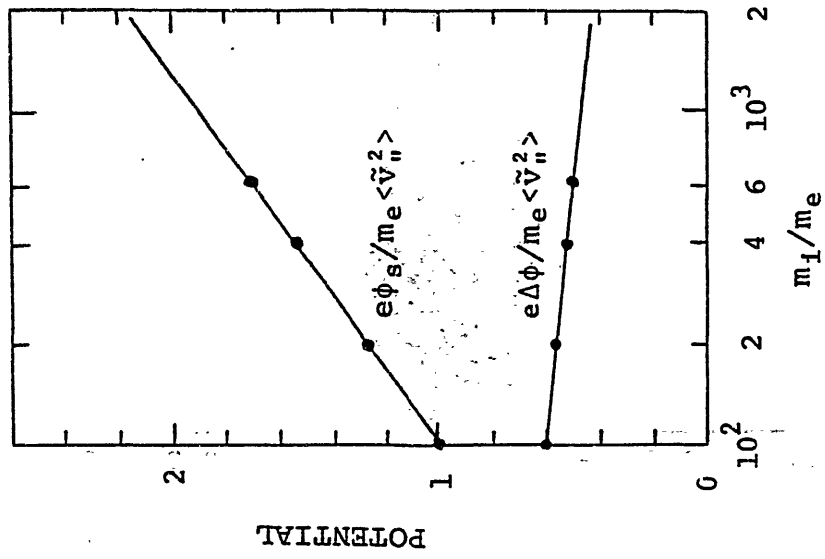


Fig.7

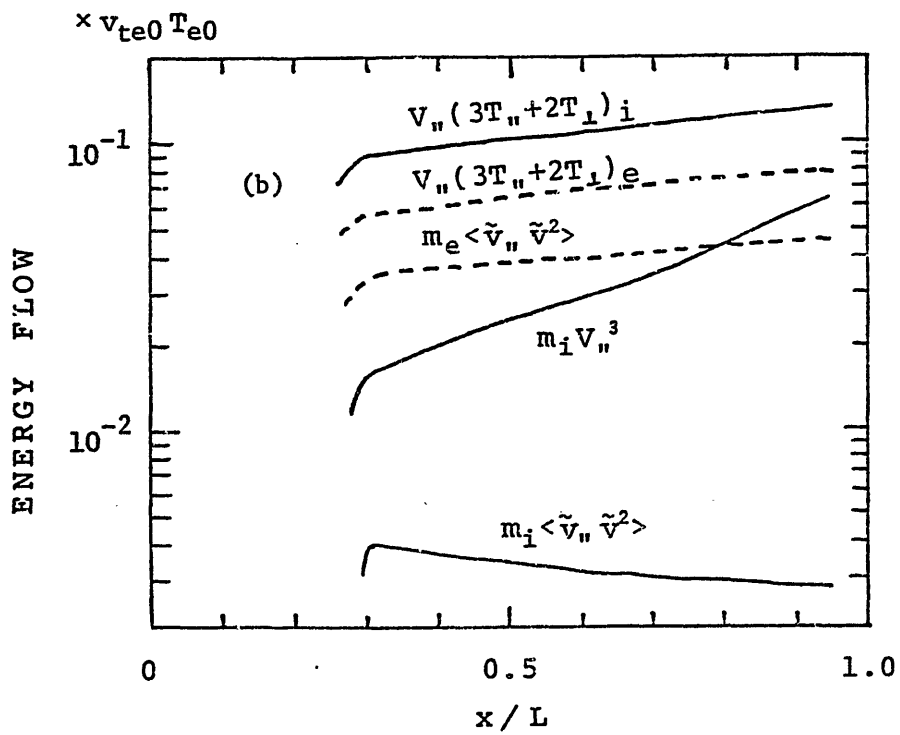
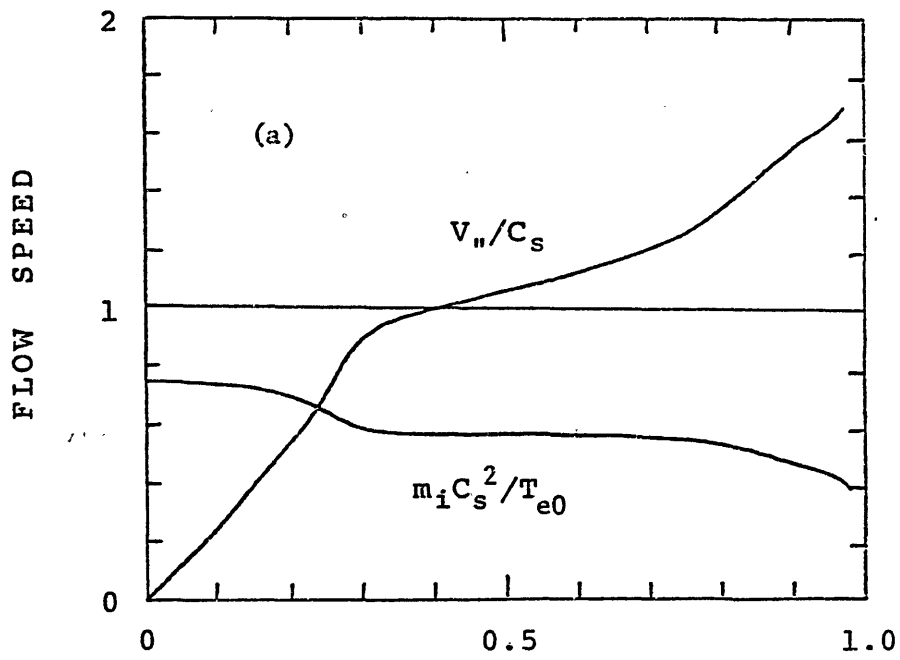


Fig.8

Modeling of Neutral Transport
(1)

at the
Plasma Edge *

D. Heifetz

Plasma Physics Laboratory, Princeton University

Princeton, New Jersey 08544

FROM REELED

Outline

- I. Neutral effects at the plasma edge and the ideal numerical model
- II. The DEGAS code
- III. Application 1: Neutral transport in the PDX divertor
- IV. Application 2: Performance of the ALT-II pump limiter
- V. Future development of DEGAS

* This work was supported by U.S. DOE Contract No. DE-AC02-76-CH03073.

I. Neutral Effects at the Plasma Edge and the Ideal Numerical Model

Transport of mass, momentum, and energy by neutral particles is an important effect at the edge of the plasma in a tokamak, where plasma neutralization at limiters or in divertors occurs. Phenomena affected by this transport include the overall power balance of the discharge, the pumping performance of pump and getter systems, the particle and energy fluxes onto the device walls, the erosion of the device walls due to impact sputtering, and the overall plasma confinement quality. Similar effects occur in the functioning of other magnetic confinement systems such as mirror machines. Knowledge of the neutral population is also important in the design and analysis of experiment diagnostics such as neutral particle emission analysers, H_{α} emission detectors, and pressure gauges.

The ideal, complete neutral transport model should include:

- (1) All important neutral-plasma reactions for all hydrogenic atomic and molecular species, including excitation/radiation effects, over a temperature range of from 1 to a few 10^4 eV,
- (2) The transport of light neutral impurities such as He^0 , Ne^0 , and Ar^0 ,
- (3) Neutral-neutral elastic scattering, which becomes important when the ambient neutral density is above 10^{14} cm^{-3} ,
- (4) Realistic wall reflection and impact sputtering models for incident energies from 1 to 10^4 eV,
- (5) Realistic models for the desorption of particles from walls, including wall saturation effects, and
- (6) An easily modified, three-dimensional, description of device

geometries.

The numerical solution should also be small and fast enough so that it can be included in plasma fluid or transport codes.

II. The DEGAS code

Modeling neutral particle transport in a plasma is very similar to the calculation of neutron transport [Gr] for which there is a large literature on both analytic and Monte Carlo methods of solutions. Analytic methods typically include physical models which are simply described, in geometries with symmetries [Au et al, Bur, Gil et al, Tam] while Monte Carlo solutions, though computationally much slower and perhaps less illuminating, can be used to treat physical processes with very detailed models in arbitrary geometries [P M, Cup et al, Ho, Hu P, R N, Seki et al]. Since our original intention was to study the effects of various physical processes on neutral transport, we ignored computational elegance and chose the Monte Carlo approach.

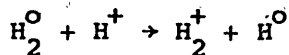
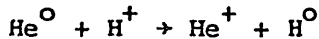
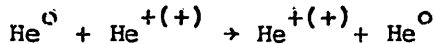
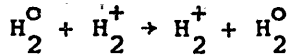
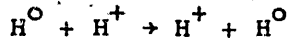
We describe here, then, our recent work in modeling neutral transport using the three-dimensional Monte Carlo code DEGAS. The DEGAS code at present includes the following parts of the ideal model:

(1) The set of neutral-plasma reactions listed in Table I for hydrogenic atoms and molecules. Neutral-ion reactions are computed as functions of ion temperature and neutral energy. Electron impact ionization of hydrogen includes the effects of multi-step ionization, hence is a function of both electron density and temperature. Reaction rates for these reactions are were taken from the data and formula in [F J, J, We]. Since these

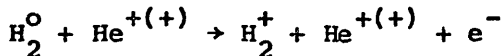
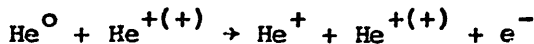
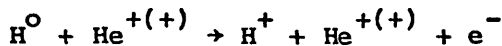
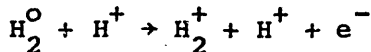
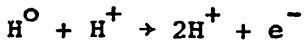
TABLE I

Neutral-Plasma reactions in DEGAS

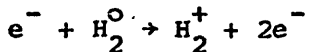
Charge-exchange:



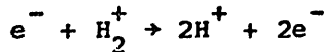
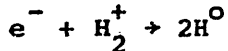
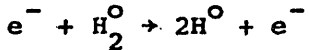
Ion-impact ionization:



Electron-impact ionization:



Electron dissociation:



references are now somewhat outdated, and even partially incorrect, we plan to include the results of a more recent survey of reactions [Jan et al] in the near future. This survey includes additional data on molecular vibrational excitation rates, and neutral-plasma elastic scattering processes.

(2) Transport of He^0 (cf. Table I). Inclusion of Ne^0 and Ar^0 is expected soon.

(3) No neutral-neutral elastic scattering processes. Including these would require a change in the program architecture, computing the neutral density iteratively, and we do not plan to do this in the near future.

(4) Reflection models using both experimental data and results of numerical simulation from: (a) the TRIM code for normal particle incidence and incident energy, E_{in} , greater than 100 eV [E V], (b) empirical fits for normal incidence and $E_{in} > 1$ keV from [Ta et al], (c) theoretical fits for $E_{in} < 100$ eV from [Sin et al, Bas], and (d) the MARLOWE code [Rob et al], for H, D, T, and He + Fe, for arbitrary incident angles and E_{in} from 50 to 1000 eV. Impact sputtering is computed as a function of target species, incident particle species, energy, and polar angle using the empirical fitting routine DSPUT [Sm et al],

(5) A simplified wall desorption model, where atoms and molecules which stick to the wall are assumed to desorb immediately as

molecules (hydrogen species), or atoms (all other species) at the wall temperature,

(6) Fully three-dimensional geometries (Fig. 1).

The numerical methods used in DEGAS have been described elsewhere in great detail [He et al 1, H P], and will not be discussed here. DEGAS has been successfully combined and run iteratively on a production basis with a number of plasma codes, including the 1-D fluid model of D. Post described elsewhere in this workshop, the SOLID 1-D, two fluid model [S L], the PLANET 2-D, two-fluid code [Pet et al 1], and the BALDUR 1-D radial transport code [Sil et al].

In the past year we have given emphasis to supporting the use of these codes to model existing experiments (Table II), and to using this modeling experience in the design of a number of proposed experiments (Table II). We describe next two of these modeling projects: neutral transport in the PDX divertor, and calculation of the pumping performance of the proposed ALT-II pump-limiter experiment.

III. Application 1: Neutral Transport in the PDX Divertor

Recent studies of the existence of H-mode discharges in PDX, ASDEX, and D-III [Wa et al, Ka et al, Oh et al] have raised questions about particle refueling through divertors. Two of the more important questions concern the degree of multiple recycling of particles in the divertor, that is, determining the divertor particle confinement time, and, the related question of the conductance of the plasma filled channels in the closed divertors.

TABLE II

Recent Modeling of Divertor Experiments

ASDEX - Computing divertor recycling in H-Mode discharges [Sch et al]; Ar⁰ transport through the plasma-plugged divertor throat (K-G. Rauh, IPP-Garching); and analysis of charge-exchange emission spectra (E. Wagner, IPP-Garching).

PDX - Computing overall neutral particle recycling [Dyl et al, He et al 2, Pe et al 2]

DITE - Computing recycling and the power balance in the bundle divertor [Fie et al].

D-III - Computing recycling in the various magnetic configurations [Pet et al 3] (S.K. Wong, GA).

Recent Modeling of Limiter Experiments

PDX - Analysis of pumping by Zr-Al getters [H C]; analysis of the scoop-limiter experiment [Bud et al].

PLT - Analysis of LENS (Low Energy Neutral Spectral analyzer) results (D. Ruzic, PPPL).

TFTR -- Computation of D and T wall inventories [Bas et al]; analysis of the Zr-Al getter system (D. Heifetz, PPPL).

ISX - Modeling of the pumping performance of the pump limiters [Ev et al].

Recent Experiment Design Work

ALT-I (TEXTOR) - Aiding in the design of diagnostics [Bol et al].

ALT-II (TEXTOR) - Prediction of the pumping performance of various proposed pump-limiter designs [Con et al].

ASDEX UPGRADE - Computation of global neutral transport [Wun et al].

TFCX/INTOR - Analysis of proposed divertor and limiter designs [Pet et al 4, Bol].

MARS - Modeling of neutral transport in the halo (W. Barr and W. Kumai, LNL).

Modeling of the H-mode has been done using fluid treatments of varying sophistication [M H, Pet et al 2, S L, Shi et al, Po et al, Sai et al, G P]. I will describe here calculations of neutral transport in the PDX divertor (Fig. 2), where the plasma was described from experimental data, and assumed to remain constant during the calculation. This approach was designed to focus on issues involving the neutral transport alone, such as atomic physics, wall reflection, and wall desorption physics.

We began by constructing a consistent picture of the gas pressure, H_α radiation, and line average density measured in the divertor dome, for a series of ohmically heated discharges with varying main chamber line average densities [Dyl et al]. In particular we hoped to explain the variation of dome pressure (Fig. 3a), which increased exponentially as the mid-plane line-averaged density, $\bar{n}_e(m)$, increased from 1 to $3 \times 10^{13} \text{ cm}^{-3}$, and then saturated for $\bar{n}_e(m)$ above $3 \times 10^{13} \text{ cm}^{-3}$.

The key unknown from the viewpoint of modeling the neutral transport was the dome electron temperature, T_e , because there existed in the data only one Langmuir probe measurement for T_e in the relevant parameter range. We estimated T_e as follows. In the electron density and temperature ranges expected in the divertor, the H_α light emission, Γ , varies approximately (Fig. 3b) as

$$\Gamma \approx K n_e n_o (T_e)^\alpha, \quad \alpha = 5.3 \text{ for } T_e < 5 \text{ eV, and } 1.0 \text{ for } 5 < T_e < 60 \text{ eV,}$$

where n_o is the density of atomic hydrogen and K is a constant. Assuming n_o is proportional to the neutral pressure (Fig. 3a), we can then determine the variation of dome T_e since we know that of the dome line-averaged density,

\bar{n}_e (d), and the dome H_α light emission.

The resulting plot for T_e , scaled at one point with the data from a Langmuir probe, is shown in Fig. 3c. Note that T_e falls below 10 eV for \bar{n}_e (m) above $3 \times 10^{13} \text{ cm}^{-3}$.

Using this data for \bar{n}_e (d) and T_e , neutral transport was computed. The calculated dome neutral pressures and H_α emission rates are shown in Figs. 3a and 3c. The calculated H_α emission rates agreed qualitatively with that measured, and the computed and measured neutral pressures agreed quantitatively when a flow velocity Mach number of 0.11 was used. (No attempt was made for a quantitative comparison of absolute H_α emission intensities.)

We thus felt that we had a self-consistent picture of the neutral-plasma behaviour in the divertor, as well as insight into low temperature plasma recycling behaviour. An indirect measurement of T_e comes from noting that OII (4415A) emission cuts off as T_e drops below 10 eV, and one experimental measurement did see a cutoff of OII emission at \bar{n}_e (m) $\approx 4 \times 10^{13} \text{ cm}^{-3}$. Now the cooling of T_e to under 10 eV reduces the ionization probability of atoms, making the plasma more transparent to the neutrals. This reduces the ability of the divertor to maintain neutral pressure, and explains the saturation of the pressure as shown in Fig. 3a. An extreme example of this may have occurred in the collapse of the pressure seen during high flow gas fueling in the dome, as the plasma loses its ability to ionize, and the divertor channel becomes completely transparent.

Encouraged by our model's achievements, we applied the same methodology to the three phases of PDX discharges exhibiting H-mode behavior: the ohmic (OH), the pre-transition (PT), and the H-mode phases (H) [He et al 2]. We now

had extensive data on the plasma parameters [O et al]. Using this information we computed two-dimensional distributions of neutral temperatures, densities, and pressures such as the one shown in Fig. 4.

The one variable we focused on was again the measured dome pressure (Table III), which rose monotonically during the discharge. Our initial calculations resulted in pressures 1.5 - 2 times those measured (Table III), and even worse, showed a peak pressure during the PT phase. We then questioned the assumption that all device walls were saturated, and did no net pumping during the discharge; that is, that all absorbed particles desorb immediately as molecules. We introduced a pumping fraction, γ , defined as that fraction of sticking atoms which do not desorb during the neutral profile. In particular, the higher the saturation of the wall, the smaller the value for γ .

Results when $\gamma = 0.1$ are listed in Table III. The calculated pressures decreased from the $\gamma=0$ cases, agreeing with the measured values during both the OH and PT phases. However they still peaked in the PT phase. Re-adjusting γ further, we achieved agreement when $\gamma = 0.09$ in the PT phase, and $\gamma = 0.04$ in the H phase, and convinced ourselves that γ should decrease during the discharge as the walls became more saturated. This wall pumping model resulted in a pumping rate by the walls roughly equal to the rate of dome fueling, 20 Torr-l/s, applied during a typical discharge. We also note, however, that we cannot explain the good agreement our modeling of the ohmic discharges achieved described above, where $\gamma=0$ was used.

Table IV gives the overall divertor-main discharge refueling balance. Particle plugging, the fraction of neutrals reionized in the divertor, increased from 0.60 to 0.73 from the OH to the PT phases, but then dropped to

Table III

PDX Dome Pressure During an H-Mode Discharge

(10^{-4} Torr)

| Phase | Measured | $\gamma=0.0$ | $\gamma=0.1$ |
|-------|----------|--------------|--------------|
| OH | 1.8 | 2.4 | 1.8 |
| PT | 2.3 | 4.9 | 2.2 |
| H | 2.9 | 4.3 | 2.1 |

γ is the fraction of non-reflected atoms assumed to be retained in the wall during the discharge. Agreement with measured pressures was obtained when $\gamma = 0.09$ in the PT phase, and $\gamma = 0.04$ in the H phase.

Table IV

Particle Recycling During a PDX H-Mode Discharge

| Phase | Fraction Re-ionized in Divertor | Fraction Absorbed by Walls | Fraction Returned to Main Discharge |
|-------|---------------------------------|----------------------------|-------------------------------------|
| OH | 0.60 | 0.22 | 0.18 |
| PT | 0.73 | 0.12 | 0.15 |
| H | 0.70 | 0.14 | 0.16 |

0.70 during the H phase. In all cases the fraction of particles returned to the main discharge was between 15-18 per-cent. These results are significant in that many scenarios of H-mode functioning are based on the change in the nature of particle refueling during the discharge, and it is not clear from our results how much of a change occurs. Perhaps the energy of the neutrals transmitted through the divertor throat also effects the recycling.

We finish by noting that recent two-dimensional measurements of H_{α} light in the main chamber and divertor dome [Grek et al] showed a peak in intensity at a point in the main chamber below the coil casing beneath the PDX neutralizer plates. Our results predicted that the peak occurred in front of the plates. Thus there are a number of pieces of the picture which presently do not fit together.

IV. Application 2: Performance of the ALT-II Pump Limiter

The pumping performance of the proposed ALT-II experiment on TEXTOR [Con et al] depends on the neutral pressure at the pump duct openings. This pressure is created as plasma strikes the neutralizer plates. We have made a self-consistent calculation of parallel plasma transport and neutral transport using the one-dimensional fluid model of D. Post, described in this workshop, coupled with DEGAS.

The proposed design, which features 12 neutralizer plates positioned above pump duct openings, is shown in Fig. 5 along with the model geometry. Neutral transport was calculated in a fully three-dimensional geometry, while the plasma was modeled by dividing the plasma into four strips at the four minor radii 51.75, 52.75, 53.75, and 54.75 cm. At a point far away from the neutralizer plate the plasma densities at these radii were 5.0, 3.6, 2.5, and

$1.6 \times 10^{12} \text{ cm}^{-3}$, and the plasma temperatures were 34, 30, 23, 16 eV.

Results for the electron densities and temperatures near the plate are shown in Fig. 6. The densities near the plate have risen by factors of 2-3 over the values far from the plate, and the temperatures have dropped by more than a factor of 2. Of the plate current 6.9% was pumped.

A quantity related to pumping is the enhancement of particle flux at the plate. Defining R as the ratio of particle flux at the plate to the flux 10 cm from the plate, we calculated that $R = 4.9, 4.3, 3.1,$ and 2.0 at the minor radii of 51.75, 52.75, 53.75, and 54.75 respectively. (These values were much higher than observed on the PDX scoop [Bud et al], for example, and the model has not been verified as yet with any other experiment.) If we do factor R into our pumping calculation, and assume that 30% of the total plasma efflux enters beneath the blade, the net result is that about 8.4% of the total plasma efflux would be removed.

It may be possible to raise R still further by puffing gas at a point beneath the limiter blade directly in front of the plate. To see the effect of such fueling, a source of 10 Torr- ℓ /s of 300^oK molecules was added to the model calculation. The resulting plasma densities and temperatures are shown in Fig. 6. The densities were more highly peaked at the plate than when puffing was absent. The temperature dropped further within the first 20 cm from the plate by a factor of more than 2 to under 7 eV across the entire plate. The value of R increased to 6.4 at the top of the plate. Thus the introduction of 10 Torr- ℓ /s of puffed gas transformed a plasma with relatively flat n and T profiles along field lines near the plate to a plasma with significant gradients in n_e and T_e over a relatively short distance.

The higher n_e , lower T_e plasma also seemed to enhance pumping of ions recycling at the plate. The fraction of the flux at the plate that was pumped increased to 9.2% from the 6.9% for the pure recycling case. This net increase might have been due to the lower T_e in the puffing case, because the reaction rate for electron impact ionization of H in the non-puffing case is 3.7 times higher than in the puffing case. Thus the neutral particle attenuation from the plate to the duct opening is less in the low T_e case.

V. Future Development of DEGAS

The physical models in DEGAS are continually being modified as experimental data are made available and new theoretical models are developed. A parallel effort is also being made to include anomalous phenomena in order to match results from tokamak experiments.

DEGAS at present is a big and slow computer code since, as we mentioned, it was written to test the effects of different physical processes on the neutral transport, with little attention being paid to speed optimization or code size. We also wrote the code so as to be able to treat a wide range of problems, and this approach added to its complexity. The program size is determined mainly by the lengths of its many storage arrays, and their sizes can be adjusted to the needs of a particular problem by using FORTRAN PARAMETER statements. Speeding up a Monte Carlo code by making use of the present generation of vector computers is typically done by writing the algorithm to follow batches of test flights at a time. At the present, however, this would require a great deal of re-writing of DEGAS, which is beyond our present resources.

Bibliography

- [Au et al] K. Audenaerde et al, J. Comp. Phys., 34 (1980), 268-284.
- [Bas] W. Baskes, Dynamic Calculation of Low Energy Hydrogen Reflection, presented at the Sixth Int. Conf. on Plasma Physics Interactions, Nagoya, Japan (May, 1984).
- [Bas et al] W. Baskes et al., Tritium Inventory and Permeation in TFTR, presented at the Sixth Int. Conf. on Plasma Physics Interactions, Nagoya, Japan (May, 1984).
- [Bol] C. Boley, Transport of Neutral Atoms and Molecules in TFCX, presented at the Sixth Int. Conf. on Plasma Physics Interactions, Nagoya, Japan (May, 1984).
- [Bol et al] C. Boley et al., Neutral Transport in the ALT-I Limiter, to appear, J. Nucl. Mats.
- [Bud et al] R. Budny et al., PDX Scoop Limiter Discharges with High Energy and Particle Confinement Time, presented the Sixth Int. Conf. on Plasma Physics Interactions, Nagoya, Japan (May, 1984).
- [Bur] K.H. Burrell, J. Comp. Phys., 27 (1978), 88-102.
- [Con et al] R. Conn et al., An Advanced Pump Limiter Experiment of Large Toroidal Extent-ALT-II, to appear, J. Nucl. Mats.
- [Cup et al] E. Cupini et al, NIMBUS - Monte Carlo Simulation of Neutral Particle Transport in Fusion Devices, Comm. of the European Communities, Directorate General XII - Fusion programme Report 324/9, Brussels (1983).
- [Dyl et al] H. F. Dylla et al., Gas Fueling Studies in the PDX Tokamak: II, PPPL Report No. 2057, to appear J. Nucl Mats.
- [E V] W. Eckstein and H. Verbeek, Data on Light Ion Reflection, Max-Planck Institute fur Plasmaphysik, Garching-bei-Munchen, Report IPP 9/32 (1979).
- [Ev et al] K. Evans et al., Monte Carlo Simulation of the ISX Pumped Limiter,

presented at the Sixth Int. Conf. on Plasma Physics Interactions, Nagoya, Japan (May, 1984).

[F J] R.L. Freeman and E.M. Jones, Atomic Collision Processes in Plasma Physics Experiments, Culham Laboratory, Abingdon, Report CLM-R137 (1974).

[Fie et al] S. Fielding et al., Recent Results from the DITE Bundle Divertor, presented at the Sixth Int. Conf. on Plasma Physics Interactions, Nagoya, Japan (May, 1984).

[G P] J. D. Galambos and Y-K.M. Peng, 1-D Flow Model for Divertor Plasma, to appear J. Nucl. Mats.

[Gil et al] J. Gilligan et al., Nucl. Fusion, 18 (1978), 63.

[Gr] E. Greenspan, Nucl. Fusion, 14 (1974), 771.

[Grek] B. Grek, Private communication.

[H C] D. Heifetz and J. Cecchi, Modeling of Tokamak Pumping Systems, Bull. Am. Phys. Soc. 27 (1982) 1144.

[H P] D. Heifetz and D. Post, Comp. Phys. Comm., 29 (1983) 287-299.

[He et al 1] D. Heifetz et al., J. Comp. Phys. 46, (1982) 309.

[He et al 2] D. Heifetz et al., Calculations of Neutral Transport in the PDX Divertor, to appear J. Nucl. Mats.

[Ho] J.T. Hogan, J. Nucl. Mats., 111-112 (1982) 413-419.

[Hu P] M.H. Hughes and D.E. Post, J. Comp. Phys., 28 (1978), 43-55.

[J] E.M. Jones, Atomic Collision Processes in Plasma Physics Experiments: II, Culham Laboratory, Abingdon, Report No. CLM-R175 (1977).

[Jan et al] R.K. Janev et al., Survey of Atomic Processes in Edge Plasmas, Princeton Plasma Physics Laboratory, Princeton, Report 2045 (1983).

[Ka et al] S. M. Kaye et al., Attainment of High Confinement in Neutral Beam Heated Divertor Discharges in the PDX Tokamak, Princeton Plasma Physics Lab., Princeton, Report 2056 (1983).

- [M H] J. G. Morgan and P. J. Harbour, Fus. Tech. 1980 (Pergamon Press, 1981), Vol. 2, p. 1187.
- [O et al] D. Owens et al., Probe Measurements of the PDX Divertor Plasma in Ohmic and Neutral Beam Heated Discharges, to appear J. Nucl. Mats.
- [Oh et al] N. Ohyaibu et al., Proceedings of the IEEE International Conference on Plasma Science, San Diego, CA (1983).
- [P M] C. Parsons and S. Medley, Plasma Phys., 16 (1974), 267.
- [Pet et al 1] M. Petravic et al., Phys. Rev. Letts. 48, 326-329 (1982).
- [Pet et al 2] M. Petravic et al., Recent Progress in Tokamak Edge Modeling, presented at the Sixth International Conference on Plasma physics Interactions, Nagoya, Japan (May 1983).
- [Pet et al 3] M. Petravic et al., A 2-D Model for the Performance of Poloidal Divertors and Pump Limiters, Proceedings Ninth Int. Conf. on Plasma Physics and Controlled Nuclear Fusion Research, Baltimore (1982).
- [Pet et al 4] M. Petravic et al., INTOR Divertor in a Realistic 2-D Geometry, presented at the Sixth International Conference on Plasma Physics Interactions, Nagoya, Japan (May 1983).
- [Po et al] D. Post et al., An Analytic One-Dimensional Divertor Model with Neutral Sources, to appear J. Nucl. Mats.
- [R N] D. Reiter and A. Nicolai, J. Nucl. Mats., 111-112 (1982), 434-439.
- [Rob et al] M. Robinson et al., Phys. Rev. B9, 5008 (1974).
- [S L] W. Schneider and K. Lackner, Proceedings of the International Conference on Plasma Physics, Goetborg, Sweden (1982).
- [Sai et al] S. Saito et al., Self-Consistent Numerical Analysis for Scrape-off Plasmas and Neutral Particles in a Divertor Chamber, to appear, J. Nucl. Mats.
- [Sch et al] W. Schneider et al., Simulation of ASDEX Divertor Action Using a Realistic Neutral Gas Model, Proceedings of the 1983 E.P.S. Meeting, Aachen

(1984).

[Seki et al] Y. Seki et al., Nucl. Fus., 20 (1980), 1213.

[Shi et al] M. Shimada et al., Nucl Fus. 22, 643 (1982).

[Sil et al] A. Silverman et al., PPPL Applied Physics Report No. 23 (July 1983).

[Sin et al] C. Singer et al., New Recycling Model for Light Ions and Atoms Below 70 eV, submitted to J. Vac. Sci. and Tech.

[Sm et al] D. Smith et al., A Physical Sputtering Code for Fusion Experiments, Proceedings of the Ninth Sym. of Eng. Problems of Fusion Research, Chicago (1981).

[Ta et al] T. Tabata et al., Data on the Backscattering Coefficients of light Ions from Solids, Institute of Plasma Physics, Nagoya University, Nagoya, Report No. IPP-J-AM-18 (1981).

[Tam] S. Tamor, J. Comp. Phys., 40 (1981), 104-119.

[Wa et al] F. Wagner et al., Phys. Rev. Lett. 49, 1408 (1982).

[We] J. Weisheit, J. Phys. B: Atom Molec. Phys. 8, 2556 (1975).

[Wun et al] R. Wunderlich et al., ASDEX Upgrade: A Poloidal Divertor Tokamak Adopted to Reactor Requirements, presented at the Sixth International Conference on Plasma Physics Interactions, Nagoya, Japan (May 1983).

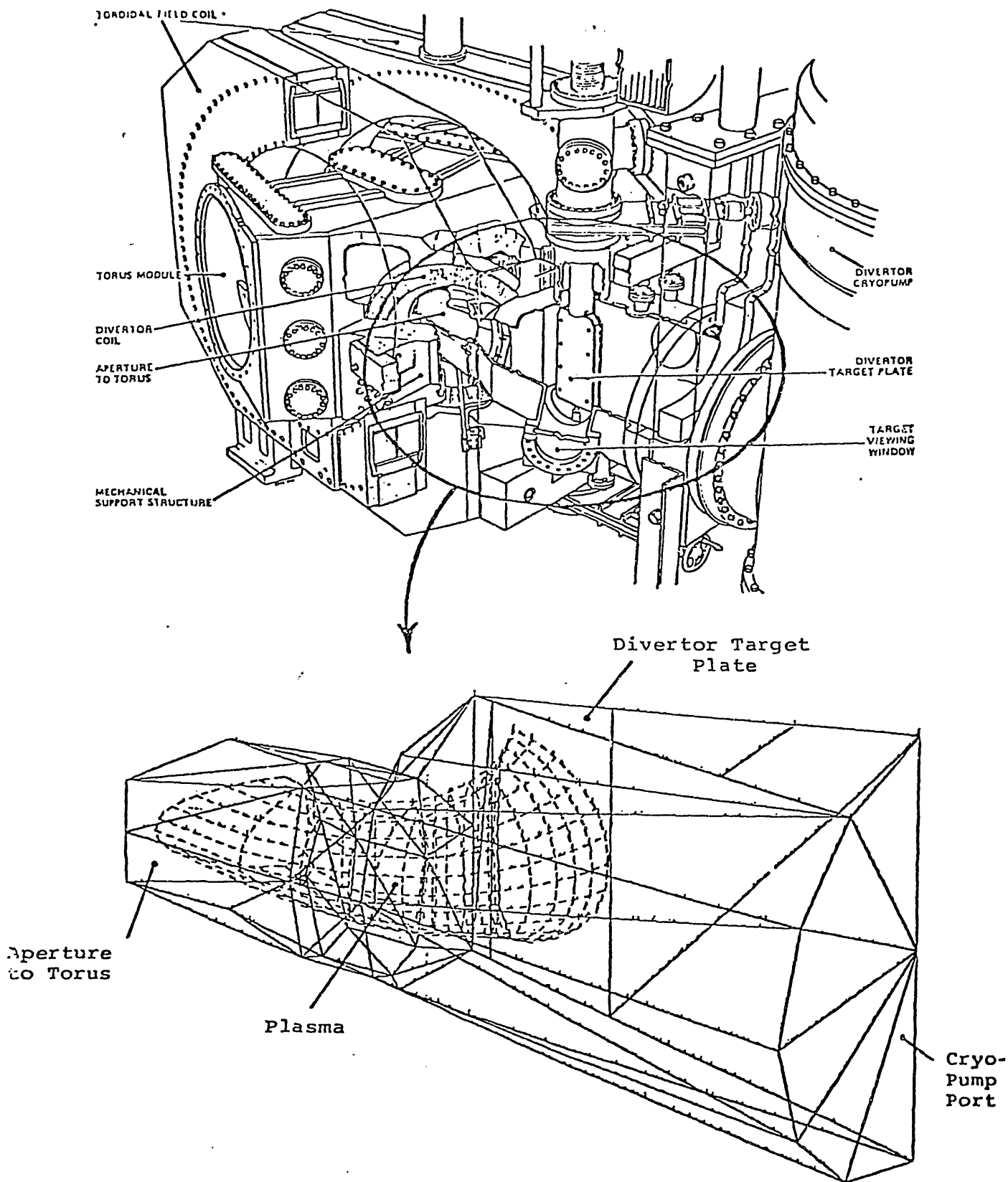


Fig. 1. Cut away drawing of the DITE bundle divertor Mk II (top), and the bundle divertor as modeled in three dimensions by DEGAS (bottom). By symmetry only half the device was included.

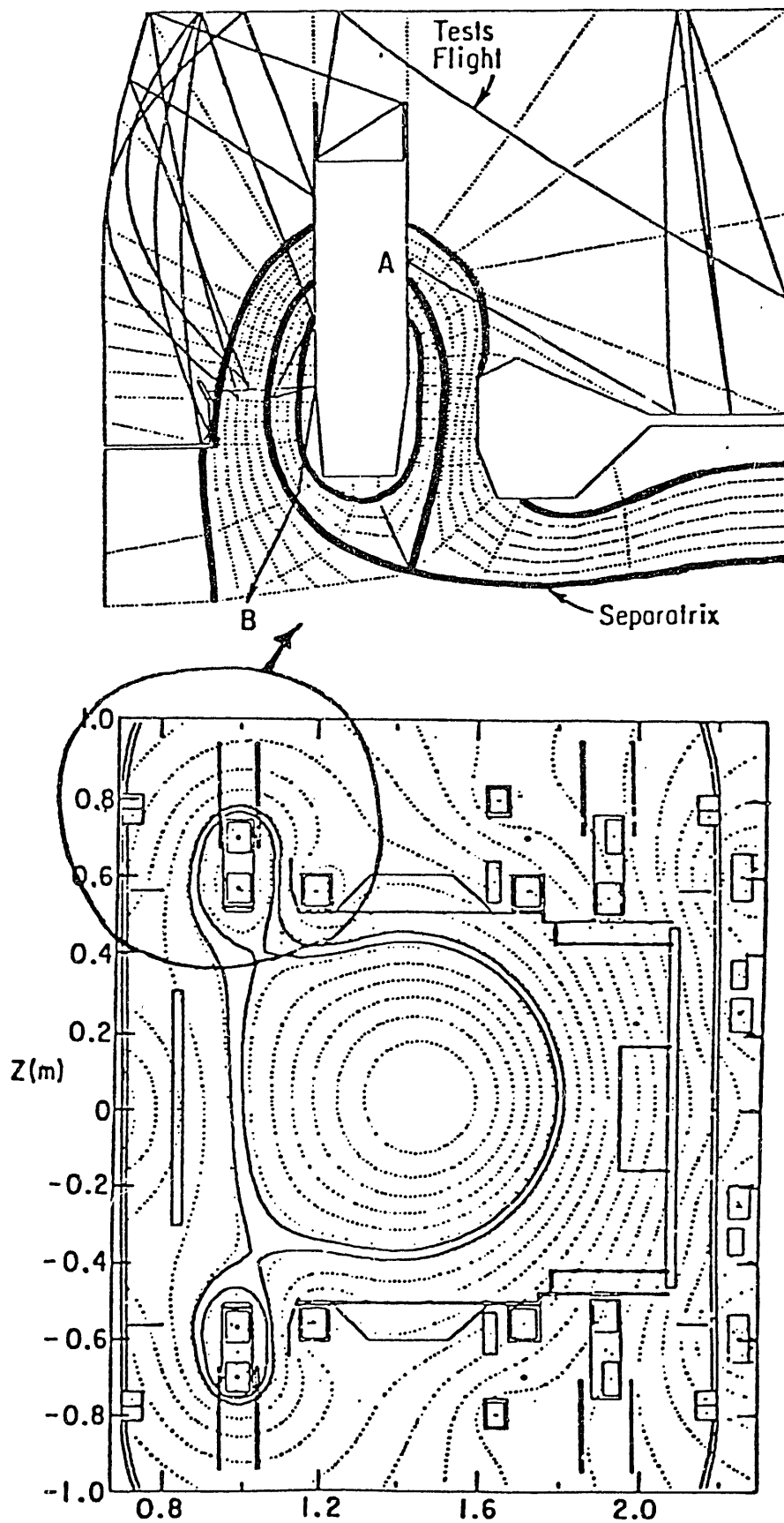


Fig. 2. Poloidal cross-section of the closed PDX divertor (top), and the divertor as modeled in DEGAS (bottom).

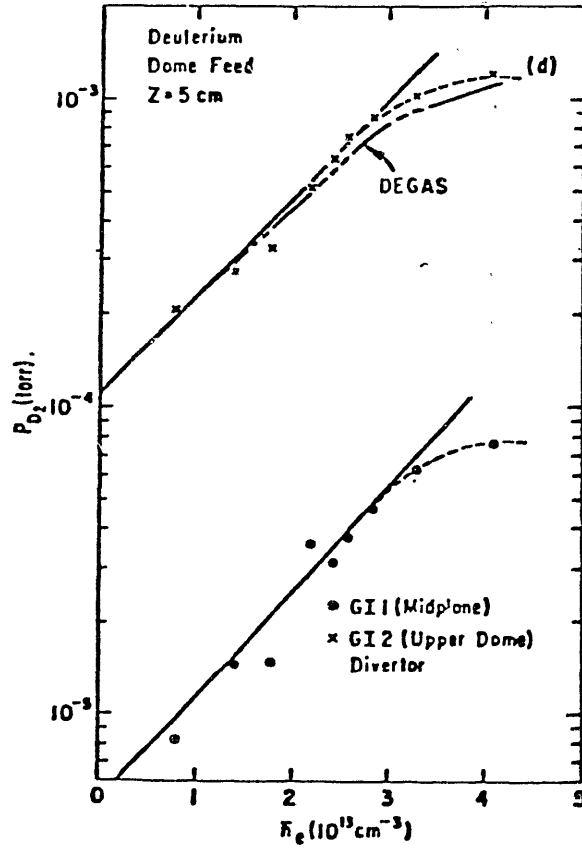


Fig. 3a. Measured dome pressure, P , as a function of the line-averaged plasma density, $\bar{n}_e(m)$, in the main chamber.

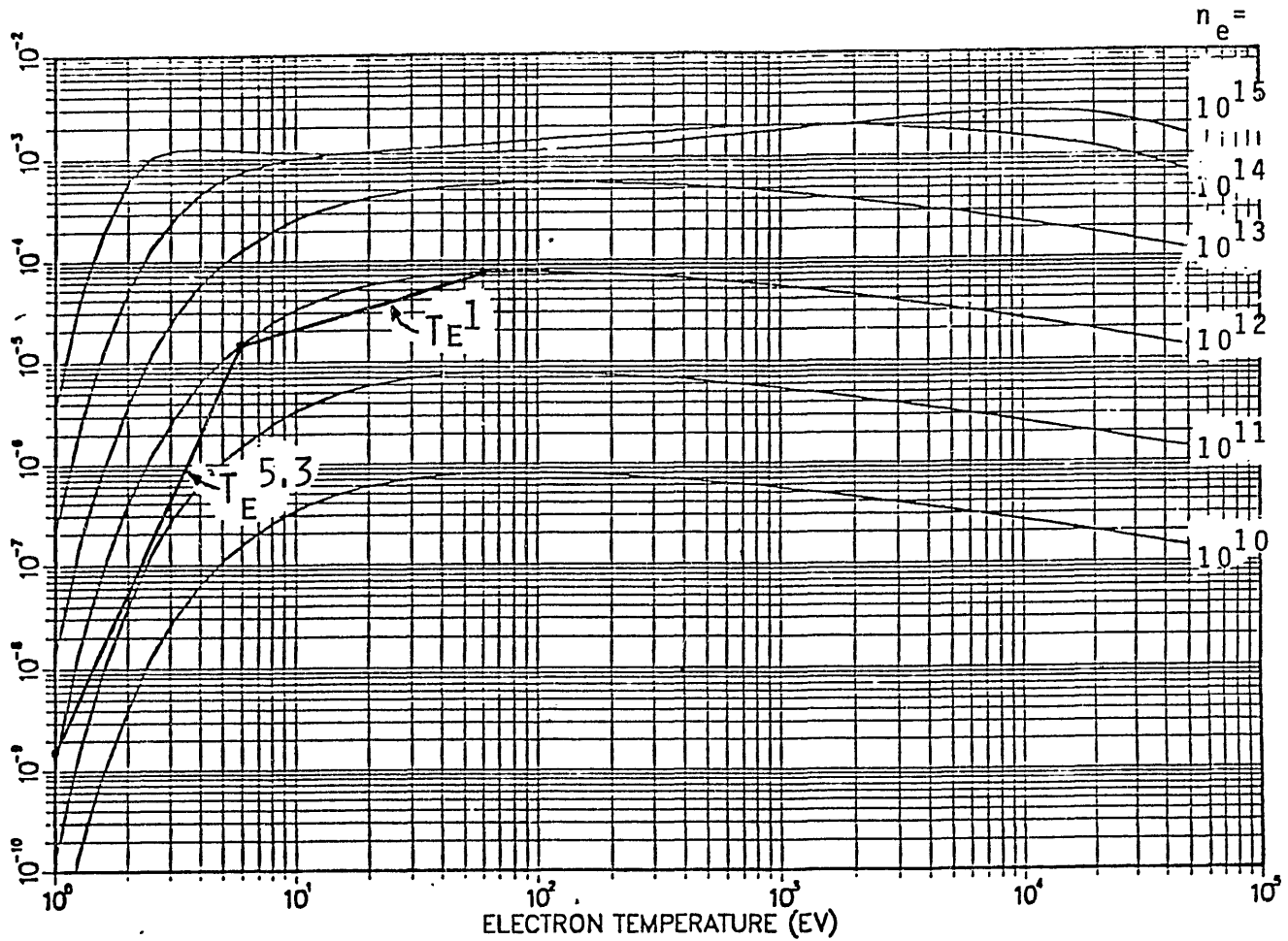


Fig. 3b. The fraction of D^0 excited to the $n=3$ level, as a function of electron temperature, T_e , and density, n_e . At $n_e = 10^{12} \text{ cm}^{-3}$, this fraction varies as $T_e^{5.3}$ for $1 < T_e < 5 \text{ eV}$, and $T_e^{1.0}$ for $5 < T_e < 60 \text{ eV}$.

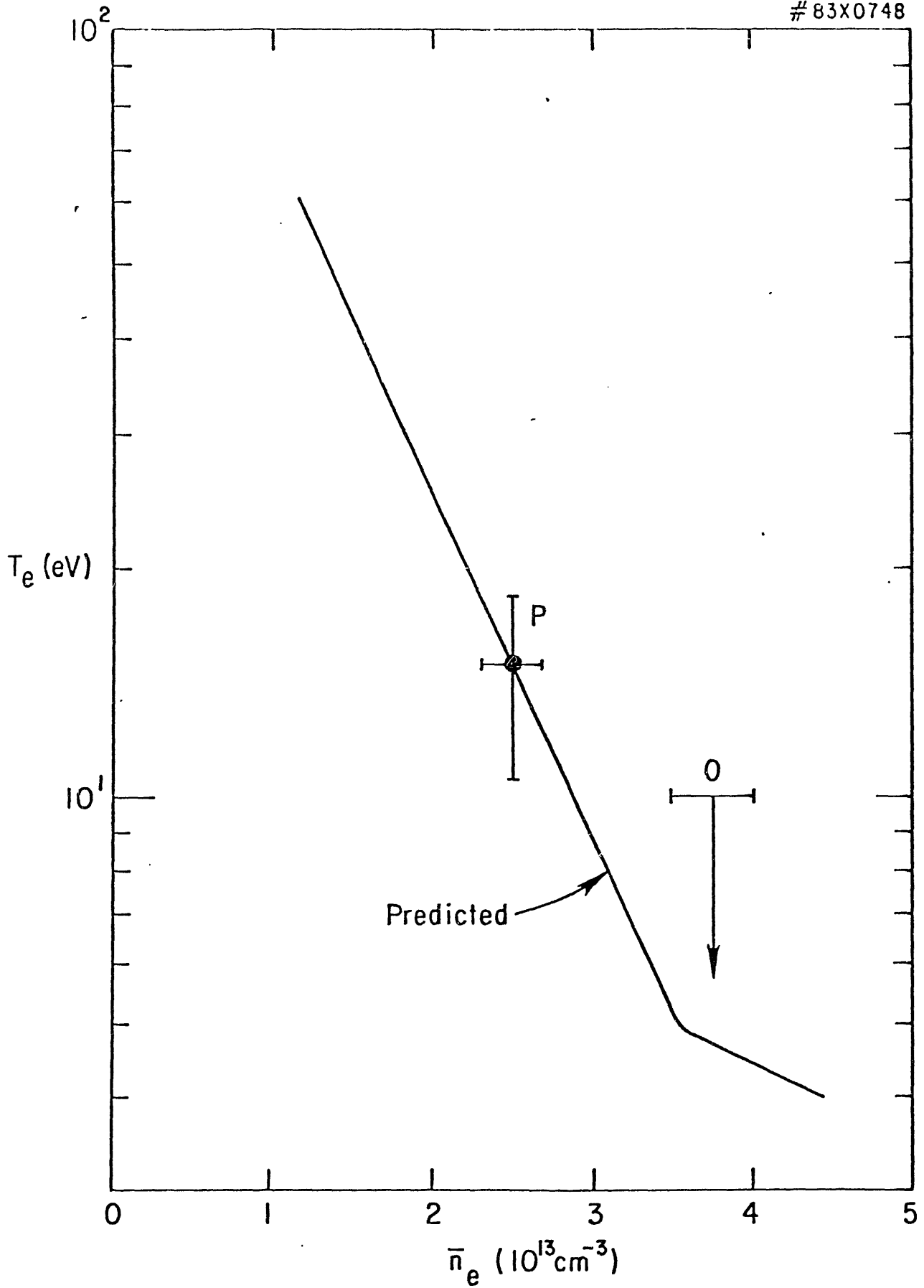


Fig. 3c. Divertor electron temperature, T_e , as a function of the line-averaged plasma density, \bar{n}_e (m), in the main chamber.

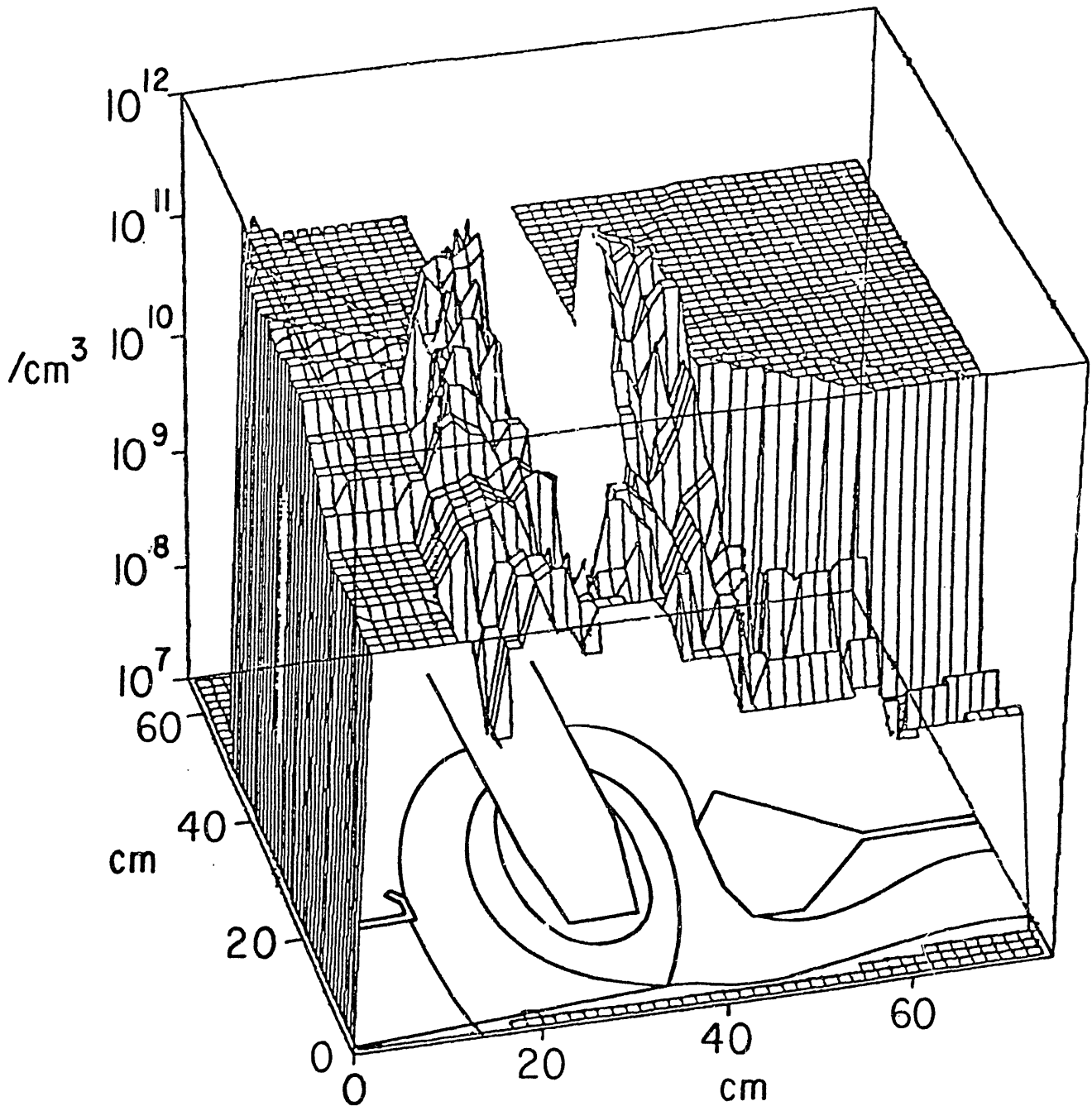


Fig. 4. Two-dimensional variation of the D^0 density pressure during the ohmic phase of a typical H-mode PDX discharge.

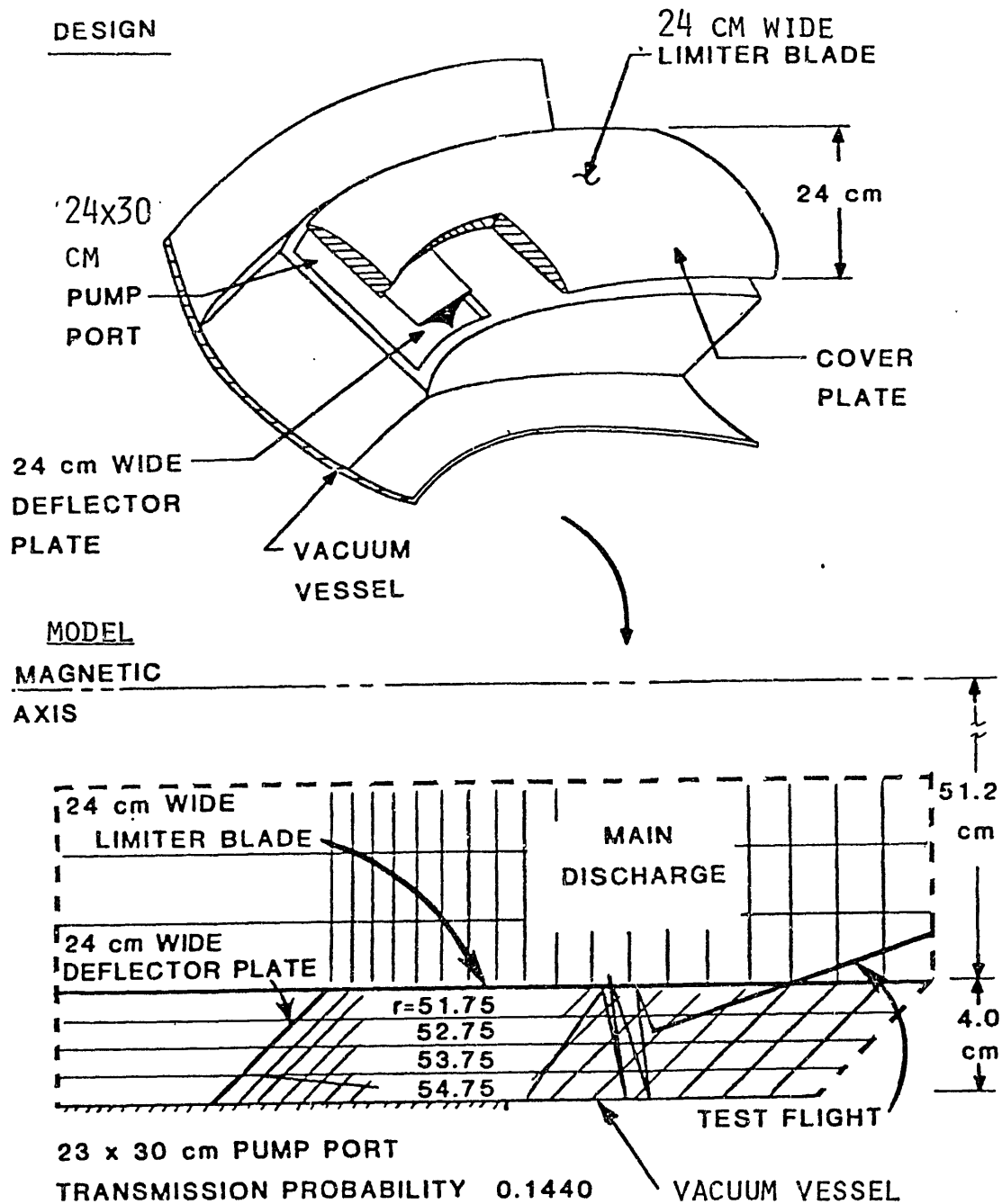


Fig. 5. A proposed ALT-II pump limiter design (top), where the limiter blade is axisymmetric, underneath which lie twelve deflector plate/pump duct combinations around the torus, and the ALT-II geometry as modeled (bottom). In the model the plasma beneath the limiter blade was divided into four strips, and a 1-D fluid treatment was applied independently to each strip.

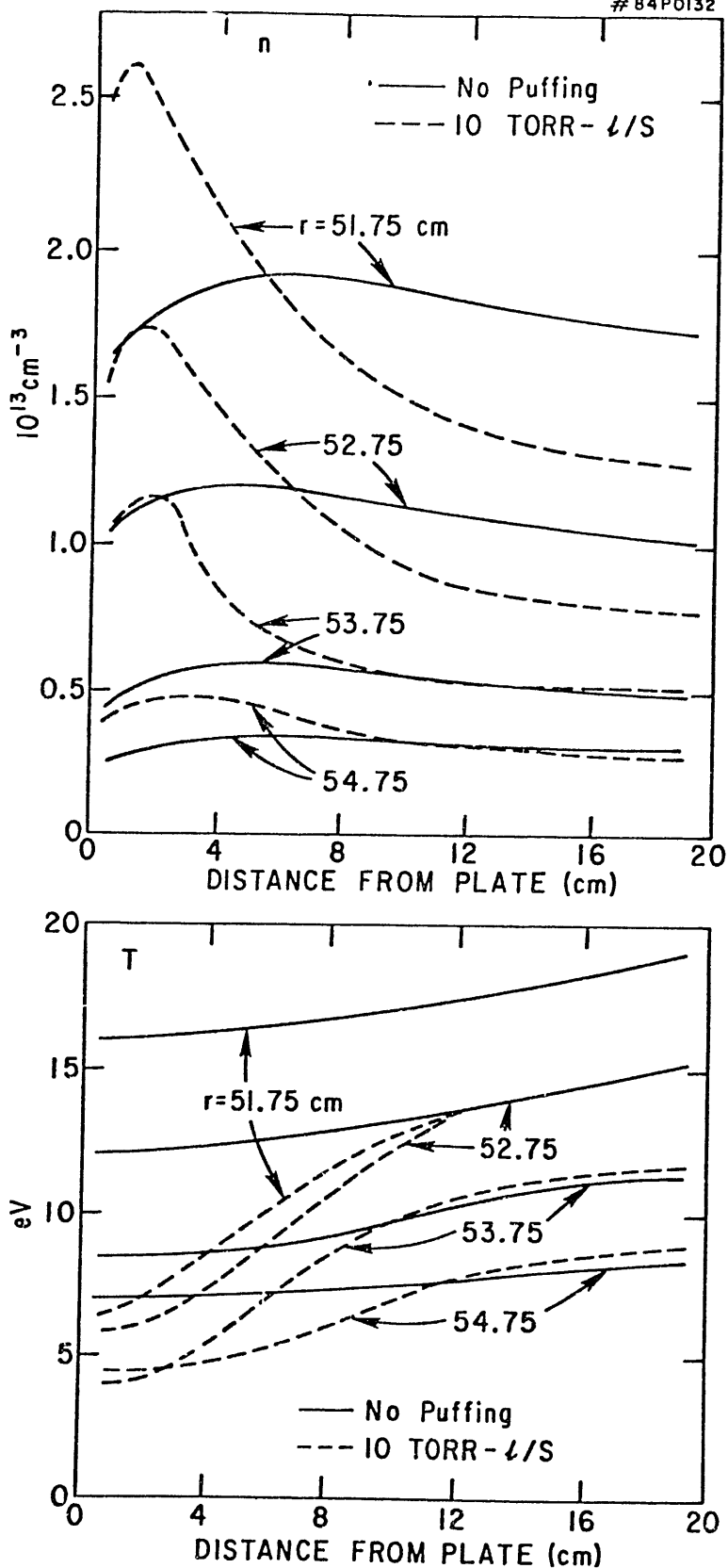


Fig. 6. ALT-II calculated plasma density (n) and temperature (T) as a function of minor radius (r) and the distance along a field line from the neutralizer plate.

Hydrogen Recycling at Wall Surfaces

K. Sone

Japan Atomic Energy Research Institute,
Tokai-mura, Naka-gun, Ibaraki-ken 319-11

In the previous paper [1], the effect of hydrogen trapping action of the wall on hydrogen recycling rate in a limiter configuration of the JT-60 tokamak has been discussed for three wall materials Inconel, Mo and TiC for the case of 20 MW neutral beam injection used. All wall and limiter surfaces of JT-60 will be coated with TiC of 20 μm in thickness, and so the discussion on TiC is particularly important. In this abstract is described the effect of chemical sputtering and titanium oxide formation, both of which are especially important in the case of TiC coating.

A modelling of hydrogen particle balance and recycling at the wall was described in detail in ref.[1]. Various particle fluxes are defined as shown in fig.1. The steady state recycling coefficient R at the wall alone is given by

$$R = 1 - \frac{1 - \alpha}{b(1-\alpha) + \alpha} \frac{\Gamma^{\text{NBI}}}{\Gamma^+}, \quad (1)$$

where α is the fraction of the total neutral influx which leave the plasma as charge exchange neutrals, b the fraction of the total influx of impinging ions to the wall. The total flux of ions leaving the plasma can be derived from the particle confinement characteristics as $\Gamma^+ = nV/\tau_p$, where n is the

average particle density in the plasma, V the plasma volume and τ_p the particle confinement time. Using eq.(1), we obtain a criterion for keeping a constant particle density n when high energy neutrals of flux Γ^{NBI} are injected during a discharge. When the recycling coefficient is less than R , the pumping rate by the wall is predominant. In such a case, we need to feed a suitable amount of hydrogen gas from outside the plasma to keep n value constant. On the contrary, when the recycling coefficient is greater than R , we need to pump an excess amount of hydrogen gas.

To treat the hydrogen recycling quantitatively, it is assumed here that the following three phenomena, backscattering, diffusion from the bulk and saturation overflow, are responsible for the re-emission of the particles incident onto the wall. A one-dimensional diffusion equation for the particles penetrating into the bulk is given as

$$\frac{\partial c(x,t)}{\partial t} = D \frac{\partial^2 c}{\partial x^2} + G(x) , \quad (2)$$

where D is the diffusion coefficient of hydrogen in the wall, $c(x,t)$ the concentration of hydrogen atoms at depth x and time t , and $G(x)$ the source term of hydrogen atoms at depth x . The source term $G(x)$ for random incidence is given by

$$G(x) = \int_0^{\pi/2} d\theta \int_0^{\infty} dE \sin 2\theta \cdot f(E) \cdot \rho_o(x,E,\theta) , \quad (3)$$

$$\rho_o(x,E,\theta) = \frac{\sqrt{2}}{\sqrt{\pi}} \frac{J_o [1-B(E,\theta)]}{\Delta R_p [1+\text{erf}(\epsilon_o)]} \exp \left[-\frac{(x-R_p \cos\theta)^2}{2\Delta R_p^2} \right] , \quad (4)$$

where $\epsilon_0 = R_p \cos\theta / \sqrt{2\Delta R_p}$, θ is the angle of incidence with respect to the surface normal, J_0 the incident flux density of hydrogen atoms per unit area, $R_p(E)$ the projected range of hydrogen atom of energy E , $\Delta R_p(E)$ the range straggling of hydrogen atom of energy E , and $B(E,\theta)$ the backscattering coefficient of hydrogen atom incident with energy E and angle θ . Gaussian range distribution of implanted particles is assumed here, eq.(4), in the case of random incidence. The range parameters $R_p(E)$ and $\Delta R_p(E)$ are calculated from the LSS theory [2,3].

Note that the factor $1-B(E,\theta)$ is multiplied with the normalization constant in the right hand side of eq.(4) to give the actual number of implanted particles by excluding the backscattered fraction. The following empirical formula for $B(E,\theta)$ is used in the calculations:

$$B(E,\theta) = B_0(E) + [1-B_0(E)](1-\cos\theta)^2, \quad (5)$$

where $B_0(E)$ is the backscattering coefficient for perpendicular incidence. This formula gives a good approximation, which we have confirmed by comparing it with a result from TRIM code calculation [4].

Surface compositional changes of the TiC wall is expected to occur by the bombardment with energetic charge exchange neutrals. One of them is carbon atom depletion from the TiC wall surface, which is mainly due to by chemical sputtering to form CH_4 and preferential sputtering of C atoms, lighter element of TiC. It finally makes the TiC wall surface a Ti-rich one at a high fluence of hydrogen, $\sim 1 \times 10^{19} \text{H/cm}^2$ [5]. The Ti-rich surface reacts with residual oxygen gas, but oxygen molecules reacts more easily with high flux hydrogen atoms, so that the

oxidation of Ti will not occur, theoretically. In practical tokamak machines, however, the Ti-rich surface will eventually get into oxidation from the following reasons: 1) sources of oxygen can not be eliminated, 2) oxidation goes on during interruption between discharge shots, 3) oxide once formed can not be reduced by atomic hydrogens within discharge duration. This has been observed so far in the decrease of gettering action of Ti flashed wall surfaces with increasing discharge shots in a number of conventional tokamaks. Therefore, we consider here hydrogen recycling at Ti and TiO₂ walls as well as TiC.

The calculated results from an empirical formula for B₀(E) by Tabata et al. [6] in Ti are used in the calculations. For TiC, average data of B₀(E) compiled by Eckstein and Verbeek [4] are used in low energy region (<1 keV), and experimental data by Schneider and Verbeek [7] are used in higher energy region (>2.5 keV). For TiO₂, the same data as for TiC are used here.

The boundary conditions of the diffusion equation (2) are given as follows: for TiC and TiO₂,

$$c(0,t) = c(d,t) = 0,$$

for Ti,

$$D \frac{\partial c}{\partial x} \Big|_{x=0} = K_r c(0,t)^2 \quad \text{at inner surface,}$$

$$-D \frac{\partial c}{\partial x} \Big|_{x=d} = K'_r c(d,t)^2 \quad \text{at outer surface,}$$

where K_r and K'_r are the recombination coefficients of hydrogen atom at inner and outer surfaces, respectively. The values of the recombination coefficients are estimated from the formula by Baskes [8].

Concerning the diffusion coefficients D , the following values in units of cm^2/s are used in the calculations:

$$D(T) = 0.018 \exp(-1.25 \times 10^4 [\text{cal/mol}]/RT), \text{ for Ti [9],}$$

$$D(T) = 1.31 \times 10^{-12} \exp(-3.05 \times 10^3 [\text{cal/mol}]/RT), \text{ for TiC [10],}$$

$$D(T) = 1.80 \times 10^{-5} \exp(-1.36 \times 10^4 [\text{cal/mol}]/RT), \text{ for TiO}_2 \text{ [11],}$$

where T is the wall temperature (in K), and R the gas constant. In the case of TiO_2 the normal diffusion coefficient in unbombarded materials is divided by 10^2 for the present re-emission calculation.

Hydrogen is re-emitted from the bulk of the wall when the hydrogen concentration $c(x,t)$ derived from the diffusion equation (2) exceeds the saturation concentration N_{SAT} . The measured data of N_{SAT} (in units of H/cm^3) are used: $N_{\text{SAT}} = 1.27 \times 10^{23}$ for Ti [12] and 2.5×10^{22} for TiC [13]. The same value of N_{SAT} for TiO_2 is assumed here as for TiC.

Since we have no computed results of the energy distribution function $f(E)$ for charge exchange neutrals in JT-60, it is assumed here to be Maxwellian. Although this is an approximation, it is not a bad one judging from other computed results [14,15]. A computer programme using the Crank-Nicolson equations have been made to solve eq.(2) under the boundary conditions and calculate numerically the hydrogen re-emission rate as a function of time and wall temperature.

It is reasonable to give zero to the value of b in eq.(1), since almost all ions leaving the plasma hit the limiter. We assume here that $\alpha = 0.3$, which is not an optimistic value judging from a model calculation which yields $0.25 \leq \alpha \leq 0.45$ [15]. As for the injected flux of neutrals, $\Gamma^{\text{NBI}} = 2.54 \times 10^{21} \text{ H/s}$ is

expected in JT-60. Thus we obtain $R = 1 - 5.92 \times 10^{21} / \Gamma^+$, where $\Gamma^+ = 60n/\tau_p$, since $V = 60 \text{ m}^3$ in JT-60. We have calculated here two cases when the incident fluxes of charge exchange neutrals Γ_W^0 are $1 \times 10^{22} \text{ H/s}$ and $3 \times 10^{22} \text{ H/s}$, respectively. These correspond to the flux densities J_0 of $1 \times 10^{16} \text{ H/cm}^2\text{s}$ and $3 \times 10^{16} \text{ H/cm}^2\text{s}$, respectively, since the projected area of the wall and limiter is nearly 100 m^2 in JT-60. These also correspond to the cases when the values of n/τ_p are $3.9 \times 10^{20} \text{ H/m}^3\text{s}$ and $1.17 \times 10^{21} \text{ H/m}^3\text{s}$, respectively. The former case is for low density (or high τ_p) and the latter one for high density (or low τ_p). The corresponding values of R are 0.75 and 0.92, respectively.

Figures 2-4 show the calculated results of R as a function of time when the energy distribution is assumed to be 400 eV Maxwellian. In the case of Ti, the thickness of the Ti layers is assumed to be 100 \AA . Each re-emission curve corresponds to the wall temperature listed in the figure in order from the bottom to the top. Note that the FLUX in these figures means the flux density J_0 . In table 1 are listed the calculated results of wall temperature regions for 10 s discharge, where the recycling coefficient is suppressed below the R values estimated above for two cases of J_0 of $1 \times 10^{16} \text{ H/cm}^2\text{s}$ and $3 \times 10^{16} \text{ H/cm}^2$. It is found in the table that the recycling coefficients in Ti for both cases are less than the R values at any temperature. But it should be noted that saturation overflow becomes very important in TiC and TiO_2 and often increases the recycling coefficient abruptly. The most realistic is the case for TiO_2 after a number of discharge shots. The results for TiO_2 show a better recycling behaviour than for TiC, because the suitable wall temperature region in TiO_2 shifts to lower temperatures

which are more realizable than in TiC. Therefore, the surface compositional change of TiC into Ti or TiO₂ will make no undesirable effects on the recycling rate control in JT-60. But it should be noted that hydrogens once trapped in these materials at low temperatures should be desorbed during the discharge off period by using thermal desorption which is available in JT-60 up to 500 °C.

Table 1

Wall temperature regions which satisfy the following conditions for 10 s discharge and 400 eV Maxwellian energy distribution: $R < 0.75$ for $J_0 = 1 \times 10^{16}$ H/cm²s or $R < 0.92$ for $J_0 = 3 \times 10^{16}$ H/cm²s.

| Material | $J_0 = 1 \times 10^{16}$ H/cm ² s | $J_0 = 3 \times 10^{16}$ H/cm ² s |
|------------------|--|--|
| TiC | 150 - 220 °C | 300 °C |
| Ti | optional | optional |
| TiO ₂ | 60 - 80 °C | 80 - 130 °C |

References

- [1] K. Sone and Y. Murakami, Symp. on Energy Removal and Particle Control in Toroidal Fusion Devices, July 1983, Princeton, USA (in press in J. Nucl. Mater.)
- [2] J. Lindhard, M. Scharff and H. E. Schiøtt, Kgl. Danske Vidensk. Selsk. Mat.-Fys. Medd., 33 (1963) NO.4.
- [3] H. E. Schiøtt, *ibid.*, 35 (1966) No.9.
- [4] W. Eckstein and H. Verbeek, Max-planck-Institut für Plasmaphysik Report, IPP 9/32 (1979).
- [5] H. Tanaka, K. Saiki, S. Otani, A. Koma and S. Tanaka, J. Nucl. Mater., 116 (1983) 317.
- [6] T. Tabata, R. Ito, K. Morita and Y. Itikawa, Japan. J. Appl. Phys., 20 (1981) 1929.
- [7] P. J. Schneider and H. Verbeek, J. Nucl. Mater., 97 (1981) 319.
- [8] M. I. Baskes, J. Nucl. Mater., 92 (1980) 318.
- [9] J. R. Morton and D. S. Stark, Trans. Faraday Soc., 56 (1960) 354.
- [10] R. Yamada and K. Sone, to be published.
- [11] O. W. Johnson, S. H. Pael and J. W. Deford, J. Appl. Phys. 46 (1975) 1026.
- [12] J. Roth, W. Eckstein and J. Bohdansky, Radiat. Effects, 48 (1980) 231.
- [13] B. L. Doyle, W. R. Wampler, D. K. Brice and S. T. Picraux, J. Nucl. Mater., 93&94 (1980) 551.
- [14] H. C. Howe, J. Nucl. Mater., 93&94 (1980) 17.
- [15] K. Audenaerde, G. A. Emmert and M. Gordinier, J. Comp. Phys., 34 (1980) 268.

Figure Captions

Fig. 1 Schematic representation of the flow of the recycled particles.

Γ^{NBI} : flux of injected high energy neutrals,

Γ^{W} : total flux of neutrals re-emitted from the wall, which consists of the fluxes due to backscattering, diffusion and saturation overflow,

$\Gamma_{\text{W}}^{\text{O}}$: total flux of charge exchange neutrals impinging on the wall,

Γ^{L} : flux of neutrals re-emitted from the limiter,

Γ_{L}^{+} : flux of ions impinging on the limiter,

Γ_{W}^{+} : flux of ions impinging on the wall,

Γ^{+} : total flux of ions leaving the plasma.

Fig. 2 Calculated recycling coefficients as a function of time and wall temperature in TiC for a Maxwellian energy distribution of 400 eV.

Fig. 3 Calculated recycling coefficients as a function of time and wall temperature in Ti for a Maxwellian energy distribution of 400 eV. a) $J_0 = 1 \times 10^{16}$ H/cm²s and b) $J_0 = 3 \times 10^{16}$ H/cm²s.

Fig. 4 Calculated recycling coefficients as a function of time and wall temperature in TiO₂ for a Maxwellian energy distribution of 400 eV.

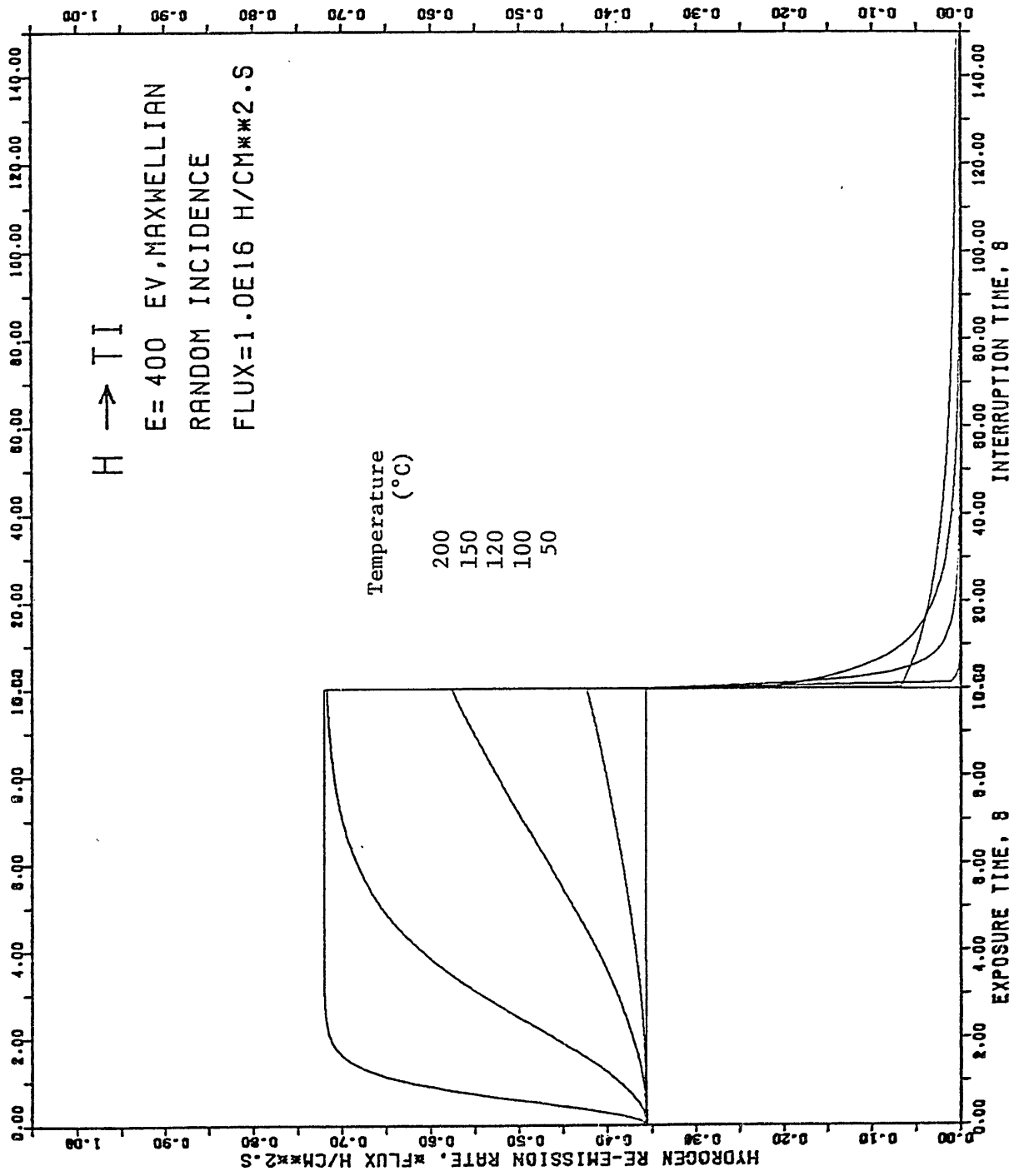


Fig. 3 a)

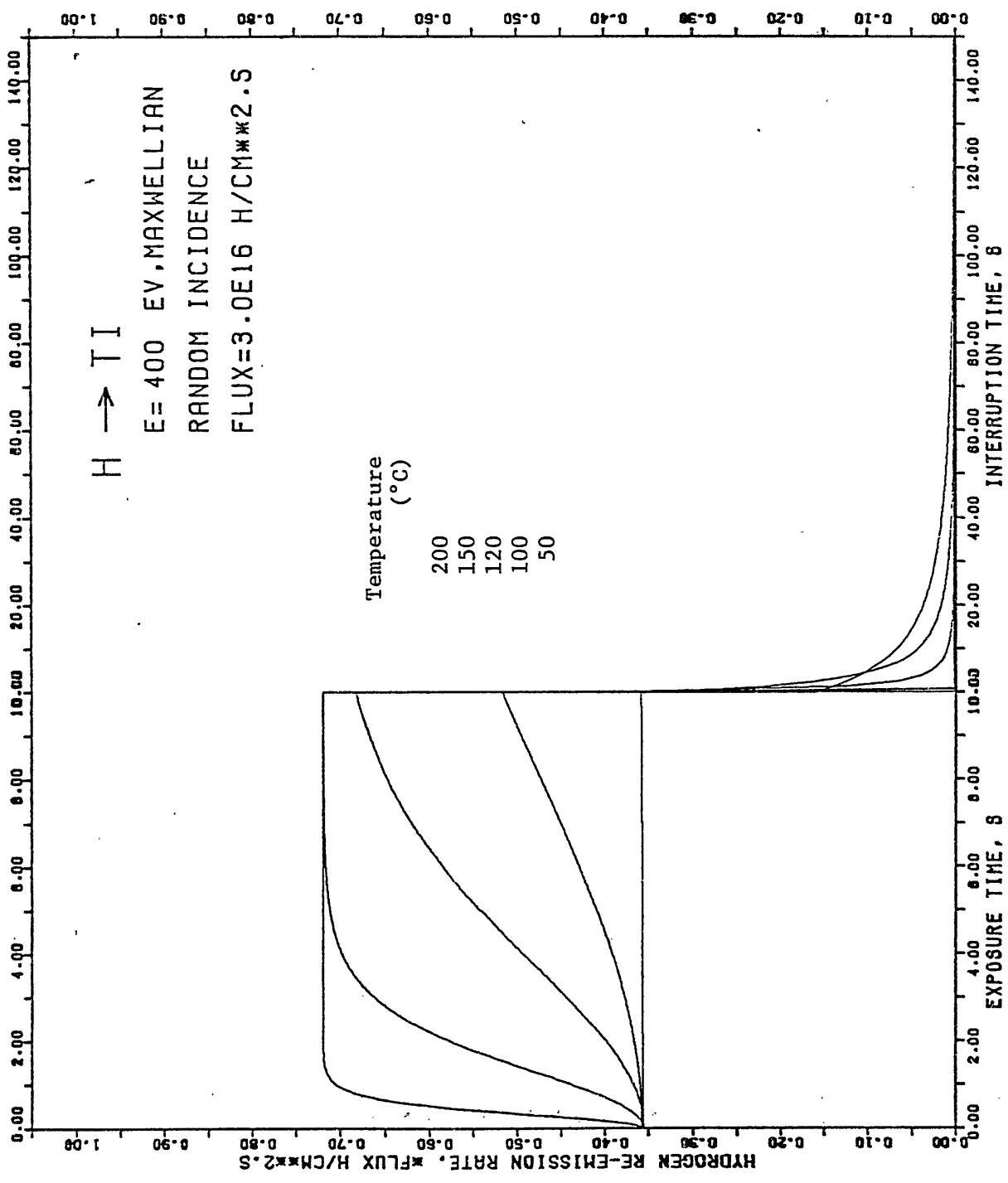


Fig. 3 b)

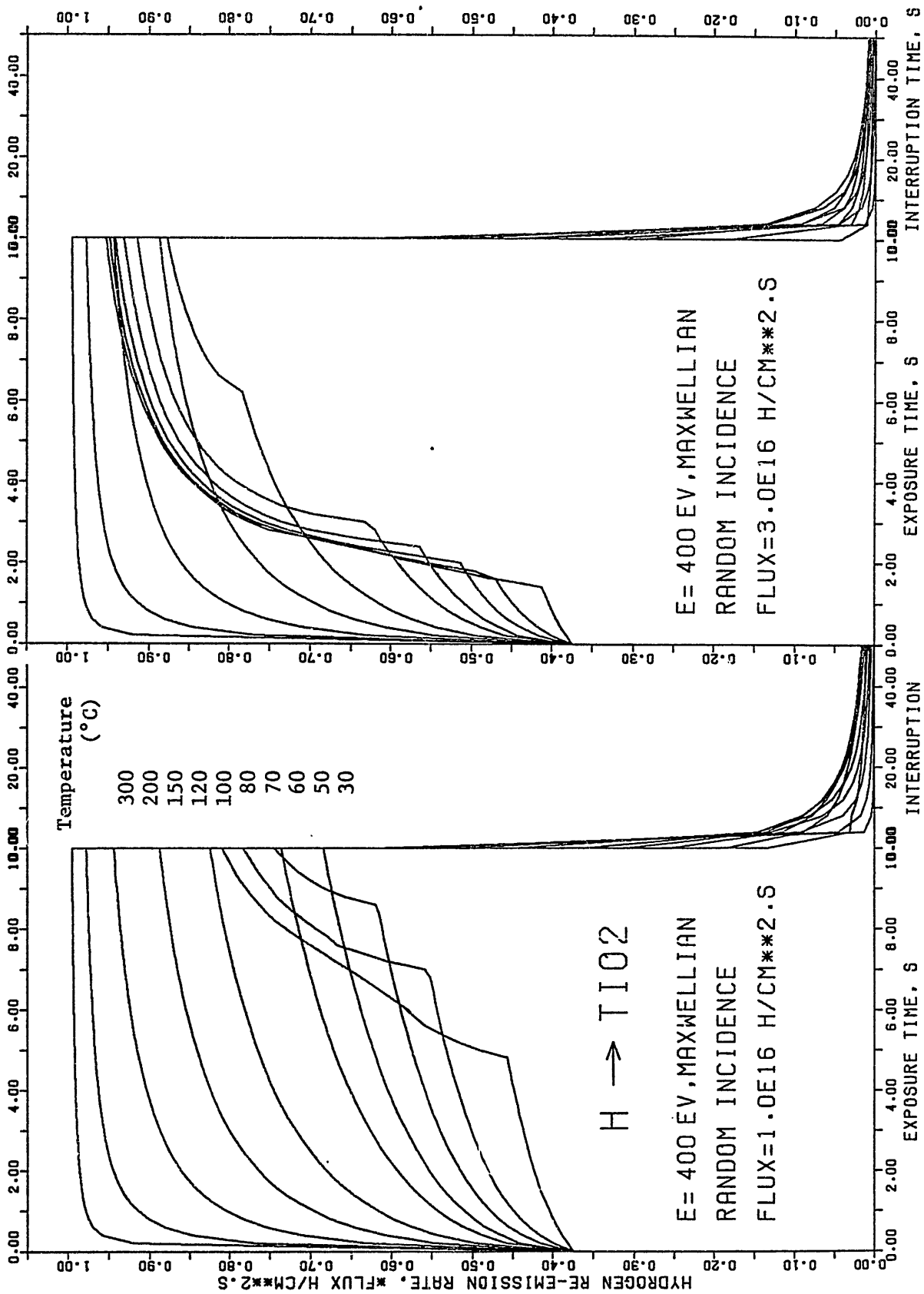


Fig. 4

IMPURITY TRANSPORT EXPERIMENT BY SURFACE DEPOSITION PROBE IN JIPP T-IIU

M. Mohri and T. Yamashina

Department of Nuclear Engineering, Hokkaido University,

Sapporo 060, Japan

INTRODUCTION

Reduction of metallic impurities in plasma has been realized to be very important in the present day torus devices. There are a number of impurity generation processes such as sputtering, blistering, flaking and evaporation from a view point of first wall surfaces, and arcing, disruption and runaway electron from a view point of plasma. One of the most important objectives in the study of plasma surface interactions is to understand and to control the production of impurities. Ti gettering has been often applied in many torus devices as a standard technique to reduce gaseous impurities.

In the present work we reported the effects of Ti gettering on the generation process of metallic impurities during plasma discharges in JIPP T-IIU.

EXPERIMENTAL

The JIPP T-IIIU tokamak device is a modified system of the JIPP T-II stellarator/tokamak device and has been operated since May 1983. The major radius and minor radius are 91 cm and 23 cm, respectively. A schematic representation of the system is shown in Figure 1. The vacuum chamber is constructed with 304SS. The two fixed ring limiters and a pair of rail limiters are also made of 304SS and are located at the distance of 25 cm and 23 cm, respectively from the center line of plasma as shown in the figure. Four ring-shaped bellows protectors made of Mo are located at the distance of 25 cm from the center line of plasma. The positions of three Ti evaporation sources for gettering and ICRH antennas are also shown in the figure. The surface deposition probe with a box structure made of 304SS as shown in Figure 2 was inserted in the scrape-off plasma region through the P6 port. Five sides of the probe were mounted with 304SS foils coated with amorphous silicon with a thickness of 1 μm and they are designated as shown in Figure 2. Three identical surface deposition probes were prepared and each one of them was exposed to only one plasma discharge with ICRH heating. In order to observe the effect of Ti gettering the first surface deposition probe (SDP-1) was exposed to the plasma without any Ti flashings. The second probe (SDP-2) was exposed to the plasma just after the first Ti flashing from a P14 Ti evaporation source in the history of JIPP T-IIIU device. Then the third probe (SDP-3) was exposed to the plasma after a number of Ti flashings from p5, p14 and P15 Ti evaporation sources.

RESULTS AND DISCUSSION

PIXE(Particle Induced X-ray Emission) and RBS (Rutherford Back-scattering) measurements showed that Fe, Cr and Ni were major metallic impurities deposited onto the probe. Mo was also observed and its amount was almost one order of magnitude smaller than that of Fe. Figure 3 shows that the depth concentration profiles for impurity elements observed on the P side of the three probes measured by a sputter AES(Auger Electron Spectroscopy) method. Plasma discharge parameters are also included in the figures. Three plasmas can be regarded as almost identical. Before Ti flashings, about 4 % of the surface of P-side was covered by Fe atoms. As shown in figure 1 the Ti flashing from the P14 evaporation source can cover two third of the whole area of the inner vacuum vessel. After the flashing, the amount of Fe impurity deposited on the probe decreased and its surface concentration fell down to less than 1 %. However, no Ti signal was observed on the SDP-2 probe by AES analysis. After Ti flashings from the three Ti evaporation sources, the amount of Fe impurity remarkably decreased and almost the same amount of Ti impurity was observed as shown in Figure 3c. The surface concentration of C and O did not show any significant differences before and after Ti flashings. This may be due to the fact that the probe surface was exposed to the air after the plasma exposure so that the top surface could be contaminated with

hydrocarbons and water vapors. However, if the depth concentration profiles of C and O are compared carefully, one may be able to find that the thickness of oxygen layer in the surface region decreased slightly while that of C slightly increased.

Light impurities such as Ca, K and S decreased remarkably after the Ti flashings.

Figures 4a and 4b show VUV spectra of O V and C IV in the main plasma during discharges, respectively. They revealed that the relative amount of O V impurity existing in the main plasma during discharges decreased significantly while that of C IV impurity did not change significantly. A large increase was observed in the signal intensity of Ti VIII as Ti flashings were carried out while a slight decrease in the Fe VIII signal intensity was observed in the VUV spectra of Ti VIII and Fe VIII.

The Ti flashings were found to retard the production and the deposition of Fe impurity. This result is quite reasonable since the surface of the inner wall of vacuum chamber was coated with Ti atoms. However, the increase of Ti deposition was not very large in comparison to the sharp decrease of Fe after Ti flashings.

The fact that the amount of O impurity in the main plasma decreased remarkably after the Ti flashings suggest that the deposition of Fe and Ti onto the probe is caused by the sputtering of the wall or limiter surfaces by O impurity from the plasma.

SUMMARY

Fe was the major metallic impurity observed on the surface probe by AES analysis. While its amount decreased remarkably after Ti flashings. This could be interpreted by the reduction of oxygen impurity in plasma which generated Fe impurity from the wall surface through the sputtering process.

Acknowledgement

We wish to acknowledge T. Katoh and S. Amemiya (Department of Nuclear Engineering, Nagoya University) for the PIXE and RBS measurements, and N. Noda (IPP Nagoya University) for the VUV measurements.

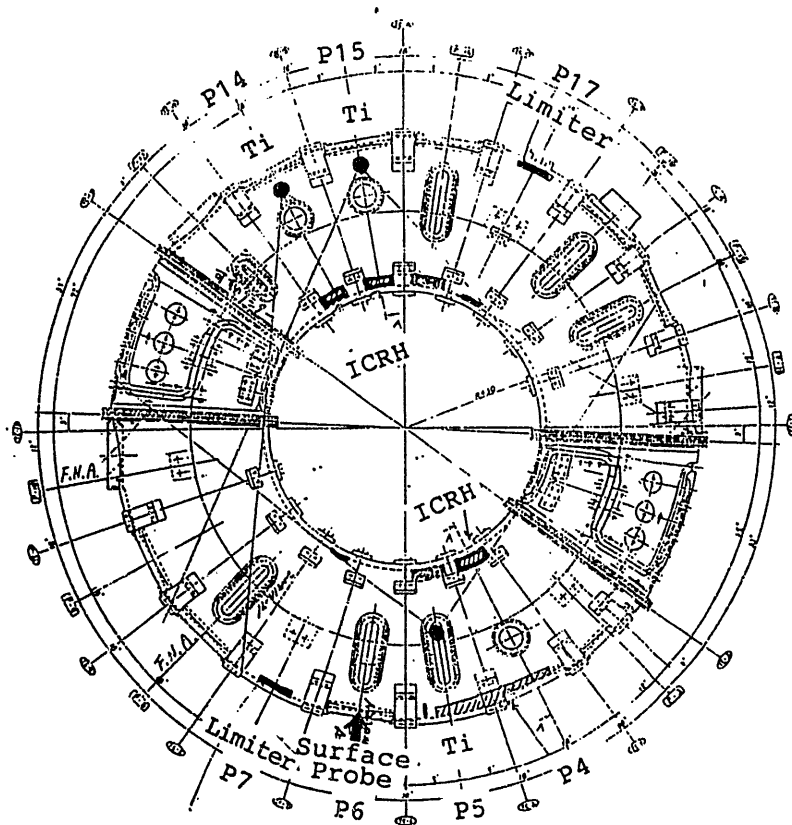


Figure 1. Schematic Representation of JIPP T-IIU

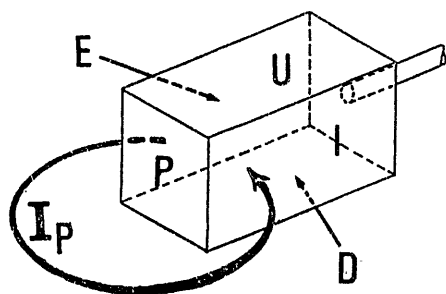


Figure 2. Surface Deposition Probe

- I; ion drift side
- E; electron drift side
- P; plasma front side
- U; upper side
- D; down side

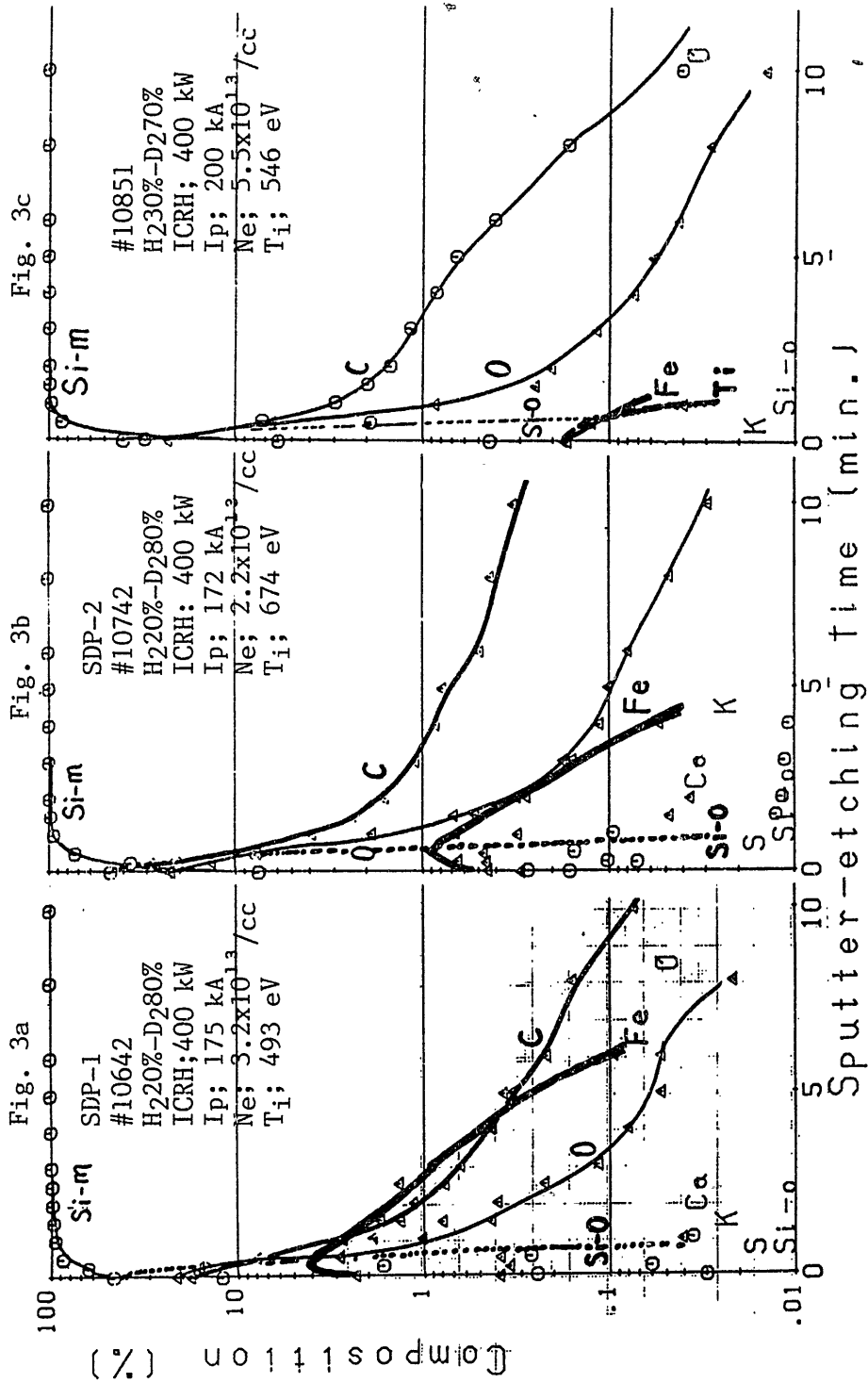


Figure 3. AES In-depth Composition Profiles of Impurity Atoms Deposited on the Surface Deposition Probe Exposed into JIPP T-IIU Plasma Discharges with and without Ti Flashings.

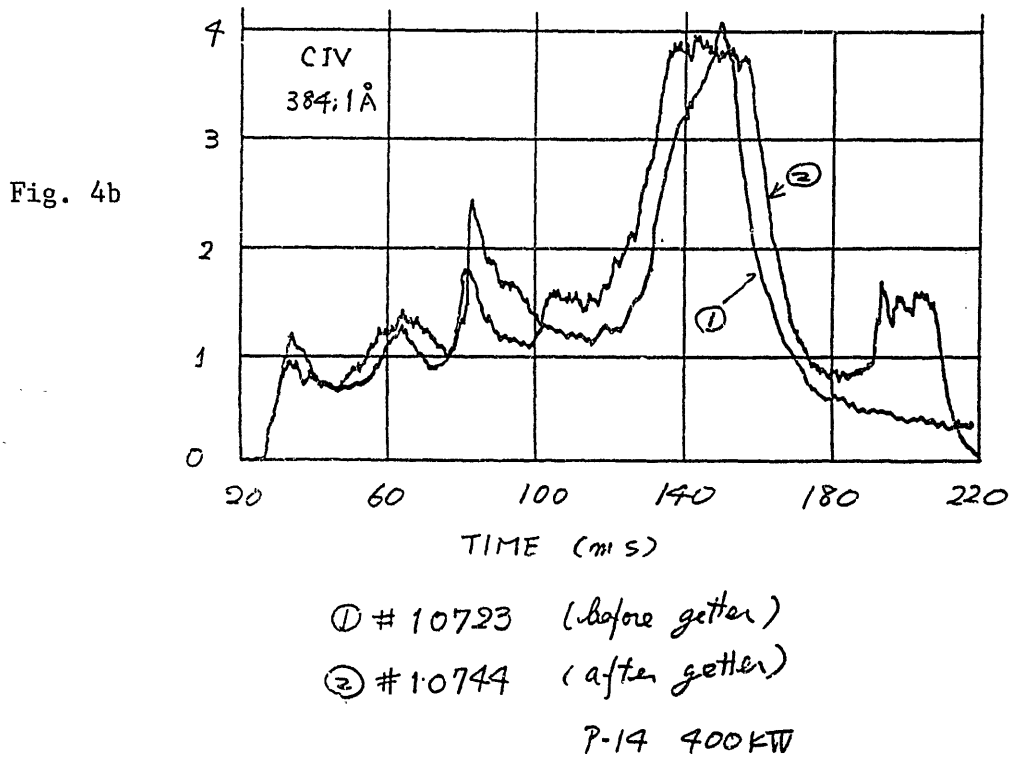
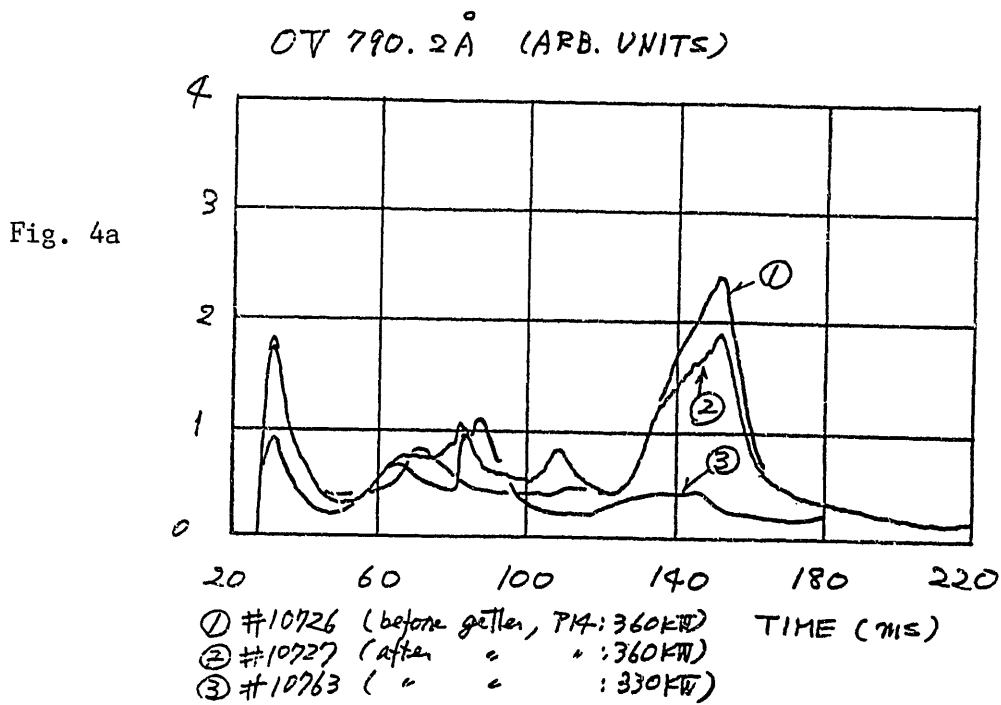


Figure 4. VUV Spectra of O V and C IV during Plasma Discharges before and after Ti Flashings.

STUDY ON ALPHA-PARTICLE DIAGNOSTICS
IN MAGNETICALLY CONFINED PLASMAS

K.N. Sato and M. Sasao
Institute of Plasma Physics, Nagoya University
Chikusa, Nagoya 464, JAPAN

Reacting plasma experiments in a medium-sized tokamak have been planned at IPP-Nagoya, Japan. One of the main subjects of the "R-Project" is to study the details of reacting plasma physics related to the fast alpha-particles produced through D-T reactions.(Table-I) For this purpose the possibility of confined alpha-particle diagnostics has been investigated quantitatively.

Several approaches for this diagnostics have been studied in detail; for example, beam probe method,¹⁾ nuclear reaction method and laser scattering method etc.(Table-II) Among them the beam probe method seems to be the most probable one for this purpose.

The alpha-particle diagnostics by charge exchange method has been planned to be applied on the R-tokamak. The beam velocity of about $0.8V_{\alpha}^{\circ}$ is appropriate in order to obtain a wide spectral range of the velocity distribution of alpha particles and to reduce the beam acceleration power. (Where, V_{α}° is the initial velocity of alpha particles produced by D-T reactions.)

Although a Li beam is one possible candidate as a probing beam, a ^3He beam is more advantageous from the viewpoints of larger charge exchange cross sections and lower acceleration voltage needed. As is well known, the He° beam neutralized

through a conventional gas cell has a problem of large fraction of metastable atoms, which will not penetrate into the center of the plasma. A new method is proposed²⁾ to utilize the auto-detachment process of He^- ions in order to have a large fraction of ground state He^0 atoms. Since He^- ions have two components of life time, i.e. about 345 μs and 11 μs (50% each), one can obtain a 24 % ground state neutral atoms with the flight distance of 30 m at the beam velocity of $0.8V_\alpha$. The beam divergence including space charge effect seems to be not so serious in the flight. Several paths of the beam probing method are shown in Fig.1.

The yield estimation of alpha particles neutralized by double charge exchange processes shows that a 10 mA $^3\text{He}^-$ or Li^- beam at the velocity of $0.8V_\alpha$ will enable us to measure the alpha-particle velocity distributions with reasonable spatial and temporal resolutions. (Fig. 2)

In this connection the electron capture cross sections in $\text{He}^{2+} + \text{Li}$ collisions have been obtained experimentally in the energy range of about 0.8 - 2.0 MeV³⁾. (Fig.3) A preliminary study on the negative ion source has been started.

Fundamental researches on high speed pellet injection technique has also been carried out in order to have another approach of this diagnostics.

References

- 1) D.E. Post *et al.*, J. Fusion Energy 1(1981)129
- 2) M. Sasao and K.N. Sato, Annual Rev. IPP-Nagoya (April 1981 - March 1982) p.52
- 3) M. Sasao *et al.*, Proc. of 13th ICPEAC (Berlin, 1983) 3KL63

Table and Figure Captions

Table-I Research subjects and its diagnostics on reacting/burning plasma physics.

Table-II Several methods of the alpha-particle diagnostics being studied at IPP-Nagoya.

Fig. 1 Several paths of the beam probing method.

Fig. 2 Schematic diagram and possible parameters of alpha-particle diagnostics by the beam probing method in the R-tokamak.

Fig. 3 Measured electron capture cross sections as a function of relative velocity in $\text{He}^{2+} + \text{Li}$ collisions.

Table-I. Research Subjects and Its Diagnostics on Reacting/Burning Plasma Physics

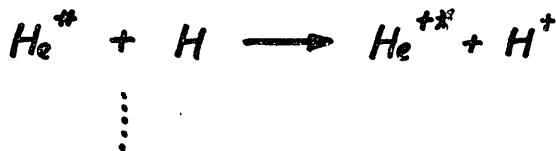
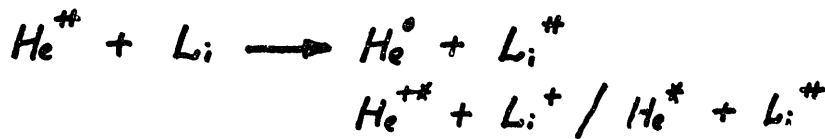
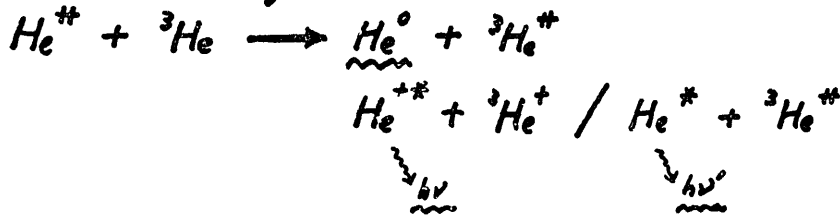
| Subject | Diagnostics | | | DOD* | Expected Gain |
|---|--|--------------------------------------|--|--|---|
| | Method | Items | Limit | | |
| [1] Q-value | Neutron | N_n, P_{NBI}^{IN} | Q-0.03 | B | Confirmation of reacting (and burning) Plasma |
| | (α | N_α, P_{NBI}^{IN} | | D | |
| | (γ | N_γ, P_{NBI}^{IN} | | D | |
| [2] Fundamental Properties | | | | | |
| (1) <u>Slowing down of α-particles</u> | <u>Confined-α</u> | $f_\alpha(v,t)$ $f_\alpha(v,r,t)$ | Q-0.1 Q-0.3-1 | D \rightarrow C D \rightarrow C | i) Basic knowledge for self-heating ii) Conditions for collective behaviors |
| (2) Loss Mechanism of α -particles | { Neutron + Lost- α | N_n N_α | Q-0.03 | B D | i) Criteria for field ripple ii) Knowledge for control of Thermonuclear instabilities, thermal instability and ash removal |
| (3) Wave excitation by α -particles and its effect (Thermonuclear instability) | { FIR laser scattering Beam Probe | \tilde{n}_e \tilde{B} | $\frac{\tilde{n}_e}{n_e} \sim 10^{-2}$ | C D | Basic information as to control method for these instabilities |
| (4) Excitation of radial electric field and its effect | { Beam Probe Doppler shift Poloidal mode | ψ v_θ v_θ | $E_r \sim 10^V/cm$ | C B B | Basic informations as to control method for E_r |
| [3] α -particle Heating (and energy balance) | { T_i T_e P_{wall}^e | T_i T_e P_{wall}^e | Q-3 | C B C | Knowledge for the design of fusion reactor |
| [4] Thermal instability | { Neutron T_i | $N(r,t)$ T_i^n | | B C | Knowledge for the design of fusion reactor |

* DOD = Degree of Difficulty: A = easy (or established), B = not so difficult, C = essentially possible, but need R&D to some extent, D = need R&D to considerable extent.

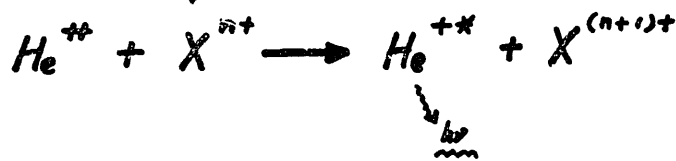
Table-II Several methods of the alpha-particle diagnostics being studied at IPP-Nagoya.

[A] Charge Exchange Method

(1) Beam Probing



(2) Pellet Injection



[B] Nuclear Reaction Method (Pellet Injection)

| | E_{α} [MeV] | E_{γ} [MeV] |
|---|--------------------|--------------------|
| $\Rightarrow {}^9\text{Be} (\alpha, n) {}^{12}\text{C}$ | <u>5.27</u> | <u>4.44</u> |
| ${}^{13}\text{C} (\alpha, n) {}^{16}\text{O}$ | 2.09 | |
| ${}^{23}\text{Ne} (\alpha, n) {}^{26}\text{Mg}$ | 2.45 | 1.37 |
| ${}^{25}\text{Mg} (\alpha, n) {}^{28}\text{Si}$ | 2.56 | 1.78 |

[C] IR Laser Scattering Method

Collective scattering

《 Confined α -Particle Diagnostics 》

[1] Charge Exchange Method (Beam Probe Method)

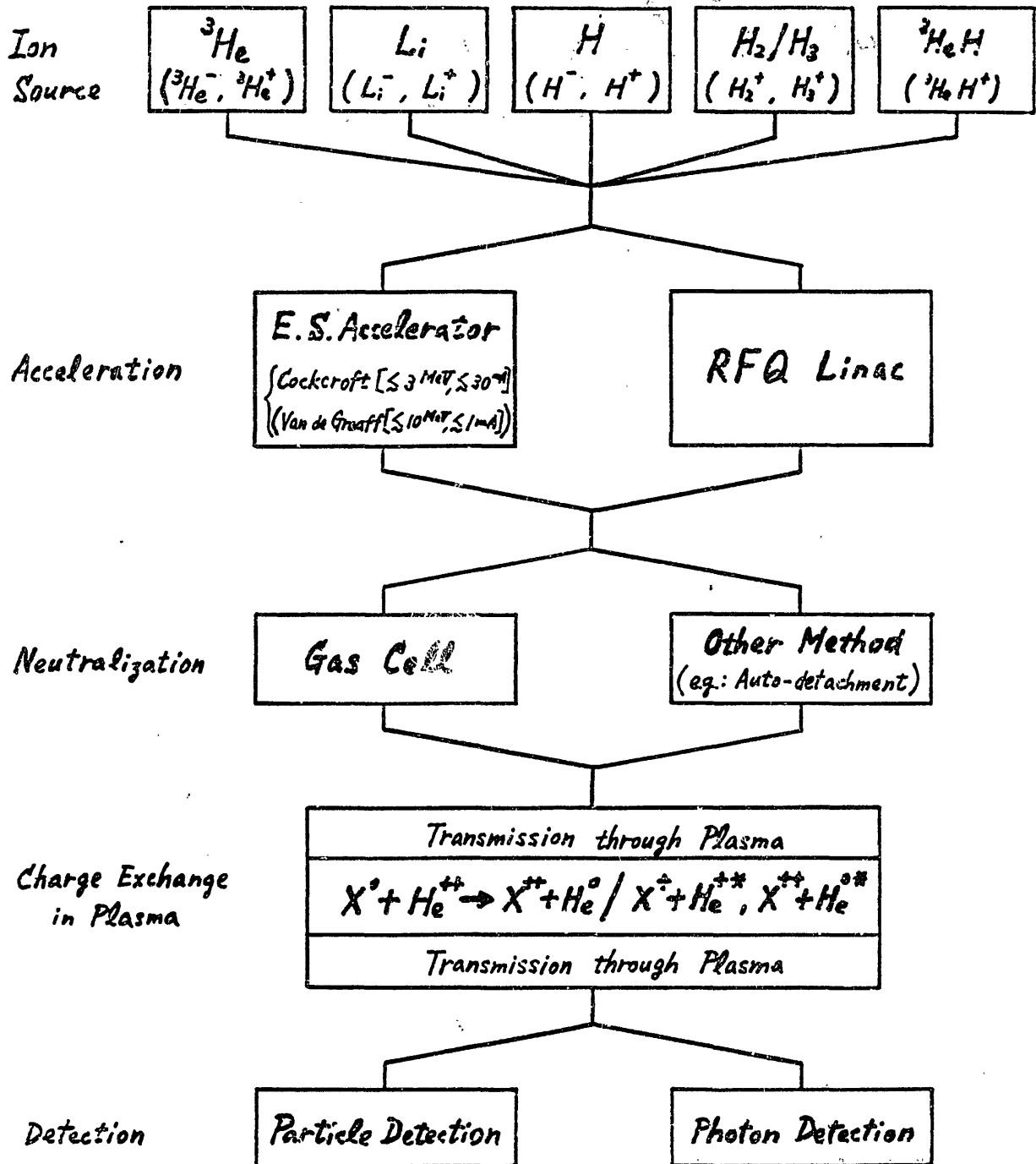
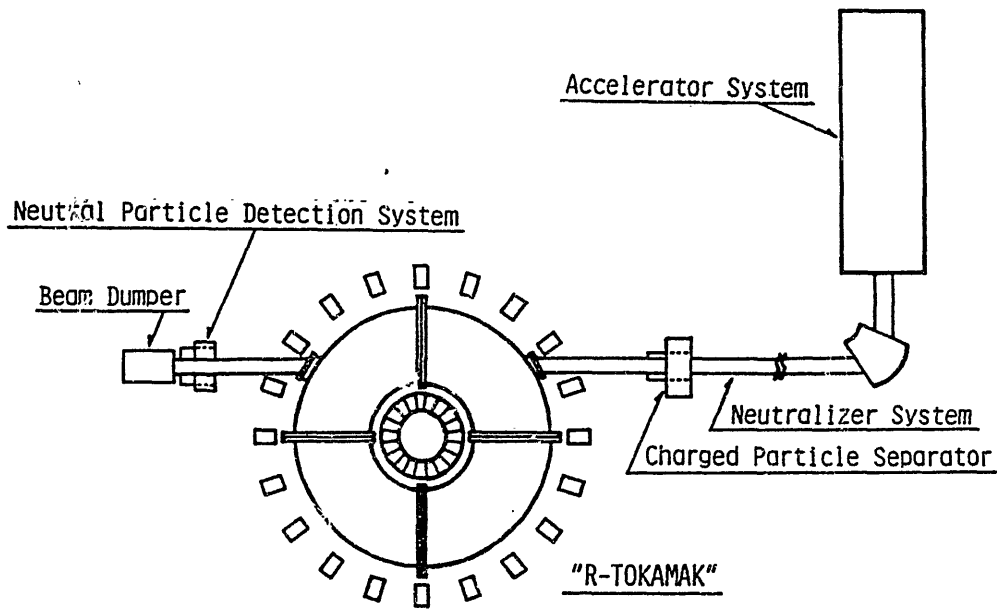


Fig. 1 Several paths of the beam probing method.



Schematic diagram of alpha - particle diagnostic system by the charge exchange method in the " R - tokamak " .

< Target Plasma >

$$n_{\alpha} \approx 1 \times 10^{11} \text{ cm}^{-3} \quad (n_{\alpha}/n_e \approx 10^{-3})$$

< Injection Beam >

$${}^3\text{He}^{-} \text{ (or } \text{Li}^{-}\text{)}$$

$$I_0 \approx 10 \text{ mA}$$

$$v/v_{\alpha}^0 \approx 0.8 \quad (\text{variable: } 0.3 \sim 0.8)$$

$$D_{\text{beam}} \approx 10 \text{ cm}\phi \quad (\text{or } 10 \text{ cm} \times 1 \text{ m})$$

< Detection System >

$$L \approx 5 \text{ m}$$

$$\theta \approx 10^{\circ}$$

$$\Delta v = 0.025 v_{\alpha}^0$$

$$\text{Detector size: } (1 \text{ cm}^2 \text{ Detector}) \times (3 \times 3)^{\text{set}} \times 5 \dots \text{ for example}$$



* Resolving Power

$$\Delta v = 0.025 v_{\alpha}^0$$

$$\Delta r \approx 10 \text{ cm}$$

$$\Delta t \approx 100 \text{ ms}$$

$$\left. \begin{array}{l} \Delta v = 0.025 v_{\alpha}^0 \\ \Delta r \approx 10 \text{ cm} \\ \Delta t \approx 100 \text{ ms} \end{array} \right) (S/N)_{\text{min}} \geq 10 \Rightarrow \boxed{f(v; r, t)}$$

Fig. 2

Schematic diagram and possible parameters of alpha-particle diagnostics by the beam probing method in the R-tokamak.

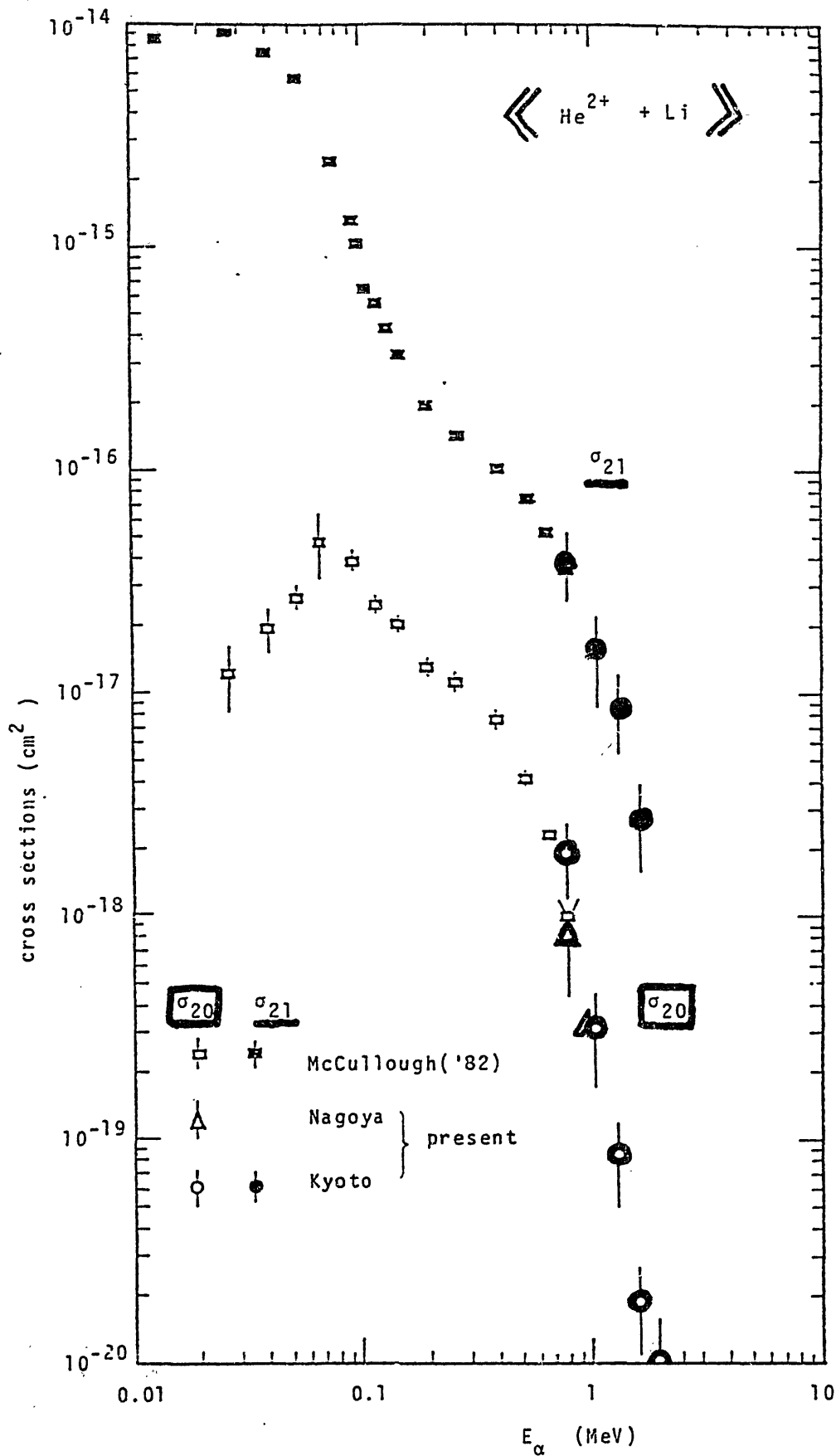


Fig. 3. Measured electron capture cross sections as a function of relative velocity in $\text{He}^{2+} + \text{Li}$ collisions.

Ignition simulation by the interaction of NBI with ICRF

Y. Hamada, Y. Oqawa, T. Amano and T. Watari

Institute of Plasma Physics, Nagoya University, Nagoya, Japan

Abstract

Efficient production of high energy ion tail by the NBI accelerated by ICRF at the higher harmonics of ion cyclotron wave, is discussed. The linear damping across the resonance layer may be small for single transit. The quasi-linear damping however is sufficiently large to give the velocity distribution similar to that of alpha particles in ignited plasma. The quasi-steady state velocity distribution function can be obtained by the reduced acceleration near the null point of Bessel function, suppressing ion runaway in cyclotron harmonics acceleration.

The scaling formula of the energy confinement time in high temperature plasma is one of the most urgent target of the experimental research. The ambiguity of the scaling near ignition plasma impells the design of the ignited plasma to have a large margin corresponding to that ambiguity, resulting in the expensive machine.

The ignited plasma may be characterized by high temperature plasma heated by the alpha particles produced by the DT reaction. Recently D. Post suggested that D-³He ICRF heating may produce the alpha particle-like velocity distribution of ³He and may heat the plasma through its high energy minority ions. In this paper the new method for the production of alpha particle-like distribution of ions through the coupling of injected ions of NB with the ion cyclotron harmonics waves, is presented.

The damping of the ICRF wave at ion cyclotron harmonics is first analysed by the linear theory. In Fig. 1 the dispersion of fast wave at the 3rd harmonics near the resonance and the power flux across the resonance layer are shown under the assumption of two component plasma of the NBI heated plasma. The linear damping about 10% can be obtained across the resonance layer.

The behaviour of the ion tail distribution is analysed by the quasilinear Fokker Planck equation derived by T. Stix. The absorption due to the generated high energy tail is found to be strong even to the 3rd and 4th harmonics of the ion cyclotron frequency. It is possible to generate high energy tails in the higher electron density, under lower toroidal magnetic field strength, and in case of lower electron temperature compared with the use of D-³He. The development of the high energy tail is impeded when $k\varrho_i$ approaches the null point of Bessel function and steady state velocity distribution similar to that of the alpha particle in high Q and ignited plasma can be obtained by the appropriate choice of plasma density and toroidal field strength as shown in Fig. 2.

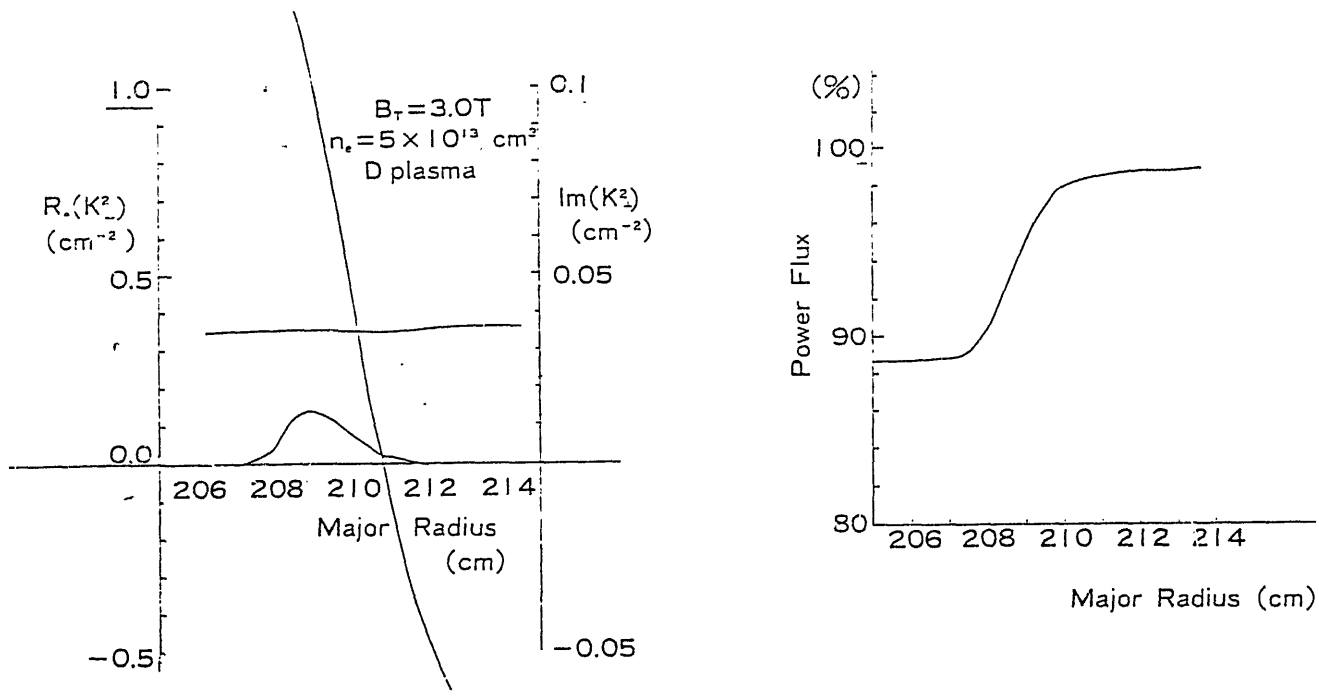


Fig. 1 Dispersion and power flux in linear theory

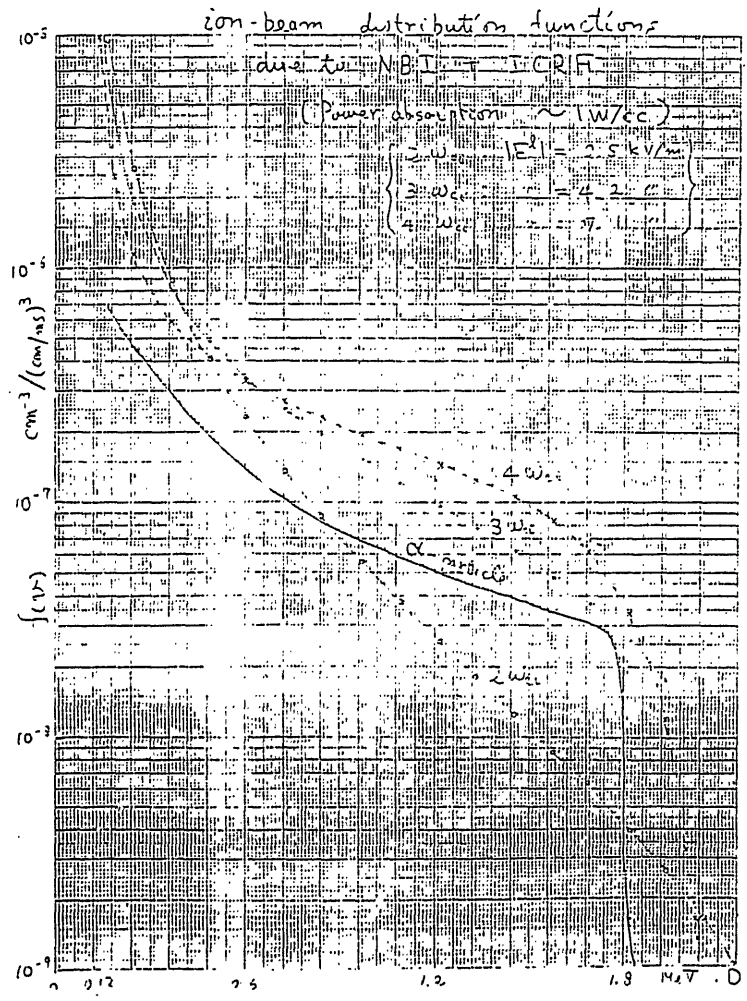


Fig. 2 Results of quasi-linear Fokker-Planck code

TOKAMAK IMPURITY CONTROL WITH MOMENTUM SOURCES
THEORY AND APPLICATION

D. J. Sigmar, Oak Ridge National Laboratory
and
W. M. Stacey, Jr. Georgia Institute of Technology

(An extended version of this work has been submitted for
publication in "Nuclear Fusion" 1984)

ABSTRACT

We have extended our previous collisional-regime theory for rotation and impurity transport in a tokamak plasma with strong, directed NBI and strong rotation ($v_\phi \sim v_{th}$) to the mixed collisionality regime. We present a self-consistent formalism for calculating ion and impurity rotation velocities and radial transport fluxes, as well as the radial electric field and the poloidal variation of the impurity density upon which the former strongly depend. Calculations for model problems representative of ISX-B and PLT are presented. The predicted impurity transport exhibits features in agreement with experimental observations.

INTRODUCTION

There is a long-standing interest in the possibility of using directed neutral beam injection (NBI) to reverse the normal inward diffusion of impurities in tokamak plasmas. Ohkawa [1] noted that the direct momentum exchange of injected beam particles and impurities via collisions would produce a radial impurity transport flux and predicted that counterinjection would produce an outward impurity transport flux.

Stacey and Sigmar [2] noted that the injected beam momentum must be balanced by a radial transfer of momentum, or drag, and that this allowed a unique determination of the radial electric field. They predicted that when the effect of the momentum input and drag on the particle flows was taken into account and when the effect of the radial electric field on transport was treated self-consistently, then coinjection would produce an outward impurity flux.

Burrell, Ohkawa and Wong [3] pointed out that the large toroidal rotation velocities associated with directed NBI could produce poloidal non-uniformity in the impurity density over the flux surface, which in turn could produce a radial impurity transport flux. This effect becomes significant when the impurity rotation velocity becomes comparable with its thermal velocity. They predicted that coinjection would produce an outward impurity flux due to this rotation, or inertial, effect. This theory was not self-consistent with respect to the ambipolar electric field, however.

Recently, Stacey and Sigmar [4] extended their previous formalism [2] to include this rotation effect in a self-consistent theory for particle flows in the flux surface, the radial electric field and radial particle transport in a tokamak plasma in the collisional regime with directed NBI. A more extensive discussion of relevant previous work is given in that paper [4].

Experimentally, it has been observed in PLT [5,6] and ISX-B [7,8] that the central accumulation of edge-introduced impurities is much greater with counter-injection than with co-injection, in qualitative agreement with the more recent theory. Attempts [8,9] to quantitatively interpret some of the experimental results with earlier, incomplete versions [2,3] of the theory have been encouraging, although unable to explain all features of both the co-injected and counterinjected results.

The purpose of this paper is to extend our previous theory [4] for the collisional regime into the plateau regime. This extension accomodates the important case of the main ion species being nearly collisionless and the impurity species being collisional, which we refer to as the mixed regime. This extension requires a kinetic theory solution for the parallel viscous force $B \cdot \nabla \cdot \bar{v}$ in the presence of large rotation velocities and an incorporation of this viscous force into the fluid theory. We find in the mixed collisionality regime that the mechanisms dominating the transport processes are quite different than in the collisional regime.

The theory described in this paper provides a self-consistent (non-linear) model, based upon particle and momentum conservation and charge neutrality, for calculating toroidal and poloidal rotation velocities, the radial electric field and radial particle fluxes in a two-species (ion-impurity) tokamak plasma with strong directed neutral beam injection, and resulting large rotation velocities. The theory relies upon neoclassical theory for specification of the parallel viscous force (including the plateau resonance) but allows for an anomalous viscous radial transfer of toroidal momentum as indicated by experimental data [7,10]. Prescriptions are given for determining the anomalous radial momentum transfer rates from measured rotation velocities for the ions and impurities. In the final section, the formalism is applied to plasmas with the gross features of ISX-B and PLT to predict certain features that are observed in the experiments.

REFERENCES

1. T. Ohkawa, Kaku Yugo Kenkyu, 32, 1 (1974).
2. W. M. Stacey, Jr., D. J. Sigmar, Phys. Fluids, 22, 2000 (1979); also Nucl. Fusion, 19, 1665 (1979).
3. K. H. Burrell, T. Ohkawa, S. K. Wong, Phys. Rev. Lett., 47, 511 (1981).
4. W. M. Stacey, Jr., D. J. Sigmar, "The Effects of Neutral Beam Injection on Impurity Transport in Tokamaks", Georgia Institute of Technology report GTR-43 (1984) also Phys. Fluids, submitted.
5. D. R. Eames, Ph.D. Thesis, Princeton Univ. (1980).
6. S. Suckewer, et al., "Ion Transport Studies on the PLT Tokamak During Neutral Beam Injection", Princeton report PPPL-2063 (1983); also Nucl. Fusion, submitted.
7. C. E. Bush, et al., Nucl. Fusion, 23, 67 (1983).
8. R. C. Isler, et al., Nucl. Fusion, 23, 1017 (1983).
9. W. M. Stacey, Jr., R. B. Bennett, D. J. Sigmar, "Neutral Beam Driven Impurity Flow Reversal in Tokamaks", Georgia Institute of Technology report GTR-42 (1983); also J. Nucl. Mat., to be published.
10. S. Suckewer, et al., Nucl. Fusion, 21, 1301 (1981); also Phys. Rev. Lett., 43, 207 (1979).

II. FLUID THEORY

Outline of Derivation

The construction of the expressions for the radial electric field, particle flows within the flux surface, poloidal variation of the particle densities over the flux surface and transport fluxes across the flux surfaces closely parallels that of Ref. [4] treating the collisional regime to which we refer the reader interested in the details. In this section, we will outline the derivation and proceed in subsequent sections to present and discuss the new results for the mixed regime.

The basic equations are the particle continuity equation for species j

$$\nabla \cdot n_j \vec{v}_j = 0, \quad (19)$$

the momentum balance equation for species j

$$\begin{aligned} n_j m_j (\vec{v}_j \cdot \nabla) \vec{v}_j + \nabla p_j + \nabla \cdot \vec{\pi}_j = -n_j e_j \nabla \phi \\ + n_j e_j (\vec{v}_j \times \vec{B}) + \vec{R}_j + \vec{N}_j, \end{aligned} \quad (20)$$

and charge neutrality

$$\sum_{j=1}^J n_j e_j = 0. \quad (21)$$

In Eq. (20), \vec{R}_j is the interspecies friction, which we will represent by

$$\vec{R}_j = -n_j m_j \sum_{k \neq j} \nu_{jk} (\vec{v}_j - \vec{v}_k); \quad (22)$$

and

$$\vec{N}_j = \vec{M}_j - n_j m_j \nu_{dj} \vec{v}_j \quad (23)$$

represents "external" momentum exchange of particles of species j due to momentum input from collisions with fast ions from neutral beam injection, \vec{M}_j , and due to the "radial" transfer of momentum across the flux surface due to anomalous viscous effects, as suggested by experiment [7, 10], which is represented by a drag frequency, ν_{dj} . The neoclassical viscous forces are contained in the term $\nabla \cdot \vec{\pi}_j$.

In these equations: n , m , e , and \vec{v} refer to the particle density, mass, charge and flow velocity of particle species j ; p is the pressure and τ is the anisotropic stress tensor discussed in the previous section; ϕ is the electrostatic potential; \vec{B} is the magnetic field; ν_{jk} is the collision frequency between particle species j and k .

Equation (19) and the perpendicular (in the flux surface) component of Eq. (20) for each species can be solved, to within a constant of integration (which is proportional to the poloidal flow velocity), for the lowest order (in the gyroradius) particle flows, which lie in the flux surface. The equation obtained by summing over species the flux surface averaged toroidal component of Eq. (20) can then be solved for the "radial" electric field. The constants of integration mentioned previously can be found by solving simultaneously the flux surface averaged parallel components of Eq. (20) for all species. The "poloidal" variation of the particle densities and electrostatic potential can then be obtained by solving the parallel (to B) components of Eqs. (20), subject to the constraint of Eq. (21). Finally, the transport flux of particles across the flux surface can be obtained by combining the parallel and normal (to the flux surface) components of Eq. (20).

At this point, we specialize our results to a plasma constituted of a main ion species (i), impurity species (I) and electrons (e), in which ion-impurity collisions are dominant over ion-electron or impurity-electron collisions in determining the transport of ions and impurities $(\alpha \equiv n_I z^2 / n_i \gg \sqrt{\frac{m_e}{m_i}})$. Actually,

$\alpha \gg \sqrt{\frac{m_e}{m_i}}$ is only a limit on the regime of validity for the theory for the main ion species. The theory is valid for the impurity species down to trace impurity concentrations ($\alpha \rightarrow 0$). For the plasma equilibrium, we make the large-aspect ratio, circular- ψ , low-beta approximation. We use the subscripts \parallel and \perp to refer to toroidal and poloidal components, and use the superscript \circ to denote the component that is uniform over the flux surface. A number of parameters which arise in the derivation are now defined:

$$P'_j \equiv \frac{1}{n_j^{\circ} e_j B_{\perp}^{\circ}}, \quad \beta_{j*} \equiv \frac{v_{jj}^{qR} c}{\epsilon^{3/2} v_{thj}}, \quad v_{thj} \equiv \frac{T_j}{m_j}, \quad j = i, I;$$

the normalized drag frequencies are

$$\beta_i \equiv \frac{v_{di}}{v_{iI}}, \quad \beta_I \equiv \frac{v_{dI}}{v_{Ii}}.$$

(where $n_i m_i v_{iI} = n_I m_I v_{Ii}$ from momentum conservation).

The normalized viscosities are

$$\hat{\mu}_j \equiv \frac{\frac{3}{2} \sqrt{\epsilon} f_{j,h}}{(1+\nu_{*j})(1+\epsilon^{3/2}\nu_{*j})} \quad j=i,I;$$

where

$$f_i \equiv \sqrt{2}/\alpha, \quad f_I \equiv \alpha \sqrt{\frac{m_I}{2m_i}}, \quad \ell \equiv \frac{m_I}{zm_i}, \quad \alpha \equiv \frac{n_i^o z^2}{n_i^o}$$

$$h_i \equiv 1 + \frac{\alpha(1-\ell)}{1+\alpha} \left(\frac{v_{\phi i}}{v_{thi}} \right)^2, \quad h_I \equiv 1 + \frac{(\ell-1)}{\ell(1+\alpha)} \left(\frac{v_{\phi I}}{v_{thI}} \right)^2$$

and

$$\xi_j \equiv \hat{\mu}_j + \beta_j,$$

$$M_{xj} \equiv \hat{n}_x \cdot \int d^3v \bar{v} m_j C_{bj}, \quad j = i,I. \quad (24)$$

In the above definitions R_o is the major radius, $\epsilon=r/R_o$ is the inverse aspect ratio, T is the temperature, q is the safety factor, ν_{jj} is the self collision frequency, C_{bj} is the Fokker-Planck collision operator, and \hat{n}_x is the unit vector in the x-direction (e.g. parallel, toroidal). Throughout the paper, the caret notation will signify either a unit vector or the normalization

$$\hat{A}_i \equiv \frac{A_i}{n_j^o m_j v_{iI}^o}, \quad \hat{A}_I \equiv \frac{A_I}{n_I^o m_I v_{II}^o}.$$

Radial Electric Field

The component of the radial electric field (E_r) which is constant over the flux surface is obtained self-consistently from the flux surface averaged toroidal momentum balance equations summed over species.

$$\frac{E_r^o}{B_o^o} = \left[\left\{ \hat{\mu}_i + \hat{\mu}_I(1+\xi_i) \right\} \hat{M}_{\phi i}^o + \left\{ \hat{\mu}_I + \hat{\mu}_i(1+\xi_I) \right\} \hat{M}_{\phi I}^o + \left\{ \beta_i + \beta_I(1+\xi_i) \right\} \hat{U}_I P'_I \right. \\ \left. + \left\{ \beta_I + \beta_i(1+\xi_I) \right\} \hat{U}_i P'_i \right] \left[\hat{\mu}_i \left\{ \beta_I + \beta_i(1+\xi_I) \right\} + \hat{\mu}_I \left\{ \beta_i + \beta_I(1+\xi_i) \right\} \right]^{-1} \quad (25)$$

Examination of this expression reveals several points. The radial electric field scales as $E_r \sim \hat{M}/\beta \sim M/v_d$, the ratio of the NBI momentum input to the radial momentum transport, or "drag", frequency and is relatively insensitive to the parallel neoclassical viscosity coefficients, $\hat{\mu}_j$. Coinjected NBI ($M > 0$) contributes a positive component to the radial electric field ($E_r > 0$), and conversely for counter-injection. The normal negative main ion pressure gradient ($P'_i < 0$) produces a negative contribution ($\Delta E_r < 0$) to the radial electric field, and similarly for the impurity pressure gradient, although the latter is usually unimportant because $|P'_I| \approx \frac{1}{z} |P'_i| \ll |P'_i|$.

Transport Fluxes

The parallel and normal (radial) components of Eq. (20) can be combined to obtain an expression for particle transport across flux surfaces

$$\langle \nabla\psi \cdot n_j \vec{v}_j \rangle = - \frac{\langle R^2 \nabla\phi \cdot (\vec{R}_j + \vec{N}_j) \rangle}{e_j}.$$

Our previous results for the rotation velocities may be used to evaluate this expression for the large-aspect ratio, low-beta equilibrium. It is important to retain $O(\epsilon^2)$ terms that were neglected in writing Eqs. (26) and (28). (These terms are given in Ref [4].) We write the radial impurity flux as a sum of contributions arising from different effects

$$\begin{aligned} \langle n_I v_{Ir} \rangle &= \langle n_I v_{Ir} \rangle_{PS} + \langle n_I v_{Ir} \rangle_{NC} + \langle n_I v_{Ir} \rangle_M + \langle n_I v_{Ir} \rangle_I \\ &+ \langle n_I v_{Ir} \rangle_{\phi'} + \langle n_I v_{Ir} \rangle_{\tilde{\phi}}. \end{aligned} \quad (37)$$

The first two components correspond to the Pfirsch-Schluter and neoclassical fluxes of the usual transport theory, but now modified to account for the radial transfer of momentum and for the variation of the impurity and ion densities over the flux surface.

$$\langle n_I^v v_{Ir} \rangle_{PS} = \frac{n_I^o m_I v_{Ii}^o \varepsilon^2}{e_I B_p^o} \left[\left\{ \left(\frac{1+2q^2}{q^2} \right) + \left(\frac{n_i^c}{\varepsilon} \right) \right\} P'_i - \left\{ \left(\frac{1+2q^2}{q^2} \right) + \left(\frac{n_I^c}{\varepsilon} \right) \right\} (1+\beta_I) P'_I \right] \quad (38)$$

and

$$\begin{aligned} \langle n_I^v v_{Ir} \rangle_{NC} = \frac{n_I^o m_I v_{Ii}^o}{e_I B_p^o} & \left[\left\{ \hat{\omega}_i \hat{\mu}_I + \varepsilon^2 \hat{\mu}_i \left((1+\beta_I) \left(\frac{n_I^c}{\varepsilon} \right) - \left(\frac{n_i^c}{\varepsilon} \right) \right) \right\} P'_i \right. \\ & \left. - \left\{ \hat{\mu}_I (\xi_i + \beta_I (1+\xi_i)) + \varepsilon^2 \hat{\mu}_I \left(\left(\frac{n_i^c}{\varepsilon} \right) - \left(\frac{n_I^c}{\varepsilon} \right) \right) \right\} P'_I \right] \quad (39) \end{aligned}$$

where

$$d \equiv \xi_i + \xi_I (1 + \xi_i) , \quad (40)$$

For a negative main ion density gradient ($P'_i < 0$), both of these flux components will be inward.

The third term in Eq. (37) is the transport flux resulting directly from the interaction of the beam ions with the main ions and impurities.

$$\begin{aligned} \langle n_I^v v_{Ir} \rangle_M = \frac{-1}{e_I B_p^o} & \left[\hat{n}_{\phi I}^o \left\{ \hat{\mu}_I (1+\xi_i) + \varepsilon^2 \left(d + (1+d) \left(\frac{n_I^c}{\varepsilon} \right) - (1+\xi_i) \left(\frac{n_i^c}{\varepsilon} \right) \right) \right\} \right. \\ & \left. + \hat{M}_{\phi i}^o \left\{ \hat{\mu}_I + \varepsilon^2 \left(\left(1 + \frac{1}{2} (\beta_I + \xi_I) \right) \left(\frac{n_I^c}{\varepsilon} \right) - \left(\frac{n_i^c}{\varepsilon} \right) \right) \right\} \right] . \quad (41) \end{aligned}$$

This contribution to the impurity flux is inward for coinjection and outward counter-injection.

The fourth term in Eq. (37) results from retention of the inertial term ($nm(\vec{v} \cdot \nabla)\vec{v}$) in the momentum balance equations, which produces $O(\varepsilon^2)$ contributions to the expressions for the toroidal and poloidal rotation velocities which in turn contribute $O(\varepsilon^2)$ terms in the transport flux. ✓

$$\langle n_I v_{Ir} \rangle_I \equiv - \frac{n_I^o m_I v_{Ii}^o \epsilon^2 B_\phi^o}{e_I B_p^o (B^o)^2 d} \left[(\xi_i + \beta_I (1 + \xi_i)) \langle \hat{G}_I \rangle - \hat{\mu}_I \langle \hat{G}_i \rangle \right], \quad (42)$$

where

$$\langle \hat{G}_I \rangle \equiv \frac{1}{2} \left(\frac{B_\phi^o}{q R_o v_{Ii}^o} \right) \left[\left[\left(\frac{B_\phi^o}{B_p^o} v_{Ip}^o \right)^2 + \omega^2 + 2 \delta_1 \omega \right] \left(\frac{n_I^s}{\epsilon} \right) + \left\{ 2 \delta_2 \omega \right\} \left(\frac{n_i^s}{\epsilon} \right) \right] \quad (43)$$

The quantities δ_1 and δ_2 involve radial density gradients and are defined in the appendix. The expression for $\langle \hat{G}_I \rangle$ is obtained from Eq. (43) by exchanging i and I subscripts, including in the definition of ω , and exchanging δ_1 and δ_2 . The quantity δ_1 is of order α/z and may be neglected in most cases. Note that $\langle \hat{G}_I \rangle$ depends (directly and indirectly through n_I^s) on the radial electric field, so that the inertial flux is actually due in large part to the radial electric field. This inertial effect will produce an outward impurity flux when the impurity density is shifted down ($n_I^s < 0$), which occurs for strong co-injection. Conversely, strong counter-injection will produce an inward flux contribution via this inertial effect.

The fifth term in Eq. (37) is the radial impurity flux driven by the linear component of the radial electric field.

$$\langle n_I v_{Ir} \rangle_{\phi'} = \frac{n_I^o m_I v_{Ii}^o}{e_I B_p^o} \left[\hat{\mu}_I \gamma_I + \epsilon^2 \left\{ \beta_i \left(\frac{i + 2q^2}{q^2} \right) + (\beta_I + \gamma_I \left(\frac{n_I^c}{\epsilon} \right) - \gamma_I \left(\frac{n_i^c}{\epsilon} \right)) \right\} \right] \left(\frac{E_r^o}{B_p^o} \right) \quad (44)$$

where

$$\gamma_I \equiv \frac{\beta_i + \beta_I (1 + \xi_i)}{\xi_i + \xi_I (1 + \xi_i)}.$$

This term will have the same sign as the radial electric field. Thus, it will produce an outward contribution to the impurity flux for strong co-injection and an inward contribution for counter-injection and weak coinjection (assuming $P_i' < 0$).

The last term in Eq. (37) is the impurity transport flux driven by the poloidal variation of the potential over the flux surface, or the poloidal electric field. This term is of order α/z and usually may be neglected.

The main ion transport flux may be obtained by exchanging i and I subscripts in the above equations. In addition, in Eq. (45) δ_1 and δ_2 must be exchanged, $a/z \rightarrow z/a$, and $z \rightarrow -z$.

Note that Eqs. (38) and (39) describe diffusive transport fluxes - i.e. fluxes proportional to a pressure gradient-while Eqs. (41), (42), (44) and (45) describe convective transport fluxes arising from viscous and inertial forces and the direct momentum input. The diffusive impurity fluxes are inward for the normal negative main ion density gradient. The rotational and electric field contributions to the convective flux are outward for strong co-injection and inward for counter-injection, and conversely for the direct momentum input contribution of Eq. (41).

IV. MODEL PROBLEMS

In order to illustrate the nature of the theoretical results that were developed in the previous two sections, we now apply the formalism to two model problems with deuterium plasmas representative of the interior regions of the ISX-B and PLT tokamaks. Neutral beam injection at 40KeV was considered in both cases. In both of these machines the toroidal rotation velocity with directed NBI has been measured [7,10], which allows us partially to extract the anomalous viscous drag frequencies ν_{di} and ν_{dI} from experimental data. The procedure we follow is first to calculate the ratio β_I / β_i from Eq. (33) (with $K=1$) and then to determine β_i from the summed toroidal momentum balance, which may be rearranged to obtain

$$\beta_i \approx \frac{M_\phi}{n_i m_i \nu_{di} \nu_{dI} \phi (1 + 3_I / 3_i)}, \quad (46)$$

where M_ϕ is the total toroidal momentum input of the beam and ν_{dI} is the measured rotation velocity. Usually, only one rotation velocity, that of an impurity species, is measured. For our purposes here, we take that approximately as a common rotation velocity for all species. If the rotation velocities of both the ions and impurities are measured, then Eqs. (30) and (31) can be used to determine ν_{di} and ν_{dI} separately.

We examined a deuterium plasma with a titanium impurity with $\alpha = 0.05$ in ISX-B. We chose parameters typical of an ISX plasma at $r \approx 10$ cm ($n_e = 2.8 \times 10^{13} / \text{cm}^3$, $T_e = T_i = 430$ eV, $q = 1.2 \left(\frac{1}{p} \frac{\partial p}{\partial r} \right)^{-1} = -8.5 \text{cm}$) and computed the toroidal momentum input of the H^0 beam with a beam deposition and Fokker-Planck slowing down code. For this ISX plasma, the beam momentum input was mostly to the deuterium $|\hat{M}_i| \gg |\hat{M}_I|$. The deuterium was in the banana-plateau regime with viscosity $\hat{\nu}_i \sim 0(\sqrt{\epsilon})$ and the titanium was in the collisional regime with $\hat{\nu}_I \leq 0(\epsilon^2)$. The anomalous drag coefficients computed in the manner described above led to the ratio $\beta_I / \beta_i = 0.36$, using the toroidal rotation velocities measured at 1 MW co-injection.

As a second model problem, we choose a deuterium plasma with parameters representative of PLT at $r = 10-20$ cm: $[n_i = 3 \times 10^{13} \text{ cm}^{-3}, T_i = T_e = 1 \text{ keV}, q = 1.5, \left(\frac{1}{v_i} \frac{\partial p_i}{\partial r}\right)^{-1} = -30 \text{ cm}]$. We used the previously described procedure and the experimentally determined [1] rotation velocities to determine the values $v_{di} = 34 / \text{s}$, $v_{dI} = 5100 / \text{s}$ and $\beta_I / \beta_i = 1.5$. We considered a uniform tungsten impurity of concentration $\alpha = 0.1$ and injection of a 40 keV D^0 beam, with the momentum input calculated as described for the first model problem. The deuterium ions are in the banana-plateau regime and the tungsten ions are in the collisional regime ($\mu_I \rightarrow 0$).

Our results for the PLT model problem are shown in Figs. 3, 4. The qualitative character of the results is similar to the ISX results, although the quantitative results are quite different between the two cases. We note that the toroidal rotation velocity is larger in PLT than in ISX, for a given directed beam power, although the total number of plasma particles is greater in PLT, implying a stronger radial momentum transfer mechanism operating in ISX than in the much larger PLT.

We note that in the PLT model problem with no injection the inward impurity flux due to the radial electric field (the linear contribution of Eq. (44) plus the nonlinear, inertial contribution of Eq. (42)) is the same size as the inward contribution due to the pressure gradient of Eqs. (38) and (30). Thus, the total inward impurity flux is about twice the neoclassical value, and conversely the outward deuterium flux is also about twice the neoclassical value, which is reminiscent of the observation that the measured ion heat conductivity is about 2-4 times the neoclassical value. Possibly, the radial electric field effects of the present theory can account for this well-known "factor of 2-4" disparity between neoclassical predictions and experiment.

The total tungsten fluxes in Fig. 4 are in reasonable agreement with those measured in PLT [5]. The experimental fluxes at $10 \leq r \leq 20$ cm were $\sim 6-7 \times 10^{15} / \text{m}^2 \text{-s}$ inward without NBI, $\sim 2-4 \times 10^{15} / \text{m}^2 \text{-s}$ outward with 585 kW coinjection, and $\sim 25-50 \times 10^{15} / \text{m}^2$ inward with 430 kW counter-injection. The total calculated tungsten fluxes shown in Fig. 6 are $\sim 9 \times 10^{15} / \text{m}^2 \text{-s}$ inward without NBI, $\sim 4 \times 10^{15} / \text{m}^2 \text{-s}$ outward with 585 kW coinjection, and $\sim 50 \times 10^{15} / \text{m}^2 \text{-s}$ inward with 430 kW counterinjection.

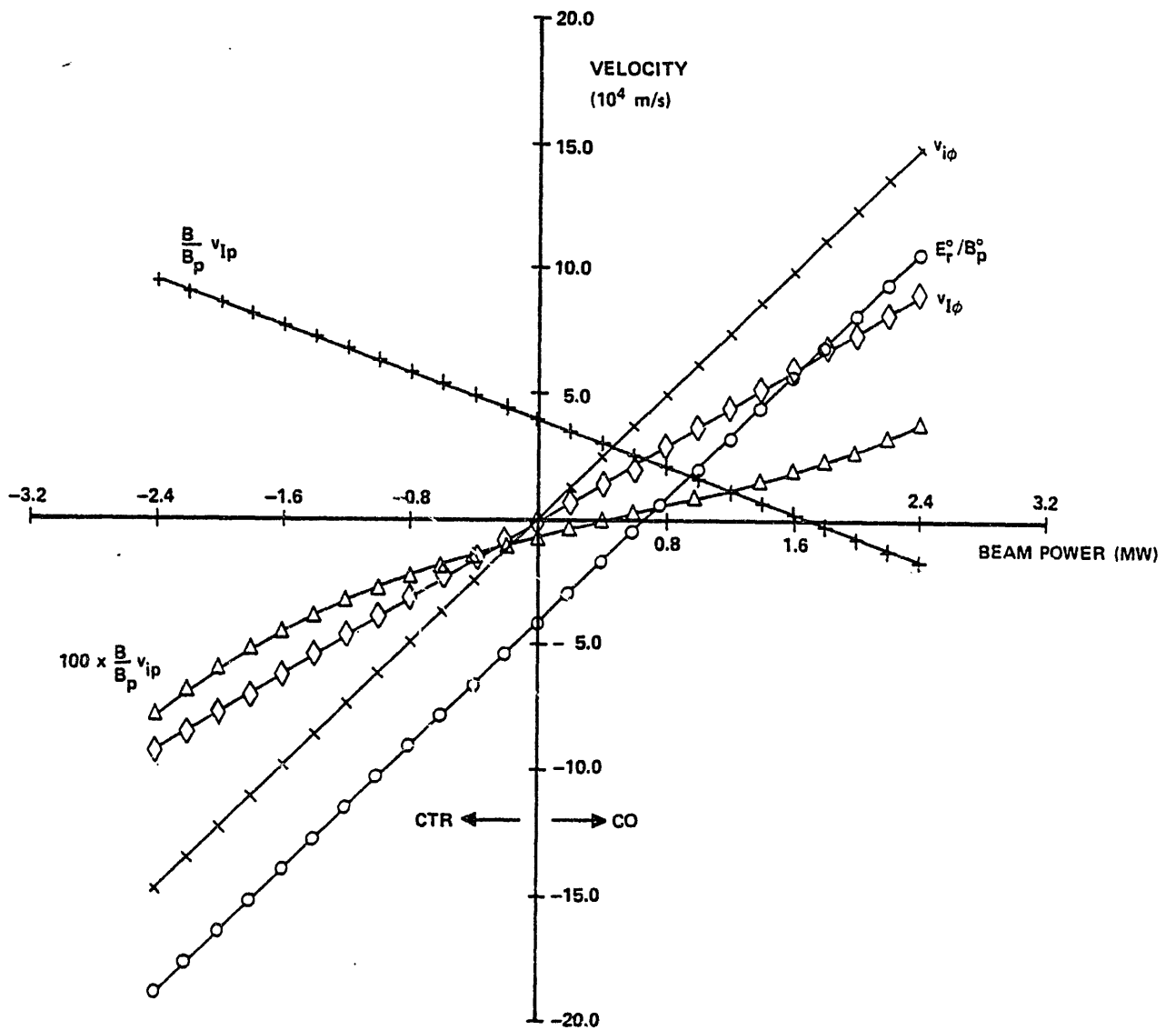


Fig. 1
Rotation Velocities and Radial Electric Field in ISX-B Model Problem

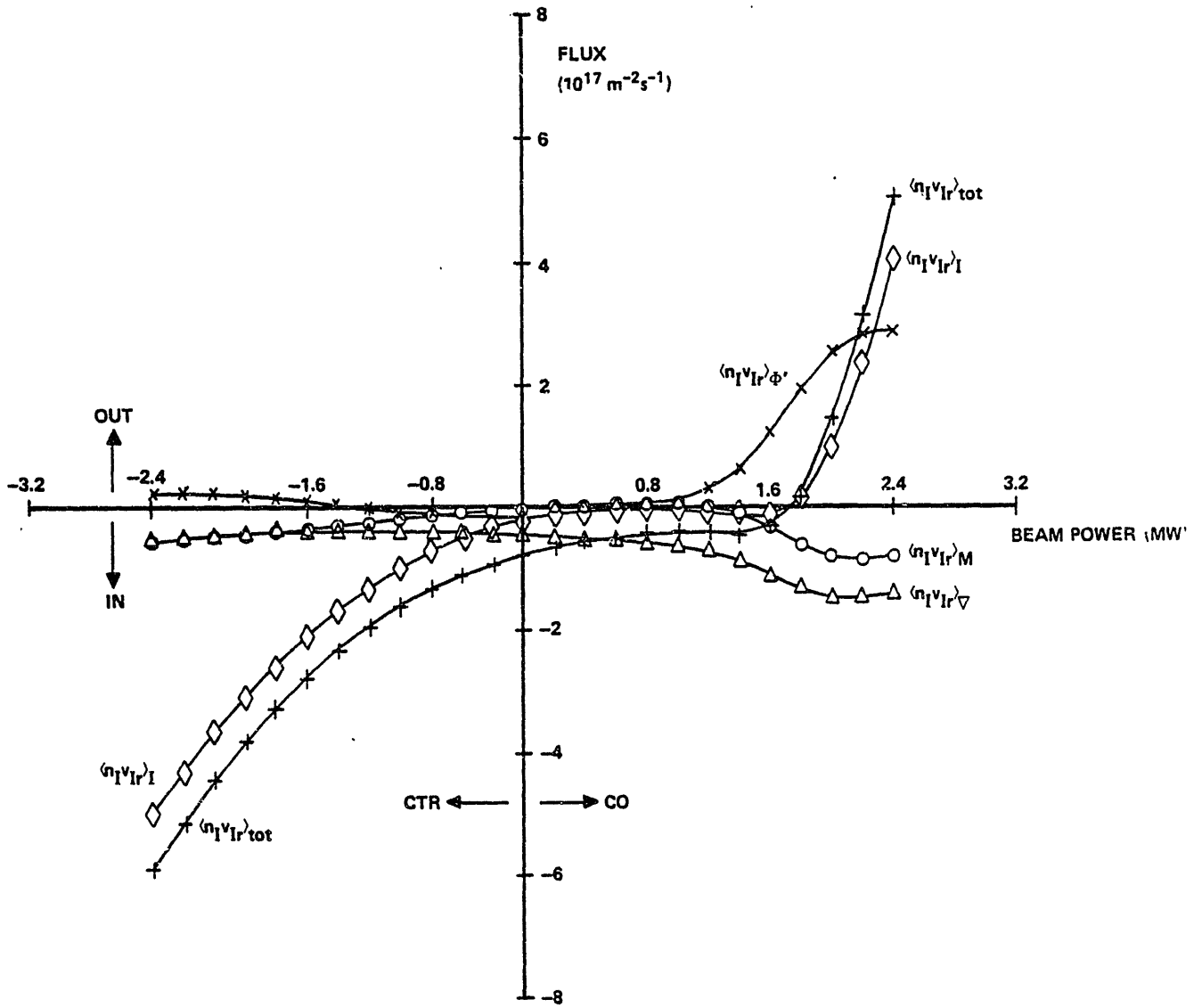


Fig. 2
 Impurity Transport Fluxes in ISX-B Model Problem

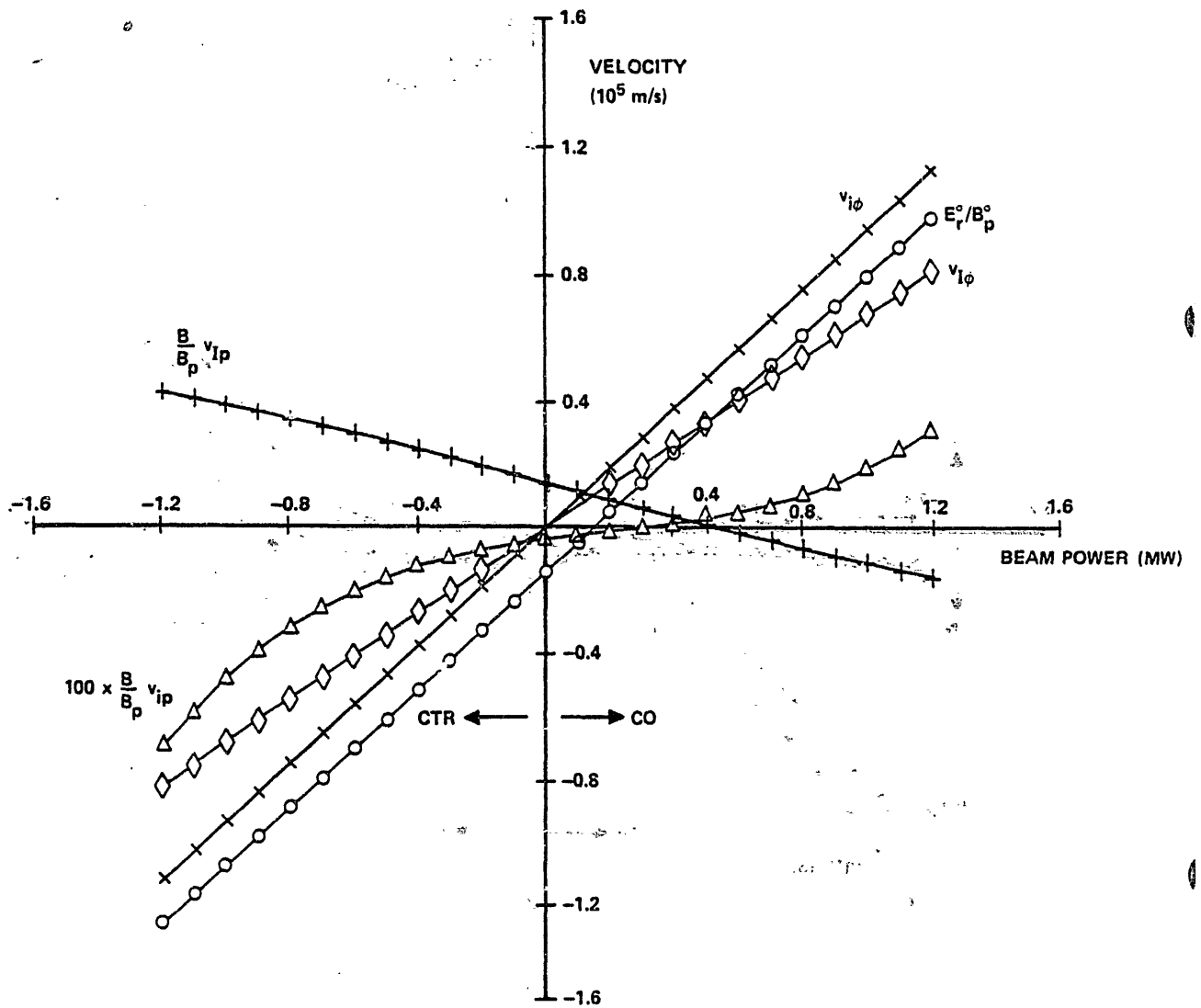


Fig. 3
Rotation Velocities and Radial Electric Field in PLT Model Problem

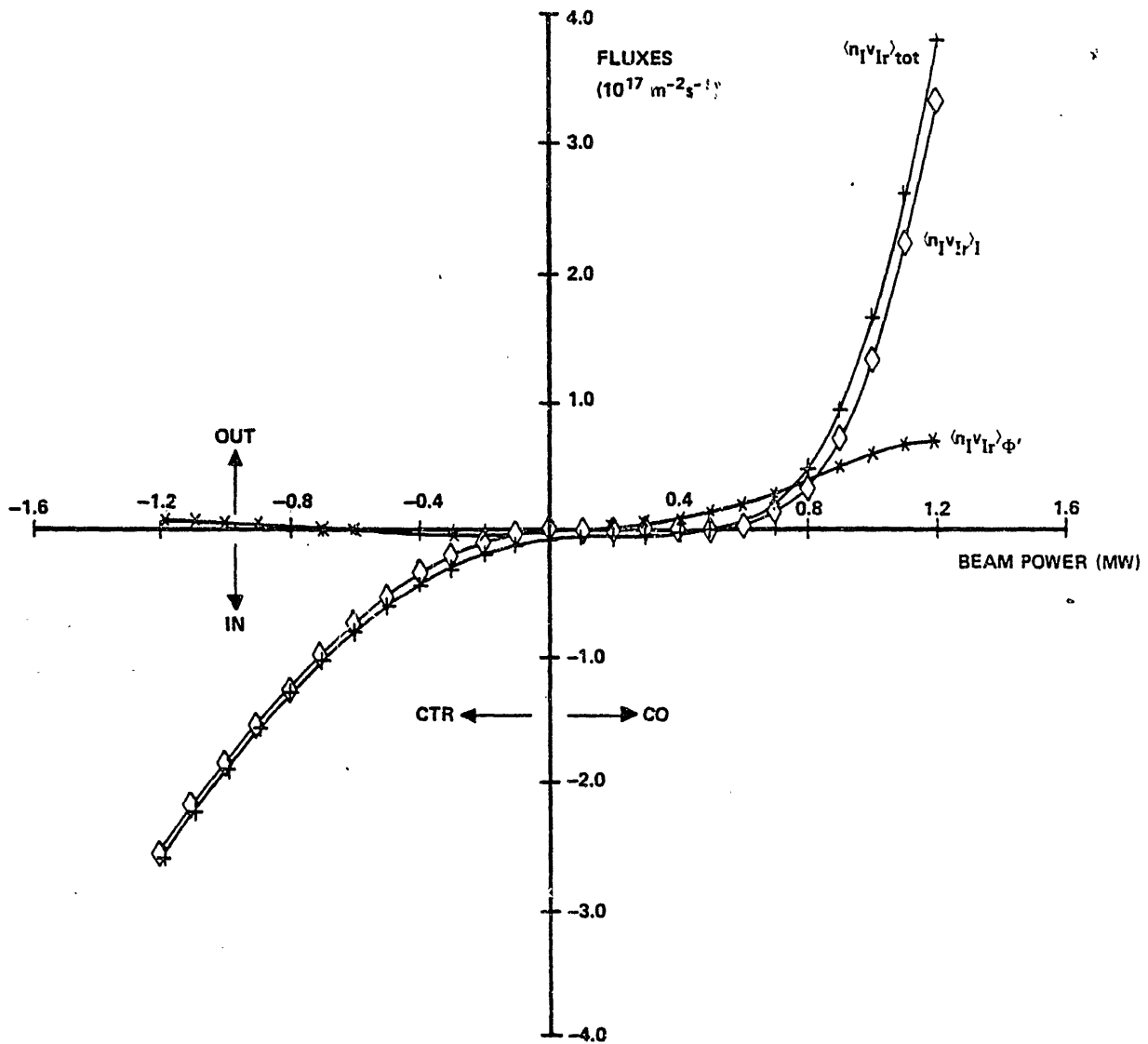


Fig. 4
Impurity Transport Fluxes in PLT Model Problem

BOUNDARY CONDITIONS FOR H-MODE*

GA Technologies D-III Groups

Presented by
N. OHYABU

GA Technologies Inc.
P. O. Box 85608, San Diego, CA 92138

Neutral-beam-heated expanded-boundary (XB) divertor discharges (Fig. 1) have been obtained in Doublet III with high heating efficiency for wide ranges of plasma parameters (I_p : 300 – 800 kA; B_T : 8 – 24 kG; \bar{n}_e 2 – $10 \times 10^{13} \text{cm}^{-3}$; $P_{beam} < 4.5 \text{ MW}$, $\beta_p \leq 1.6$, and $\beta_t \leq 2.8\%$). The improved heating efficiency is well correlated with a configurational change from limiter to XB discharges (Fig. 2). The beam-heated, fully diverted expanded-boundary discharges with a limiter-separatrix distance greater than 1.5 cm exhibit up to a factor of two improvement in energy confinement time (Fig. 3). The τ_E increases approximately linearly with I_p , but is insensitive to variations of a factor of two in \bar{n}_e and B_T . Over the inner two-thirds of the plasma radius ($r/a \leq 0.7$), the shape of the T_e profile for XB discharges is similar to that for limiter discharges (Fig. 4). Hence the improvement of the global energy confinement is consistent with a reduction of thermal conductivity over most of the plasma radius. With 2 MW of neutral-beam injection into a high-current ($I_p = 750 \text{ kA}$) XB discharge, we have obtained energy confinement times $\bar{n}_e \tau_E \approx 1 \times 10^{13} \text{cm}^{-3} \text{s}^{-1}$. At high beam power ($P_b > 3 \text{ MW}$), a mild deterioration of the energy confinement time has been observed.

*Work Supported by U. S. DOE Contract DE-AT03-84ER51044.

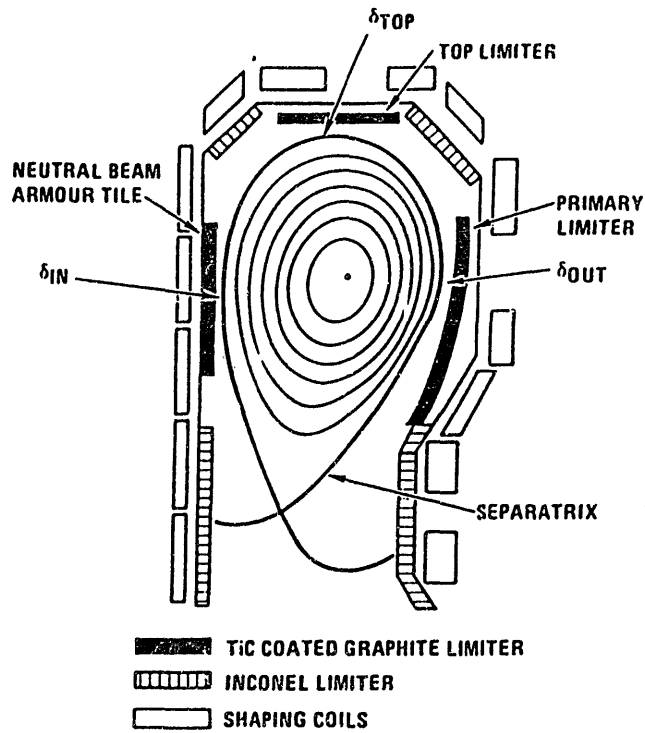


FIG. 1 Equilibrium flux surface plot for a typical expanded boundary divertor configuration illustrating the relationship between the separatrix and the various limiters in Doublet III. The distance between the separatrix and the leading edge of the nearest limiter, Δ , is the minimum value of the distance between the limiter and the separatrix for each of the 3 limiters (δ_{in} , δ_{top} , δ_{out}) as shown.

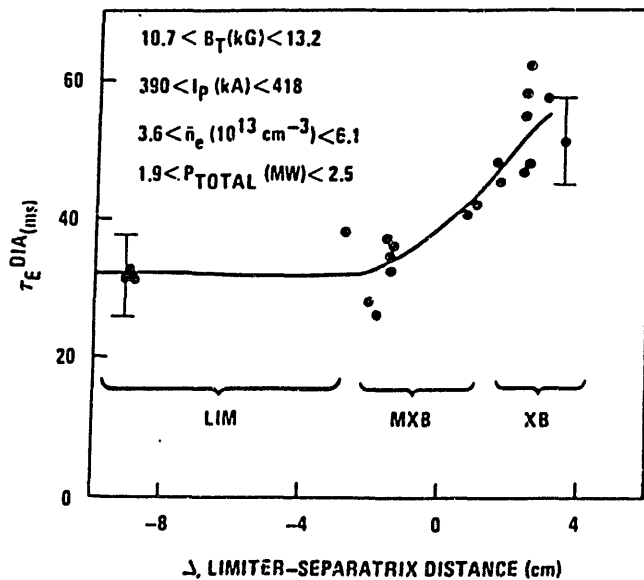


FIG. 2 Variation of τ_E from diamagnetic loop measurements with Δ , limiter-separatrix distance, for fixed parameters, illustrating 3 types of discharges.

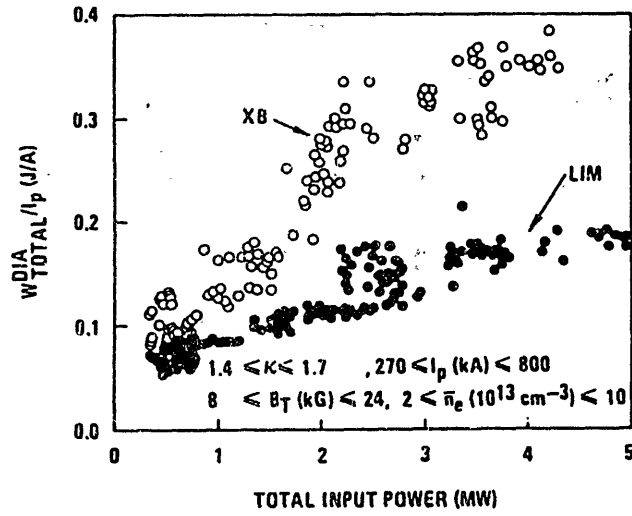


FIG. 3 Variation of W_{total}/I_p with total input power for limiter ($\Delta < -4$ cm) and XB ($\Delta > 1.5$ cm) discharges.

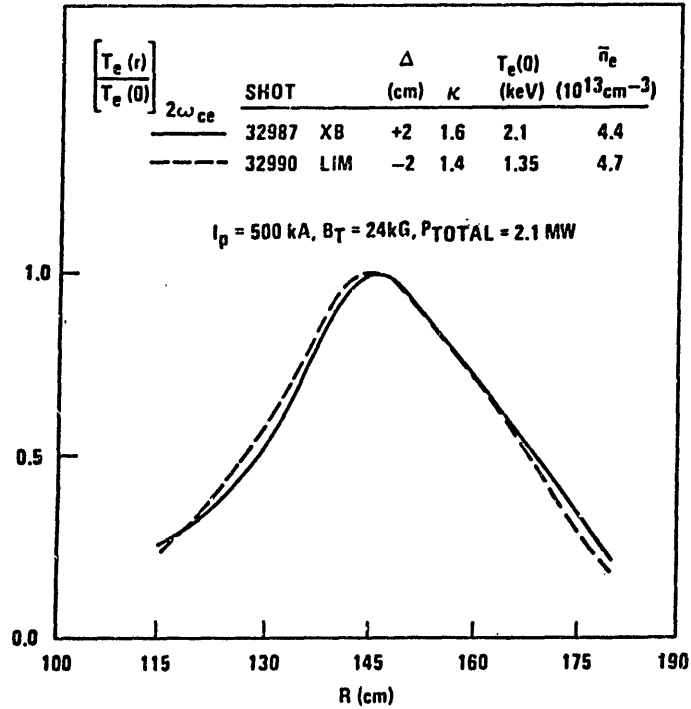


FIG. 4 Comparison of T_e profile obtained from electron cyclotron emission at $2\omega_{ce}$ between comparable XB and limiter discharges.

SIMULATION OF IMPURITY TRANSPORT IN H-MODE TOKAMAK DISCHARGE

T. HIRAYAMA

Japan Atomic Energy Research Institute, Japan

Abstract

Results of the impurity injection experiments in Doublet III beam heated plasmas were analysed with a numerical code to determine the transport properties of trace impurities in L- and H-mode. A numerical code simulating the impurity transport is utilized to estimate the value of anomalous diffusion coefficient D_A . The impurity flux density is expressed as the sum of an Alcator-INTOR type anomalous diffusion (D_A) and the neoclassical flux. The D_A of $(4-5) \times 10^{19}/n_e$ (m^2/s) can well explain the dependence of the experimental decay time on electron density. No difference in D_A was found between L- and H-mode discharges as well as the joule heating phase.

1. Introduction

The discovery of good confinement discharges by ASDEX [1], where the divertor equilibrium improves the energy confinement time of the beam heated plasmas by a factor of two, was a highly encouraging result in the research and development of the tokamak reactor. These good confinement discharges are referred to as "H-mode" in comparison to the deteriorated confinement discharges in the so-called "L-mode". Similar H-mode discharges have also been obtained in Doublet III [2] and PDX [3]. The experimental data indicated the importance of particle transport properties as well as the electron thermal conductivity [4]. However, it is not possible to measure the particle confinement time directly. And therefore, titanium impurity injection experiments were performed in Doublet III in order to study the impurity transport. The decay times of line emissivity of Ti XX (259.3 Å) are measured and show a weak dependence on the electron density throughout the neutral beam heated discharges. The injected titanium ion line emissions are simulated with a numerical code using Alcator-INTOR [5] type anomalous diffusion coefficients and a neoclassical flux in the flux density expression.

2. Experimental results

In Doublet III, 69-76 kV hydrogen beam with power of up to 4 MW is injected near-perpendicularly into a deuterium plasma. The discharges are made with either a divertor configuration or a poloidal limiter configuration, whose cross-section shapes are shown in Fig. 1. In the divertor configuration, high-confinement discharges (H-mode) have been obtained with neutral beam injection heating.

A small amount of titanium is injected into the steady state portion of the discharge at 0.8 sec from the breakdown, using a laser blow-off technique [6]. The emission of Ti XX along a horizontal chord is measured at ~8 cm vertically above the magnetic axis. Decay times are obtained from the e-folding time of a decaying chordal line radiance of Ti XX in the L-mode and

H-mode discharges as well as in the joule heating phase. A parameter study of impurity injections has been performed with various combinations of parameters: plasma current ($300 \text{ kA} < I_p < 750 \text{ kA}$), electron density ($2.5 \times 10^{19} \text{ m}^{-3} < \bar{n}_e < 7.5 \times 10^{19} \text{ m}^{-3}$, where \bar{n}_e means the electron density averaged along a tangential chord (CH-B) at $r/a = 0.33$), and the toroidal magnetic field ($B_t \sim 2.4\text{T}$). The time evolution of the Ti XX emission in the H-mode is shown in Fig. 2-(e). Other plasma parameters are also shown in figures: (a) neutral beam pulses; (b) electron density at $r/a = 0.33$; (c) poloidal beta β_p from the diamagnetic loop measurement; (d) H_α/D_α line emissions at the divertor plate and at the middle of the main plasma.

All data of the decay time τ_d measured in the experiment are shown in Fig. 3 versus line-averaged electron density of CH-B. In this figure, the notation "D" means a dee-shaped discharge with a limiter as shown in Fig. 1-b. The open symbols corresponds to the decay times in the H-mode discharges and the solid to the L-mode discharges. The squares show the data in the joule phase. This figure shows a weak dependence of τ_d on the electron density. Figure 4 shows the data points with shot numbers, which are analyzed in this paper. The heating efficiency which is the increment of β_p divided by the number of neutral beams ($\sim 1\text{MW}/\text{beam}$) is plotted against the inversed square of the plasma current and also shows the definition of the H-mode and L-mode used in this paper. The heating efficiency data in Doublet III are almost uniformly distributed between the two lines H and L. We refer to data points above the middle dotted line between the L and H lines as H-mode and to others as L-mode. The notation "AX" in this figure corresponds to the ASDEX data just for comparison [1].

3. Simulation Procedure

A one-dimensional time-dependent, multi-species impurity code is used to treat impurity transport and atomic processes of ionization and recombination simultaneously. The transport model is discussed in Ref. [7] ; here we only add some comments on a few modifications for simulation of impurity injection.

The simulation of impurity injection to measure the decay time is

performed by switching recycling coefficients to zero at the time $t = 0.8$ sec, after calculating the density profiles with recycling coefficients of 1.0, instead of a pulsive external source due to impurity injection. It was confirmed that this abridgement does not affect the decay times for ions higher than fourteenth for titanium impurity simulation. In order to compare the simulation results with the experimental data, a line integrated value of the line radiation Ti XX is calculated at 8 cm off the magnetic axis and the decay time is evaluated from the initial e-folding time of the decaying chordal radiance. Background plasma parameters are given by timetables of the experimental data. The background ion is assumed to be deuterium and its temperature is approximated by the electron temperature. The assumption of a circular cross section is used throughout this simulation. The effects of sawtooth oscillation and momentum transfer due to neutral beam injection have been ignored.

The rate coefficients are calculated from the multi-ion model [8] that is reformulated from the average ion model [9]. The charge-transfer (CT) recombination with H/D neutrals is also considered as well as the electron impact. The CT recombination rates are based on the empirical formulation of IPPJ [10]. Only the fast neutrals of the injected neutral beam and the halo neutrals are assumed to have the charge-transfer interaction with impurity ions except for the thermal neutrals of the background ions. The deposition profiles of the fast ions are calculated with a simple pencil beam model by considering the beam energy components.

4. Computational Results and Discussion

With the anomalous diffusion coefficient inversely proportional to the electron density, we have simulated the decaying radiances of the injected titanium ions. First, the tendencies of τ_d are studied with fixed plasma profiles. Secondly, the simulation calculation for the experimental data is made to obtain the value of D_A .

In using the Alcator-INTOR type diffusion coefficient, we have studied the dependence of τ_d on the plasma parameters with the plasma profiles which are normalized as follows: $T_e(r) \propto (1 - (r/a)^{1.5})^2$, $T_e(a) = 0.05T_e(0)$;

$n_e(r) \propto (1 - (r/a)^4)$, $n_e(a) = 0.1n_e(0)$. The parameter studies are made by changing the central electron temperature from 1.0 keV to 2.5 keV and the volume averaged electron density from $3 \times 10^{19} \text{ m}^{-3}$ to $9 \times 10^{19} \text{ m}^{-3}$. Figure 5 shows the calculated τ_d of Ti XX versus the averaged electron density for several central electron temperatures, with $D_A = 4 \times 10^{19}/n_e \text{ [m}^2/\text{s]}$, the plasma current of 740 kA and the toroidal field of 2.4 T. τ_d increases with the increase of the electron density, while it decreases with the increase of the central electron temperature. These are caused by the inverse dependence of D_A on the electron density and by a movement of the peak position of Ti XX toward the outer region [11]. This shows that the central electron temperature is one of the important contributing factors to τ_d .

For the experimental data shown in Fig. 4, the simulation calculation has been made to evaluate the decay times. Figure 6 shows the comparison of calculation results and experimental results of the decay times for line radiation of Ti XX versus the volume averaged electron density. The results are classified according to their central electron temperatures: (a) $T_e(0) = 0.8 \sim 1.0 \text{ keV}$ (Joule plasma); (b) $T_e(0) = 1.5 \text{ keV}$; (c) $T_e(0) = 1.9 \sim 2.5 \text{ keV}$. "D" in the figure denotes dee-shaped discharges with a limiter; the others are divertor discharges. The experimental τ_d are shown in the same symbols as those in Fig. 3. The symbols of + and x correspond to the calculated results with observed plasma profiles with $D_A = 4 \times 10^{19}/n_e \text{ [m}^2/\text{s]}$ and with $D_A = 5 \times 10^{19}/n_e \text{ [m}^2/\text{s]}$, respectively. The solid curves in these figures show the decay times that are obtained with fixed profiles of plasma parameters with $D_A = 4 \times 10^{19}/n_e \text{ [m}^2/\text{s]}$ as shown in Fig. 5. The differences between these lines and the calculated points + are caused by the difference in plasma profiles. The discrepancies are less than 20 % for all cases. This suggests that the neoclassical effects due to gradients in plasma profiles are weak in Doublet III discharges. Figure 6 shows that a good agreement in τ_d is obtained over a wide range of plasma parameters within experimental and calculational accuracies. No appreciable difference in D_A was found between three kinds of discharges, as far as using the Alcator-INTOR type anomalous diffusion coefficient. D_A of $(4-5) \times 10^{19}/n_e$ can well explain the tendency of the weak dependence of τ_d on electron density. For constant D_A over the radius, we have not obtained a systematic agreement of the decay times between the calculation results and the experimental data.

Figure 7 shows the values of $D_A=4 \times 10^{19}/n_e$ for different discharges at $t = 0.8$ sec just before zero-recycling. The values of D_A at the edge for dee-shaped discharges are smaller than the ones for diverted discharges by a factor of 3-4 because the dee-shaped discharges have a high electron density at the boundary [4]. It should be emphasized again that τ_d of not only the diverted discharges but also the dee-shaped limiter discharges agree with the calculation results obtained with D_A which is inversely proportional to the electron density as shown in Fig. 6. This fact might suggest that the decay time of Ti XX is not determined by D_A at the outer region but by D_A at the peak position in Ti XX profile. In order to verify that D_A at the edge has little effect on the calculated τ_d , calculations were made whereby the anomalous diffusion coefficient was assumed to be half of $4 \times 10^{19}/n_e$ during the neutral beam injection in two regions: (a) $0.7 < r/a < 1$ and (b) $0.5 < r/a < 1$. Figure 8 shows the impurity ion density profiles at $t=0.79$ sec for the H-mode. The calculated decay times are 31.5 ms for the case of (a) and 40.6 ms for the case of (b). The original decay time with $D_A=4 \times 10^{19}/n_e$ is 24.6 ms. It is obvious that the improved transport at the region farther out from the density profile of Ti XX would have an impact on the decay time only by a factor of 30%. On the other hand, the smaller D_A over the region including the peak position in Ti XX profile, clearly results in the too long decay time as shown in Fig. 8. Therefore, it is shown that τ_d of initial e-folding time mainly reflects the impurity transport properties near the peak position in the profiles of the measured line radiation.

5. Conclusion

By using Alcator-INTOR type scaling as D_A , we have simulated the injections of titanium over a wide range of plasma parameters, from L-mode to H-mode as well as the pulse heating phase. Analysis of the decay time of the injected impurity experiments demonstrated that the impurity transport does not change with the difference of the plasma parameters between H- and L-modes. The anomalous diffusion coefficient obtained is $(4-5) \times 10^{19}/n_e$ [m^2/s].

If there is a strong relation in the particle transport between the bulk ions and the impurity ions, the two facts that the one, no essential differences in the decay time are seen for the different discharge mode and that the second, the contribution of D_A at the outer region to the decay time is small, suggest that an improvement of confinement property in the H-mode may exist in a limited region of $r/a > 0.7$; the particle confinement is apparently improved in the H-mode relative to that in the L-mode because the electron density increases or keeps constant value even though the gas fueling is reduced. Therefore, it is reasonable that no differences in the impurity transport are seen over the wide parameter range from the L-mode to the H-mode because the peak position in Ti XX profile is located at the inner region of $r/a < 0.6$ through this experiment.

7. Acknowledgements

The authors are grateful to Dr. R. A. Hulse of the Princeton Plasma Physics Laboratory for supplying the atomic physics package code of the multi-ion model. The authors would like to express appreciation to Dr. S. K. Wong for stimulating discussions. The continuing support of Drs. S. Mori, Y. Iso, K. Tomabechi, Y. Obata, M. Yoshikawa of JAERI, and Drs. T. Ohkawa and J. Gilleland of GA Technologies, is gratefully acknowledged.

REFERENCES

- [1] WAGNER, ., BECKER, G., BEHRINGER, K., CAMPBELL, D., EBERHAGEN, A., et al., in Plasma Physics and Controlled Nuclear Fusion Research (Proc. 9th Int. Conf. Baltimore, 1982) vol1. 1. IAEA,Vienna (1983) 43.
- [2] NAGAMI, M., KASAI, M., AIKAWA, H., KITSUNEZAKI, A., et al., in Controlled Fusion and Plasma Physics (Proc. 11th European Conference, Aachen, 1983).
- [3] KAYE, M. S., BELL, M., BOL, K., BOYD, D., et al., *ibid.*
- [4] NAGAMI, M., KASAI, M., KITSUNEZAKI, A., KOBAYASHI, T., et al., *Nuc. Fus. Vol.24, 2 (1984) 183.*
- [5] INTERNATIONAL TOKAMAK REACTOR Zero Phase, Report of the International Tokamak Reactor Workshop, IAEA, Vienna (1980).
- [6] BURRELL, K. H., WONG, S., MULLER, C.H., HACKER, M.P., et al., *Nucl. Fus. Vol.21, (1981) 1009.*
- [7] HIRAYAMA, T., TAKIZUKA, T., SHIMADA, M., NAGAMI, M., et al., Numerical Transport Studies of Injected Titanium into Doublet III Beam Heated Discharges. GA-A17406, (1984).
- [8] HULSE, R.A., *Nucl. Technology/Fusion Vol.3, (1983) 259.*
- [9] POST, D.E., JENSEN, R.V., TARTER, C.B., GARISBERGER, W.H., and LOKKE, W.A., *Atomic Data Nucl. Data Table, Vol.20, (1977) 397.*
- [10] KANEKO, Y., ARIKAWA, T., ITIKAWA Y., et al., IPPJ-AM-15.
- [11] ALLEN, S.L., MOOSE, H.W., MARMAR, E.S. and RICE, L.E., *Nucl. Fus. Vol.23, (1983) 303.*

FIGURE CAPTIONS

- Fig. 1 Plasma cross section studied in the present work, (a) divertor discharge, (b) limiter discharge.
- Fig. 2 Typical time evolution of the Ti XX emission and related plasma parameters in the H-mode discharge with $I_p = 740$ kA, $P_{INJ} \sim 4$ MW and $B_t = 2.4$ T.
 (a) neutral beam pulses,
 (b) electron density (CH-B) at $r = 14$ cm,
 (c) poloidal beta for the diamagnetic loop measurement,
 (d) H_α/D_α line emissions at the divertor plate and in the middle of the main plasma,
 (e) the emission of Ti XX (259.3 Å) along a horizontal chord at ~ 8 cm vertically above the magnetic axis.
- Fig. 3 Experimental decay time τ_d vs. line-averaged electron density \bar{n}_e . The open symbols correspond to τ_d in the H-mode discharge and the solid to the L-mode discharge. The squares show the data in the joule phase. D means a dee-shaped discharge with a limiter.
- Fig. 4 Increment of beta per number of neutral beams (~ 1 MW/beam) with respect to I_p^{-2} . Two lines of H and L show the typical data in the H- and L-mode discharges. Symbols mean the same as those in Fig. 3. The AX corresponds to the ASDEX data.
- Fig. 5 Dependence of tau on the plasma parameters with the fixed profiles: $T_e(r) \propto (1-(r/a)^{1.5})^2$, $T_e(a) = 0.05T_e(0)$; $n_e(r) \propto (1-(r/a)^4)$, $n_e(a) = 0.1n_e(0)$; $D_A(r) = 4 \times 10^{19}/n_e(r)$; $I_p = 740$ kA, $B_t = 2.4$ T.
- Fig. 6 Comparison of experimental τ_d and calculated results with observed plasma profiles: +, $D_A = 4 \times 10^{19}/n_e$; x, $D_A = 5 \times 10^{19}/n_e$. The axis of the abscissa is the volume averaged electron density. The solid lines show the calculated results for fixed plasma profiles with $D_A = 4 \times 10^{19}/n_e$.

Fig. 7 Profiles of anomalous diffusion coefficient of $4 \times 10^{19}/n_e$ at $t = 0.8$ sec. The values at the radii further out than $r = 35$ cm are shown in a different scale.

Fig. 8 Titanium ion density profiles and the effect of D_A on τ_d for the H-mode discharge; $T_e(0) = 2.5$ keV, $I_p = 740$ kA, $P_{INJ} \sim 4$ MW and $B_t = 2.4$ T. The D_A is reduced by a factor of 1/2 after the neutral beam injection in two regions: (a) $0.5 < r/a < 1.0$; (b) $0.7 < r/a < 1.0$. The decay times are 40.6 ms for (a) and 31.5 ms for (b), and the original τ_d is 24.8 ms with $D_A = 4 \times 10^{19}/n_e$.

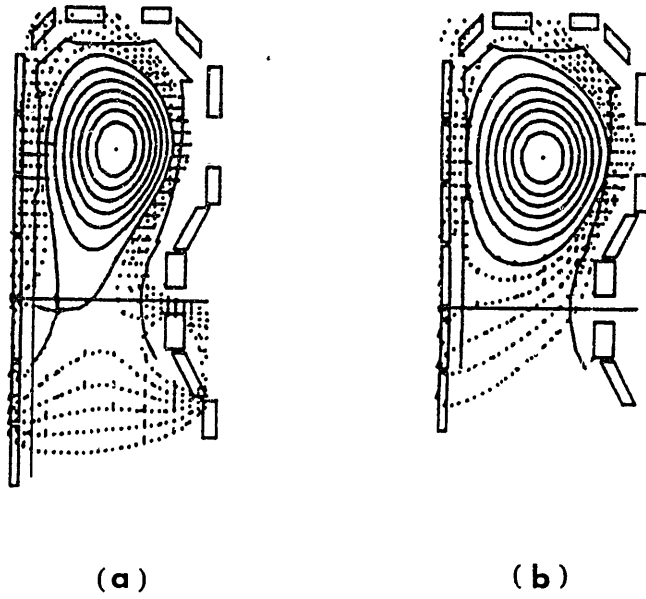


Fig. 1

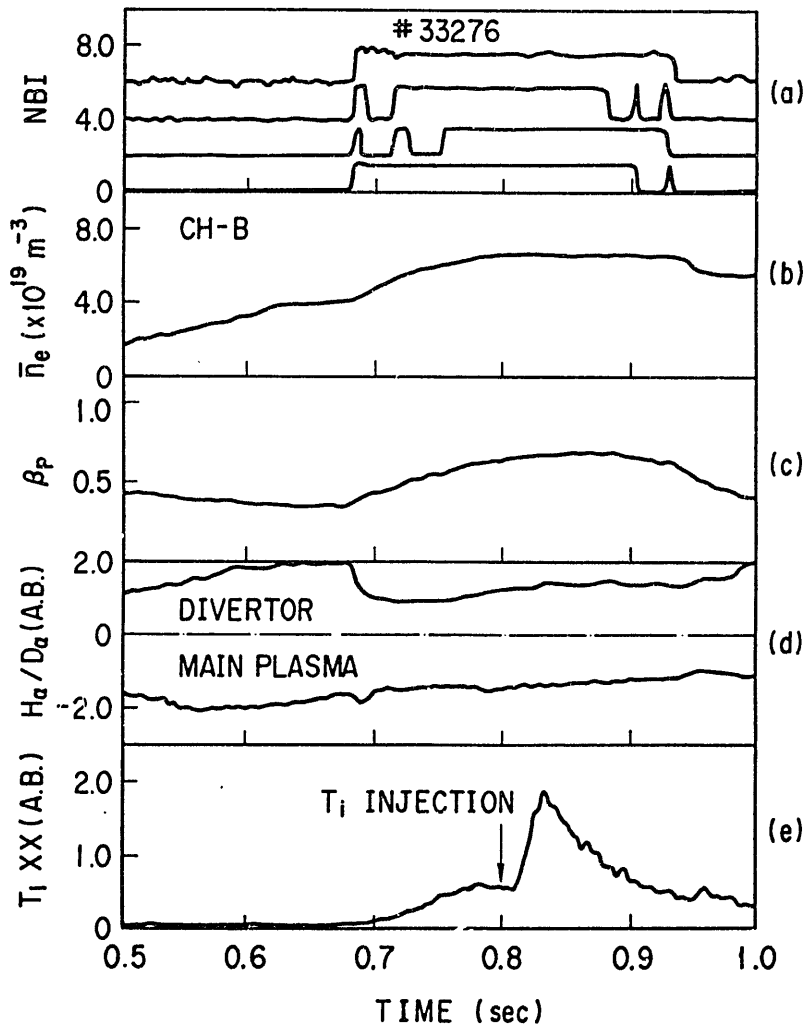


Fig. 2

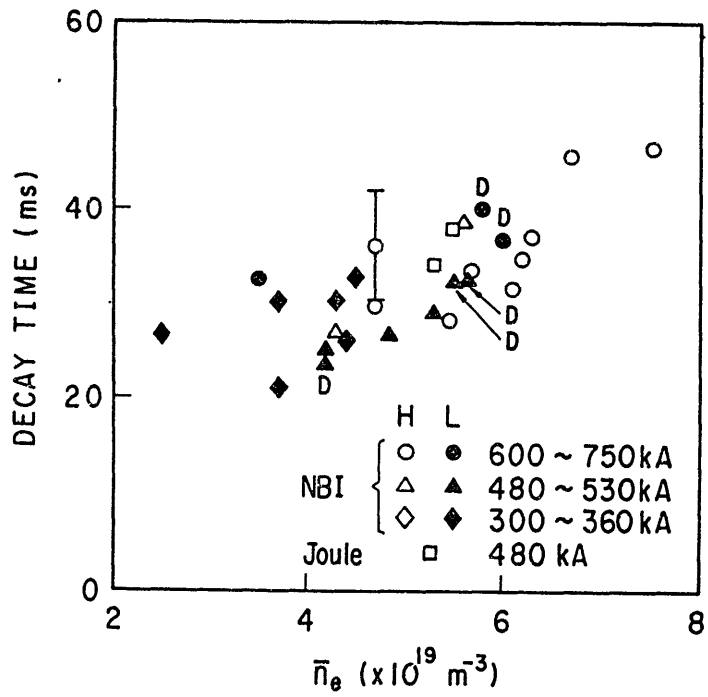


Fig. 3

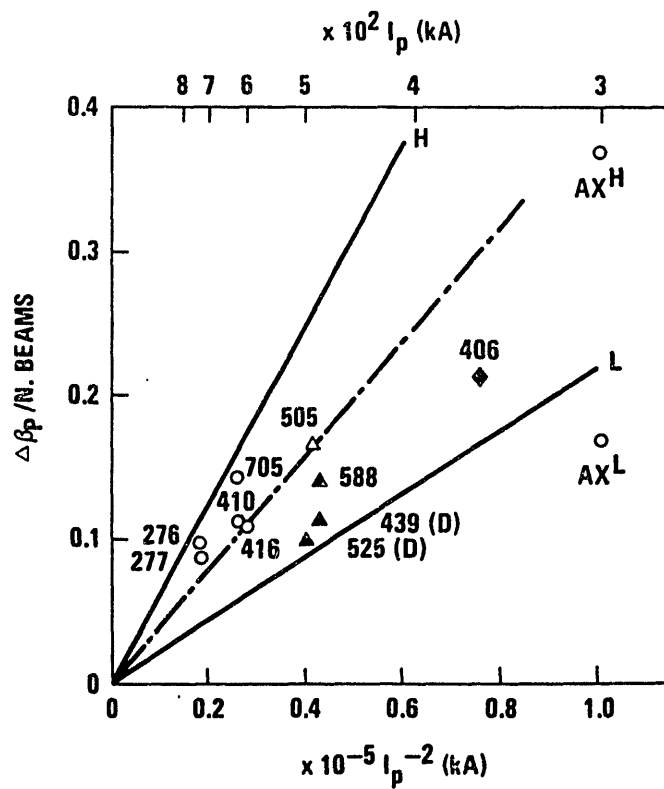


Fig. 4

Fig. 6

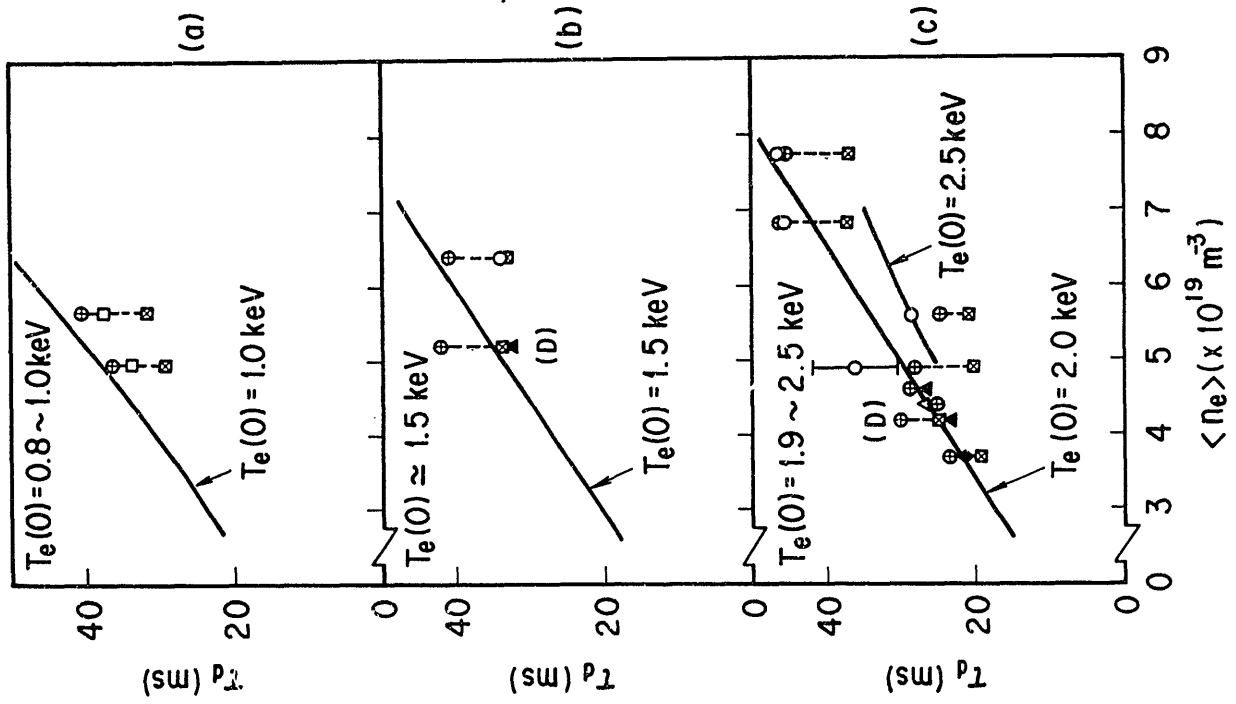


Fig. 5

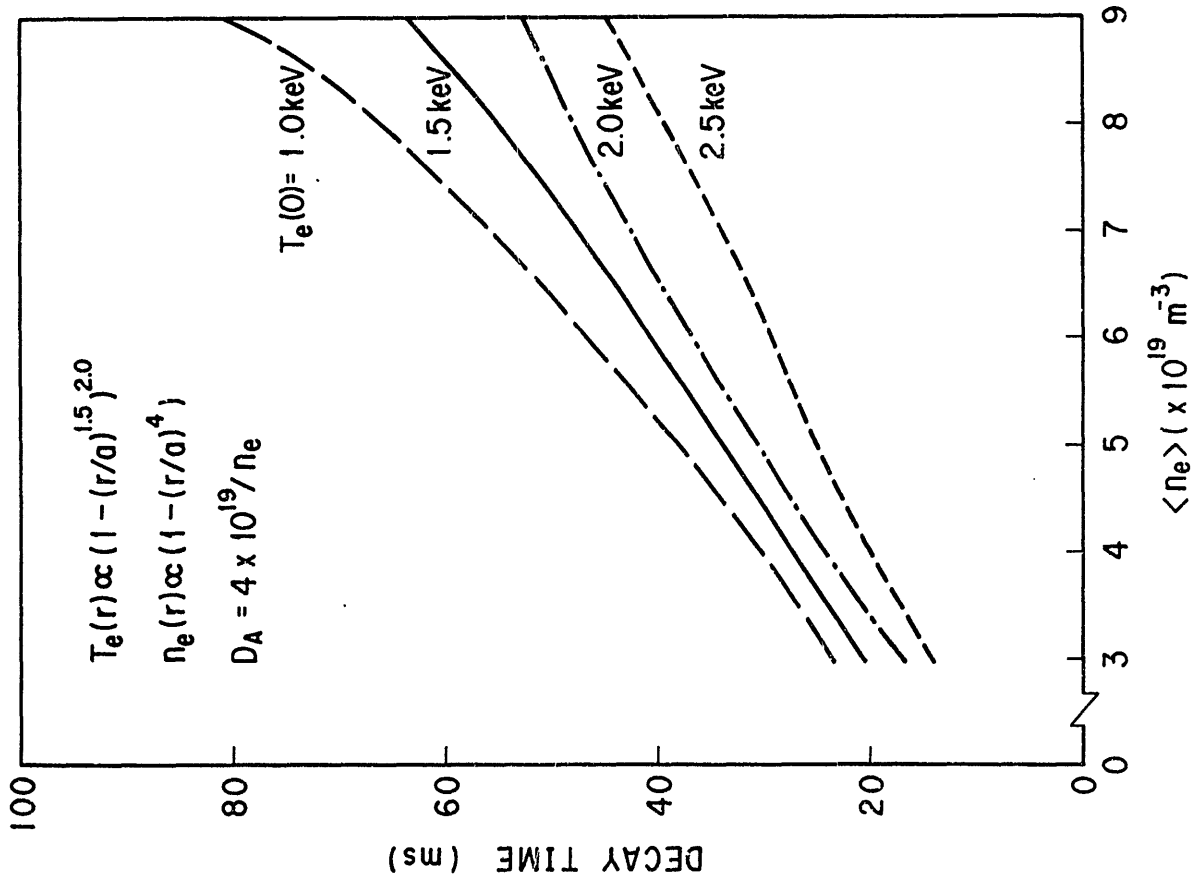


Fig. 7

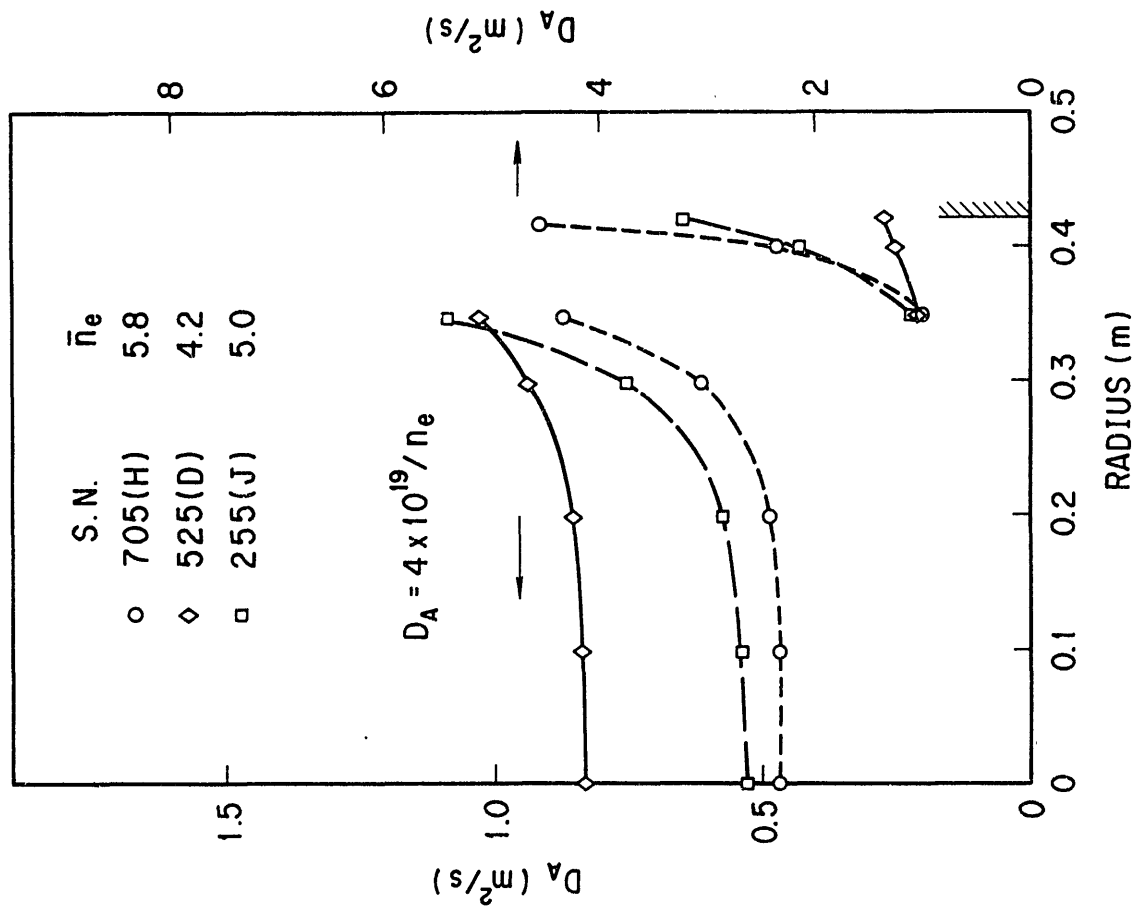
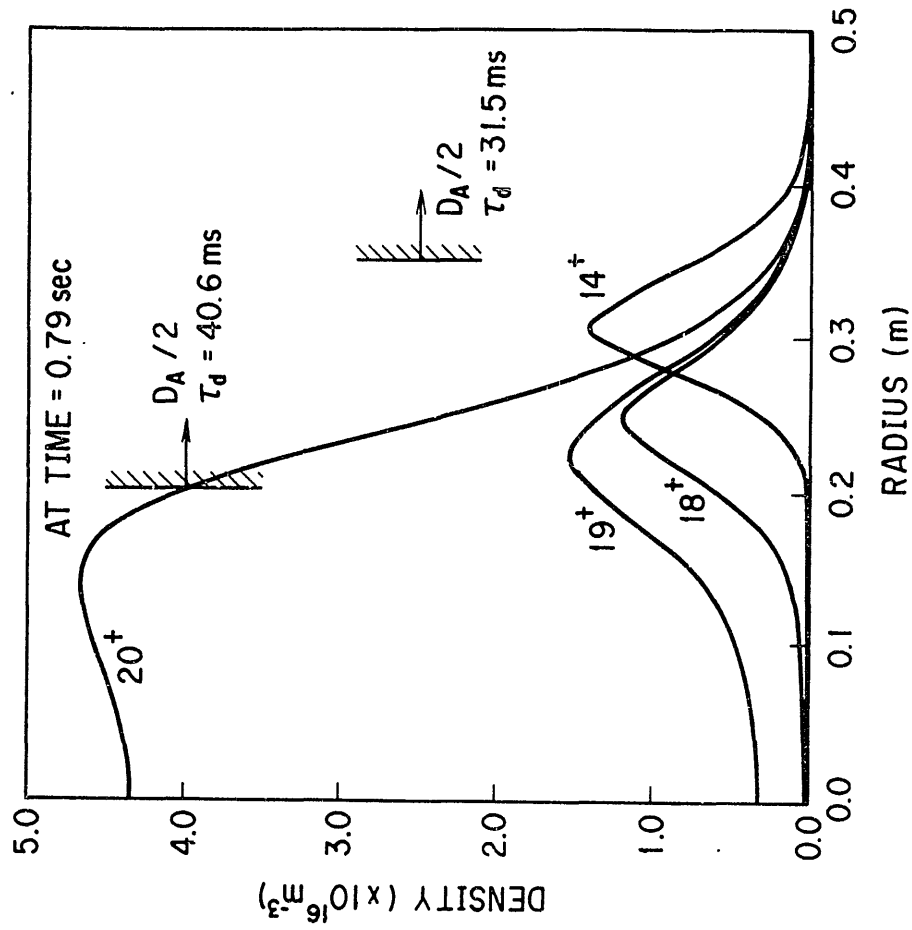


Fig. 8



LIST OF IPPJ-AM REPORTS

- IPPJ-AM-1* “Cross Sections for Charge Transfer of Hydrogen Beams in Gases and Vapors in the Energy Range 10 eV–10 keV”
H. Tawara (1977) [Published in *Atomic Data and Nuclear Data Tables* 22, 491 (1978)]
- IPPJ-AM-2* “Ionization and Excitation of Ions by Electron Impact –Review of Empirical Formulae–”
T. Kato (1977)
- IPPJ-AM-3 “Grotrian Diagrams of Highly Ionized Iron FeVIII-FeXXVI”
K. Mori, M. Otsuka and T. Kato (1977) [Published in *Atomic Data and Nuclear Data Tables* 23, 196 (1979)]
- IPPJ-AM-4 “Atomic Processes in Hot Plasmas and X-Ray Emission”
T. Kato (1978)
- IPPJ-AM-5* “Charge Transfer between a Proton and a Heavy Metal Atom”
S.Hiraide, Y. Kigoshi and M. Matsuzawa (1978)
- IPPJ-AM-6* “Free-Free Transition in a Plasma –Review of Cross Sections and Spectra–”
T. Kato and H. Narumi (1978)
- IPPJ-AM-7* “Bibliography on Electron Collisions with Atomic Positive Ions: 1940 Through 1977”
K. Takayanagi and T. Iwai (1978)
- IPPJ-AM-8 “Semi-Empirical Cross Sections and Rate Coefficients for Excitation and Ionization by Electron Collision and Photoionization of Helium”
T. Fujimoto (1978)
- IPPJ-AM-9 “Charge Changing Cross Sections for Heavy-Particle Collisions in the Energy Range from 0.1 eV to 10 MeV I. Incidence of He, Li, Be, B and Their Ions”
Kazuhiko Okuno (1978)
- IPPJ-AM-10 “Charge Changing Cross Sections for Heavy-Particle Collisions in the Energy Range from 0.1 eV to 10 MeV II. Incidence of C, N, O and Their Ions”
Kazuhiko Okuno (1978)
- IPPJ-AM-11 “Charge Changing Cross Sections for Heavy-Particle Collisions in the Energy Range from 0.1 eV to 10 MeV III. Incidence of F, Ne, Na and Their Ions”
Kazuhiko Okuno (1978)
- IPPJ-AM-12* “Electron Impact Excitation of Positive Ions Calculated in the Coulomb-Born Approximation –A Data List and Comparative Survey–”
S. Nakazaki and T. Hashino (1979)
- IPPJ-AM-13 “Atomic Processes in Fusion Plasmas – Proceedings of the Nagoya Seminar on Atomic Processes in Fusion Plasmas Sept. 5-7, 1979”
Ed. by Y. Itikawa and T. Kato (1979)
- IPPJ-AM-14 “Energy Dependence of Sputtering Yields of Monatomic Solids”
N. Matsunami, Y. Yamamura, Y. Itikawa, N. Itoh, Y. Kazumata, S. Miyagawa, K. Morita and R. Shimizu (1980)

- IPPJ-AM-15 "Cross Sections for Charge Transfer Collisions Involving Hydrogen Atoms"
Y. Kaneko, T. Arikawa, Y. Itikawa, T. Iwai, T. Kato, M. Matsuzawa,
Y. Nakai, K. Okuno, H. Ryufuku, H. Tawara and T. Watanabe (1980)
- IPPJ-AM-16 "Two-Centre Coulomb Phaseshifts and Radial Functions"
H. Nakamura and H. Takagi (1980)
- IPPJ-AM-17 "Empirical Formulas for Ionization Cross Section of Atomic Ions for
Electron Collisions –Critical Review with Compilation of Experimental
Data–"
Y. Itikawa and T. Kato (1981)
- IPPJ-AM-18 "Data on the Backscattering Coefficients of Light Ions from Solids"
T. Tabata, R. Ito, Y. Itikawa, N. Itoh and K. Morita (1981)
- IPPJ-AM-19 "Recommended Values of Transport Cross Sections for Elastic Collision and
Total Collision Cross Section for Electrons in Atomic and Molecular Gases"
M. Hayashi (1981)
- IPPJ-AM-20 "Electron Capture and Loss Cross Sections for Collisions between Heavy
Ions and Hydrogen Molecules"
Y. Kaneko, Y. Itikawa, T. Iwai, T. Kato, Y. Nakai, K. Okuno and H. Tawara
(1981)
- IPPJ-AM-21 "Surface Data for Fusion Devices – Proceedings of the U.S.–Japan Work-
shop on Surface Data Review Dec. 14-18, 1981"
Ed. by N. Itoh and E.W. Thomas (1982)
- IPPJ-AM-22 "Desorption and Related Phenomena Relevant to Fusion Devices"
Ed. by A. Koma (1982)
- IPPJ-AM-23 "Dielectronic Recombination of Hydrogenic Ions"
T. Fujimoto, T. Kato and Y. Nakamura (1982)
- IPPJ-AM-24 "Bibliography on Electron Collisions with Atomic Positive Ions: 1978
Through 1982 (Supplement to IPPJ-AM-7)"
Y. Itikawa (1982)
- IPPJ-AM-25 "Bibliography on Ionization and Charge Transfer Processes in Ion-Ion
Collision"
H. Tawara (1983)
- IPPJ-AM-26 "Angular Dependence of Sputtering Yields of Monatomic Solids"
Y. Yamamura, Y. Itikawa and N. Itoh (1983)
- IPPJ-AM-27 "Recommended Data on Excitation of Carbon and Oxygen Ions by Electron
Collisions"
Y. Itikawa, S. Hara, T. Kato, S. Nakazaki, M.S. Pindzola and D.H. Crandall
(1983)
- IPPJ-AM-28 "Electron Capture and Loss Cross Sections for Collisions Between Heavy
Ions and Hydrogen Molecules (Up-dated version of IPPJ-AM-20)
H. Tawara, T. Kato and Y. Nakai (1983)

- IPPJ-AM-29 "Bibliography on Atomic Processes in Hot Dense Plasmas"
T. Kato, J. Hama, T. Kagawa, S. Karashima, N. Miyanaga, H. Tawara, N. Yamaguchi, K. Yamamoto and K. Yonei (1983)
- IPPJ-AM-30 "Cross Sections for Charge Transfers of Highly Ionized Ions in Hydrogen Atoms (Up-dated version of IPPJ-AM-15)"
H. Tawara, T. Kato and Y. Nakai (1983)
- IPPJ-AM-31 "Atomic Processes in Hot Dense Plasmas"
T. Kagawa, T. Kato, T. Watanabe and S. Karashima (1983)
- IPPJ-AM-32 "Energy Dependence of the Yields of Ion-Induced Sputtering of Monatomic Solids"
N. Matsunami, Y. Yamamura, Y. Itikawa, N. Itoh, Y. Kazumata, S. Miyagawa, K. Morita, R. Shimizu and H. Tawara (1983)
- IPPJ-AM-33 "Proceedings on Symposium on Atomic Collision Data for Diagnostics and Modelling of Fusion Plasmas, Aug. 29 – 30, 1983"
Ed. by H. Tawara (1983)
- IPPJ-AM-34 "Dependence of the Backscattering Coefficients of Light Ions upon Angle of Incidence"
T. Tabata, R. Ito, Y. Itikawa, N. Itoh, K. Morita and H. Tawara (1984)
- IPPJ-AM-35 "Proceedings of Workshop on Synergistic Effects in Surface Phenomena Related to Plasma-Wall Interactions, May 21 – 23, 1984"
Ed. by N. Itoh, K. Kamada and H. Tawara (1984)
- IPPJ-AM-36 "Equilibrium Charge State Distributions of Ions ($Z_1 \geq 4$) after Passage through Foils – Compilation of Data after 1972"
K. Shima, T. Mikumo and H. Tawara (1985)
- IPPJ-AM-37 "Ionization Cross Sections of Atoms and Ions by Electron Impact"
H. Tawara, T. Kato and M. Ohnishi (1985)
- IPPJ-AM-38 "Rate Coefficients for the Electron-Impact Excitations of C-like Ions"
Y. Itikawa (1985)
- IPPJ-AM-39 "Proceedings of the Japan-U.S. Workshop on Impurity and Particle Control, Theory and Modeling, Mar. 12 – 16, 1984"
Ed. by T. Kawamura (1985)

Available upon request to Research Information Center, Institute of Plasma Physics, Nagoya University, Nagoya 464, Japan, except for the reports noted with*.